Karlsruhe Institute of Technology

Investigation of Systematic Effects and Analysis of KATRIN ^{83m}Kr N_{23} Calibration Measurements

Master's thesis of Caroline Fengler

at the Department of Physics
Institute for Astroparticle Physics (IAP)

Reviewer:	Prof. Dr. Guido Drexlin
Second Reviewer:	Prof. Dr. Ulrich Husemann
Advisor:	Dr. Moritz Machatschek
Second Advisor:	Dr. Rudolf Sack

October 01st, 2020 – October 08th, 2021

Ich versichere wahrheitsgemäß, die Masterarbeit selbstständig verfasst, alle benutzten Hilfsmittel vollständig und genau angegeben und alles kenntlich gemacht zu haben, was aus Arbeiten anderer unverändert oder mit Abänderungen entnommen wurde, sowie die Satzung des KIT zur Sicherung guter wissenschaftlicher Praxis in der jeweils gültigen Fassung beachtet zu haben.

I assure truthfully that I have written this master's thesis by myself, that I have given complete and accurate information on all used resources, that I have highlighted everything that has been taken from the work of others, either unchanged or with modifications, and that I have complied with the currently valid version of the KIT statutes for the safeguarding of good scientific practice.

Karlsruhe, Oct. 08^{th}, 2021
Ort, Datum

Caroline Fengler

Contents

Chapter 1

Introduction

Neutrinos are the most abundant particles in the cosmos. They play an important role both in large-scale cosmic events such as super nova explosions and in subatomic processes, like in the β-decay. Since neutrinos only interact by weak interaction they are difficult to detect. Therefore, fundamental questions concerning neutrinos are still unanswered. Observations show that neutrinos can change their flavour eigenstate on their way from their source to a detector, leading to the conclusion that neutrinos must carry a mass. This is a deviation from the Standard Model, in which neutrinos are predicted to be massless. Nevertheless, the neutrino mass is still unknown, since for example the electron neutrino is predicted to be at least 500 000 times lighter than the otherwise lightest lepton, the electron. In order to extend the physical knowledge beyond the Standard Model, the determination of the neutrino mass would constitute a great achievement and will have major implications for many other physical studies.

Since the first experiment in the 1940s attempting to determine the neutrino mass, a variety of measurement approaches have been developed to achieve this goal. The current leading upper constraint on the electron antineutrino mass from direct kinematic measurements comes from the Karlsruhe Tritium Neutrino (KATRIN) experiment with [AAA+19]

$$m_{\overline{\nu_e}} < 1.1\,\mathrm{eV/c^2} \quad (90\,\%\ \mathrm{C.L.})\,. \tag{1.1}$$

The KATRIN experiment is aiming for a sensitivity of $0.2\,\mathrm{eV/c^2}$ (90 % C.L.) [AAB+04]. It consists of a 70 m long setup which is used to perform high-precision spectroscopy of the electrons originating from tritium β-decay. The neutrino mass affects the shape of the electron spectrum close to the kinematic endpoint. The high-precision measurements of the spectrum rely on technically challenging conditions: A stable high-luminosity source is needed, as well as one of the largest ultra-high vacuum vessels ever built and a high-voltage system, which is stable at the order of parts per million.

In addition to the technical challenges of the experiment, the model of the spectrum and systematic effects distorting it must be well understood. In order to determine and quantify systematic effects, measurements with the conversion electrons from added ^{83m}Kr are conducted. The krypton line spectrum allows to draw conclusions about the source potential causing systematic effects on the neutrino mass measurements. Similar to the neutrino mass measurements, also the ^{83m}Kr calibration measurement must be well understood.

The thesis at hand aims for a comprehensive study of the systematic effects affecting the ^{83m}Kr calibration measurements. Furthermore, it is intended to develop a standardised procedure for measurements with krypton and their data analysis in order to reliably quantify the systematic impact of the source potential on the neutrino mass. For this purpose, the systematic influences of different parameter and model settings are quantified. In addition, various measurement settings are compared to study their influence on the estimates of the ^{83m}Kr measurements. The identified procedure and modelling is applied to the summer 2021 krypton measurements of KATRIN to determine the observables of the source potential. The thesis is structured as follows:

In chapter 2, a brief introduction into neutrino physics is given. Following a short historical introduction of the first neutrino observations, the neutrino oscillations are discussed. Furthermore, various experimental approaches that allow to determine the neutrino mass are compared.

Chapter 3 gives a detailed overview over the setup and functioning of the KATRIN experiment. For this, the functional units of the experiment are introduced one by one. In addition, an insight into the data analysis is given and the treatment of different uncertainties is discussed. Finally, the KATRIN sensitivity on the neutrino mass is derived.

Chapter 4 introduces the krypton mode of the KATRIN experiment. First the model of the krypton line spectrum is outlined, followed by a discussion about the physical processes in the source. In the course of this, different applications for the krypton mode are explained.

In chapter 5, a standardised measurement and analysis strategy is developed. For this purpose, a comprehensive study of systematic effects influencing the krypton spectrum is performed. First, the systematic effects caused by different parameter and model settings are quantified, allowing to develop standardised analysis settings. These include the ^{83m}Kr N line parameters, parameters of the magnetic field strength, model settings of different transmission functions and many more. In a second step, different measurement and analysis approaches are compared to quantify their effect on the observables of the source potential. This is done based on specific measurements. The resulting measurement and analysis strategy is finally applied to determine the systematic effect of the source potential on the neutrino mass.

A summary of the obtained results and an outlook for following investigations are given in chapter 6.

Chapter 2

Neutrino Physics – An Overview

In 1914, intense studies on radioactive decay processes by Chadwick lead to the observation of a continuous spectrum for the electrons of a β-decay [Cha14]. At that time the β-decay was assumed to be a two-body problem, since only the electron or positron and the daughter nucleus could be measured. Under energy momentum conservation, a monochromatic fermion energy was expected for this decay. This problem could be resolved 1930 by a theory of Pauli, expanding the β-decay to a three body process obeying energy momentum and angular momentum conservation. Based on this assumption Pauli also predicted characteristics of the third theoretical particle. He followed, that it must be a neutral particle with spin $\frac{1}{2}$ and it must only interact weakly, since it was not measured to this point [vM85].
In 1956, a neutrino-induced reaction, the inverse β-decay could be detected by Cowan and Reines at the Savannah River Experiment [CRH+56]. Using the antineutrinos from the Savannah river reactor and the protons of 200 L of cadmium chloride infused water the inverse β-decay lead to

$$\overline{\nu_{\mathrm{e}}} + \mathrm{p} \rightarrow \mathrm{e}^{+} + \mathrm{n}\,. \tag{2.1}$$

The positron and neutron resulting from this reaction could be detected by a delayed coincidence signature. First, the positron would annihilate with an electron producing two signature photons. As a second process the neutron is captured by the cadmium chloride, which then de-excited by emitting a 10 µs delayed photon. Detecting both signals showed the process of the inverse β-decay as predicted.
Additionally to the electron neutrino ν_{e}, two additional neutrino flavours were discovered: the muon neutrino ν_{μ} [DGG+62] and the tau neutrino ν_{τ} [KUA+01].
Experiments like ALEPH could prove, that there are only three neutrino flavours [DDL+90]. This lead to including the neutrino in the Standard Model.

2.1 Neutrino Oscillations

The Standard Model of particle physics provides a comprehensive theory of the elementary particles and their fundamental interactions within the framework of quantum field theory. Within this theory, the neutrino is predicted to be massless. In the 1990's, observations of neutrino oscillations led to the conclusion, that this prediction must be inaccurate, which led to the need of a theory beyond the Standard Model (BSM).

2.1.1 Experimental Evidence

The Homestake experiment aimed at measuring the total electron neutrino flux coming from the sun [CDR+98]. The electron neutrinos are produced by the high number of massive fusion processes happening in the sun. The experiment was designed using the chemical detection process

$$\nu_e +^{37} \mathrm{Cl} \rightarrow^{37} \mathrm{Ar} + \mathrm{e}^- \,. \tag{2.2}$$

Despite using a detection mass of 615 t of perchloroethylene (C_2Cl_4) only 1/3 of the expected rate could be detected, leading to the solar neutrino problem. Following this, other experiments, such as Kamiokande, SAGE, GALLEX and Super Kamiokande [Suz95, AFG+94, HHH+99, FFI+01], obtained according values for the solar electron neutrino rate. Since no adjustments of the solar model could explain the obtained results, it was followed that the effect was related to the neutrino propagation.
Pontecorvo first introduced the idea of neutrinos changing their flavour during propagation [GP69]. However, the concept of neutrino oscillations was only possible for massive neutrinos.
Finally, the Sudbury Neutrino Observatory (SNO) was the first experiment able to detect neutrino oscillations. This was possible, since not only the electron neutrino flux, but also the sum of all neutrino fluxes were measured [AAA+02].

2.1.2 Theoretical Description

The theoretical concept of the neutrino oscillations is based on describing the flavour states of the neutrino, which are also the eigenstates to the weak interaction, as a superposition of the corresponding mass states, being the eigenstates of the free Hamiltonian. Here, the flavour states are denoted by $|\nu_\alpha\rangle$ with $\alpha \in$ e, μ, τ and the mass states are symbolised by $|\nu_k\rangle$ with $k \in 1, 2, 3$. Using the unitary PMNS mixing matrix U, one can express the relation between the states with [Sch14]

$$|\nu_\alpha(t)\rangle = \sum_k \exp\{-\mathrm{i}E_k^{\mathrm{tot}}t\} \, |\nu_k\rangle \,. \tag{2.3}$$

The factor $\exp\{-\mathrm{i}E_k^{\mathrm{tot}}t\}$ describes the time propagation of a free particle. The probability P of detecting a neutrino with initial flavour state α in a flavour state β can be derived under the assumption of CP invariance as [Bil10]

$$\mathrm{P}(\nu_\alpha \to \nu_\beta) = |\,\langle\nu_\beta|\nu_\alpha(t)\rangle\,|^2 = \delta_{\alpha\beta} - 4\sum_{k>j} \mathrm{Re}(U^*_{\alpha k}U_{\beta k}U_{\alpha j}U^*_{\beta j})\sin^2\left(\frac{\Delta m^2_{kj}L}{4E}\right) \,. \tag{2.4}$$

Here, the oscillation length L is the distance between the source and the detector. E is the energy of the neutrino. Δm^2_{kj} denotes the difference between the squared masses k and j, so that $\Delta m^2_{kj} = m^2_k - m^2_j$. Consequently, only mass differences can be obtained by oscillation experiments, not the absolute neutrino masses. Furthermore, the exact ordering of the neutrino masses can not be determined from the measurements. But based on the obtained results, there are two possible orderings for the mass eigenstates: the normal ordering (NO) with $m_1 < m_2 < m_3$ and the inverted ordering (IO) with $m_3 < m_1 < m_2$ [Sch14]. A global analysis of neutrino oscillation experiments has been conducted, giving the differences of the squared mass states as follows [ZBB+20]

$$\Delta m^2_{21} = \left(7.55^{+0.20}_{-0.16}\right)\,10^{-5}\,\mathrm{eV}^2/\mathrm{c}^4 \qquad (\mathrm{NO},\mathrm{IO}), \tag{2.5}$$
$$\Delta m^2_{32} = (2.424 \pm 0.03)\,10^{-3}\,\mathrm{eV}^2/\mathrm{c}^4 \qquad (\mathrm{NO}), \tag{2.6}$$
$$\Delta m^2_{32} = \left(-2.50^{+0.04}_{-0.03}\right)\,10^{-3}\,\mathrm{eV}^2/\mathrm{c}^4 \qquad (\mathrm{IO}). \tag{2.7}$$

2.2 Complementary Methods for the Determination of the Neutrino Mass

The observations of neutrino oscillations raised the need for new experimental approaches which are able to determine the neutrino mass. In the following, different strategies to constrain the neutrino mass are introduced.

2.2.1 Mass Limits from Cosmology

Neutrinos can play an important role in the formation of large scale cosmic density structures, since they are one of the most abundant known particles in the cosmos. Due to their weak interaction they are able to escape overdense regions causing washed out density contrasts. Conclusions about their mass can be made since this process is only possible for length scales smaller than the free-streaming length, which is inverse proportional to the neutrino mass [Per09]. Therefore, the cosmological observable corresponds to the direct sum of the mass eigenstates

$$m_{\mathrm{cosm}} = \sum_i m_i \,. \tag{2.8}$$

Nevertheless, the cosmological observable depends on the cosmological model used in the analysis. Furthermore, a combination of multiple cosmological studies is needed to determine a constraint on the neutrino mass. In the most stringent case an upper limit of $m_{\mathrm{cosm}} < 0.11\,\mathrm{eV}/\mathrm{c}^2$ is assumed [ZBB+20].

2.2.2 Mass Limits from Neutrinoless Double Beta Decay

Information about the neutrino mass could also be provided by measuring the hypothetical neutrinoless double beta decay $0\nu\beta\beta$. Some nuclei are able to undergo two β-decays at once. If the antineutrino resulting from one β-decay could as a virtual particle directly contribute as a neutrino for the second β-decay, only two electrons would be found in the final state of this $0\nu\beta\beta$-decay. This process can only be possible if neutrinos are Majorana particles which can be their own antiparticles. Even though

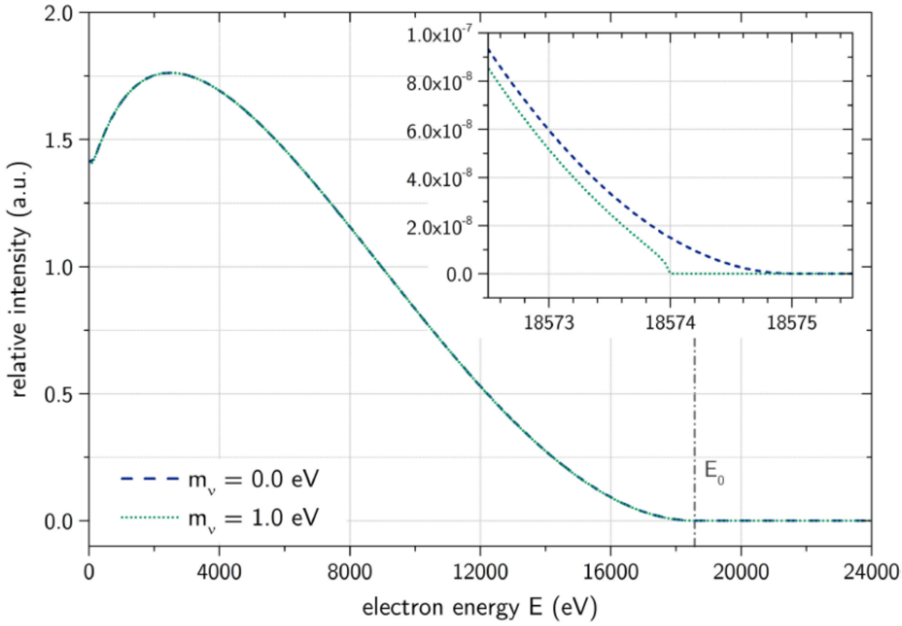

Figure 2.1: Differential β-spectrum of tritium, showing the cases $m_{\overline{\nu_e}} = 0\,\mathrm{eV}$ and $m_{\overline{\nu_e}} = 1\,\mathrm{eV}$. The impact of the neutrino mass is visible at the endpoint $E_0 \lesssim 18\,575\,\mathrm{eV}$, shown in a detailed view in the upper right corner. Figure from [Kle14].

this process has not been observed yet, it is possible to constrain the effective Majorana mass $m_{\beta\beta}$, being the coherent sum of the mass eigenstates of the electron neutrino weighted by PMNS matrix elements, under some model dependent assumptions. This is possible since the half-life $T^{0\nu}_{1/2}$ can be obtained from the measured count rate and is related to $m_{\beta\beta}$ via [Zub20]

$$T^{0\nu}_{1/2} \sim \frac{1}{m^2_{\beta\beta}} \,. \tag{2.9}$$

For the effective Majorana mass, it is predicted that $\langle m_{\beta\beta}\rangle = |\sum_i U^2_{ei} m_i| < 61 - 165\,\mathrm{meV/c^2}$ [GGH+16, ABB+18, AAA+20, ABB+19].

2.2.3 Mass Limits from Single Beta Decay

Based on the single β-decay, the neutrino mass can be obtained independent of an complex underlying model, since it provides a laboratory approach based on a kinematic measurement. Therefore, several experiments make use of this decay process. The ECHo experiment aims to measure the mass of the electron neutrino by analysing the ^{163}Ho spectrum after an electron capture process of holmium. The spectrum is measured with low temperature magnetic calorimeter arrays. With this method, a measurement in the sub-meV range is aspired [GBD+14].

Both the KATRIN experiment and Project 8 use the β^--decay of tritium to obtain the electron neutrino mass, following the reaction equation

$$^3\mathrm{H} \rightarrow ^3\mathrm{He}^+ + \mathrm{e}^- + \overline{\nu_\mathrm{e}}\,. \tag{2.10}$$

To determine the neutrino mass the endpoint region of the β-spectrum is relevant, since at the endpoint all the kinetic energy is carried by the measured electron. Therefore, the shape of the β-spectrum in the endpoint region contains the information about the squared neutrino mass, which can be obtained by fitting the spectrum. The tritium β-spectrum with its endpoint region is shown in figure 2.1. Project 8 uses for the measurement of the electron energies cyclotron radiation emission spectroscopy. For this method the tritium atoms are confined in a strong magnetic field. The decay electron can then be detected by its cyclotron frequency using a precision measurement of the emitted radio waves. Project 8 aims with this method at a sensitivity on the neutrino mass of 40 meV [MF09].
In contrast the KATRIN experiment measures the tritium spectrum around the endpoint by using an integrating high energy pass filter to obtain the maximum electron energy. A detailed description of the experimental setup and the way of functioning of the energy filter is given in the next chapter 3. The current leading upper constraint on the neutrino mass from direct kinetic measurements comes from the KATRIN experiment with [AAA+19]

$$m_{\overline{\nu_\mathrm{e}}} < 1.1\,\mathrm{eV/c^2} \quad (90\,\%\ \mathrm{C.L.})\,. \tag{2.11}$$

Chapter 3

KATRIN Experiment

The KATRIN experiment is located at the Karlsruher Institute of Technology (KIT) at Campus North. Its goal is to measure the mass of the electron antineutrino by precision spectroscopy of the tritium β-decay spectrum, as described in subsection 2.2.3, aiming at a sensitivity of 200 meV. Section 3.1 provides an overview over the components and measurement principles which are relevant for an understanding of the KATRIN experiment. All specifications are based on the recently updated KATRIN report [AAA+21]. In section 3.2 a brief introduction into the KATRIN data analysis is given.

3.1 Experimental Setup

From the source to the detector the 70 m long beam line is divided into functional units, each serving a specific purpose. The most prominent components are described in the following, in the order of their position along the beam line starting at the rear and source section. An overview of the arrangement of the functional units along the beam line is provided in figure 3.1.

3.1.1 Windowless Gaseous Tritium Source and Rear Section

The particles of interest for the KATRIN experiment, the β-electrons, originate from tritium β-decay, which occurs in the **Windowless Gaseous Tritium Source (WGTS)**. The WGTS consists of a 10 m long beam tube with a diameter of 90 mm surrounded by superconducting solenoid magnets and a two-phase neon cryostat. The gas gets injected into the beam tube in the middle of the WGTS and gets pumped out at the ends of the WGTS through two pumping ports. This setup ensures an injection rate of tritium of 5×10^{19} molecules/s with a gas purity of $\geq 95\,\%$. A Laser Raman (LARA) setup continuously monitors the tritium purity as well as the concentrations of the six different hydrogen isotopologues. The initial partial pressure at the injection site amounts to $\lesssim 3 \times 10^{-3}$ mbar and is kept constant within 0.1 %. The pumps at both ends of the WGTS reduce the this partial pressure towards the ends of the WGTS. As shown in figure 3.2, this leads to a decrease of the density by a factor of ~ 100. The resulting longitudinal density profile is gas-type dependent and shows a non-linear progression.

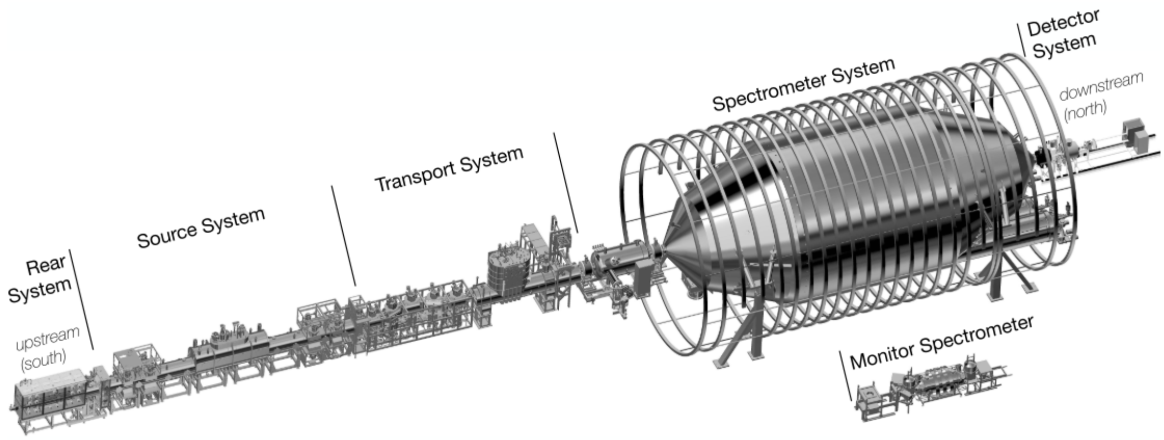

Figure 3.1: Setup of the KATRIN experiment with its different sections. The β-electrons originate from the decaying tritium inside the WGTS, located in the source section. The rear section enables the monitoring and adjusting of the source plasma. Additionally, it contains an e-gun for calibration measurements. The transport system serves the reduction and blocking of gas components towards the spectrometer section. Therefore, it is equipped with multiple differential and cryogenic pumping stations, solenoid magnets and an electrode system. The spectrometer system covers the pre- and main spectrometer, which serve as integrating high-pass energy filters for the β-electrons. The monitor spectrometer works the same way, but is used parallel to the beam line to monitor the high-voltage stability. The detector system is responsible for detecting the filtered electrons and passing the measured count rates to the data-acquisition system. Figure from [AAA+21].

This decrease of the density is an important feature of the source since it is designed as a windowless source, indicating there is no solid barrier implemented in the beam tube preventing the tritium gas components from travelling into the spectrometer section. Therefore, the turbo molecular pumps implemented in the source and transport section (see section 3.1.2) withhold the neutral gas while dipoles and ring electrodes block the ions. This is done without causing an energy loss of the electrons as it would result from a window material. Hence, unnecessary sources of systematic errors are prevented.

The maximum column density ρd, it being the integrated number of tritium molecules along the beam tube axis per unit of cross-sectional area, is set to 5×10^{21} molecules/m^2 with a required stability of $< 0.1\,\%$/h. This introduces strict stability limits for the source temperature, the injection rate, and pumping speed. The value for the maximum column density was designed for operating the WGTS at 30 K, since a low temperature setting is important for the KATRIN neutrino mass measurements. It reduces broadening effects in the measured spectrum such as Doppler broadening or broadenings through plasma effects in the source. Nevertheless, the 30 K temperature setting does not allow a proper comparability of the data sets of the neutrino mass measurements with the plasma systematics measurements performed with tritium plus krypton at 80 K [Ost20]. Krypton is needed for reference measurements and handling

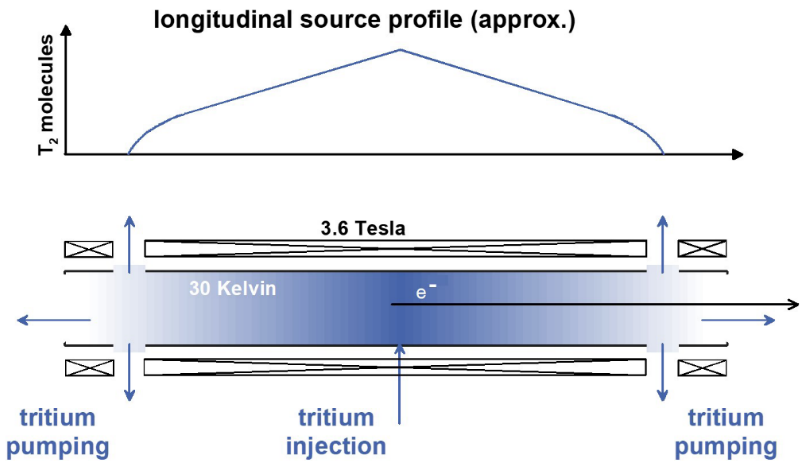

Figure 3.2: Setup and gas profile of the WGTS. In the lower half the longitudinal section of the WGTS is shown. The blue arrows depict the tritium gas flow. Tritium is injected in the middle of the WGTS. Two differential pumping systems at the front and rear end pump out the tritium, causing a decrease in density towards the ends. This is indicated by the fading blue color. The corresponding longitudinal source profile for the tritium molecules is shown in the upper half. The black arrow in the WGTS shows the direction of the electrons which are guided towards the spectrometer. Nevertheless, electrons also travel towards the rear section right after being generated in the source or after deflection in the spectrometer section. Figure from [AAA+21].

the systematics of the plasma. Inside the WGTS 80 K is the lowest possible temperature setting without risking a freeze-out of krypton. Therefore, the WGTS is operated at 80 K for all recent and future measurements. This change limits the column density to 75 % ρd.
To provide a homogeneous plasma potential and therefore to be able to control the boundary conditions in the source the rear end of the WGTS is terminated with a gold-plated **rear wall (RW)**. The rear wall can be set to an electric potential relative to the rest of the beam tube. The rear section is also equipped with a **monoenergetic, angular selective electron gun (e-gun)** emitting electrons through a hole in the middle of the rear wall. It is used for specific reference measurements [Sac20, Bab14]. More about the application of the e-gun can be found in subsection 3.1.3.
For monitoring the source activity of around 1.7×10^{11} Bq two **β-induced X-ray spectrometry (BIXS) detectors** are positioned outside the beam tube next to the rear wall [Pri13]. The system indirectly measures the upstream(1) moving electrons by detecting their emitted X-ray radiation from the absorption process in the gold coating of the rear wall. This upstream moving electron flux is composed not only of source electrons starting in the upstream direction, but also of downstream moving

(1) "Upstream" is defined in reference to the main particle stream in the KATRIN experiment moving from the WGTS to the FPD. Therefore, "upstream" denotes a movement in direction of the rear wall, whereas "downstream" equals the movement of the main particle stream towards the FPD.

electrons being reflected back onto the RW by the magnetic mirror effect or the electric retarding potential in one of the spectrometers. Additionally, the relative intensity of the downstream moving electron flux can be measured by inserting the **Forward Beam Monitor (FBM)** into the flux tube of the transport section. The homogeneous source magnetic field of 2.52 T (equal to 70 % of the design magnetic field) is generated by the superconducting solenoids of the WGTS and transports the created electrons adiabatically from the source downstream through the transport and spectrometer section towards the detector [BF28].

3.1.2 Transport Section

From the source section the β-electrons are guided adiabatically by twelve superconducting magnets through the transport section. Here, they are passing two pumping systems configured as chicanes. First, the two stages of the **differential pumping system (DPS)** reduce the neutral tritium flow rate in downstream direction by at least seven orders of magnitude. As the DPS transport section is configured as a chicane tilted with 20° angles to each other in horizontal plane it also prevents neutral gas from passing into the spectrometer section. It would require several scattering processes for the particles to pass the chicane, hence, the probability of passing the section decreases and a beaming effect(2) is prevented. Additionally magnetically guided tritium ions are blocked with a ring and dipole electrode system. More precisely, the dipole electrodes remove positive ions using $E \times B$-drift while blocking negative ions and secondary electrons. The ring electrodes additionally block and reject positive ions [Kle18]. Following the DPS the **cryogenic pumping system (CPS)** again reduces the flow rate of neutral gas by more than seven orders of magnitude [Röt19]. For this purpose a cryo-sorption pump with a condensed argon layer on the surface of the gold-plated inner beam tube wall is used. The argon layer functions as an adsorber for tritium, which can easily be removed and renewed. This is an advantage compared to a solid adsorber material. In total a tritium flow rate reduction factor of more than 10^{14} is achieved.

3.1.3 MAC-E Filter

For the KATRIN experiment three **Magnetic Adiabatic Collimation with Electrostatic filter (MAC-E) spectrometers** are used: A Pre-Spectrometer (PS) and Main Spectrometer (MS) in the beam line and a Monitor Spectrometer (MoS) in a parallel setup to the beam line.
The **measurement principle** is visualized in figure 3.3, its description is based on the MS. In principle, the MAC-E filter consists of two components: a magnetic adiabatic collimator for the isotropically emitted electrons and an electrostatic energy filter. The magnetic field guiding the electrons through the spectrometer is generated by

(2) The beaming effect concerns the passing density distribution of molecules within a straight cylindrical pipe. The molecular flow inside the pipe changes from an input uniformly distributed density towards a centrally increased density distribution [SJZ08].

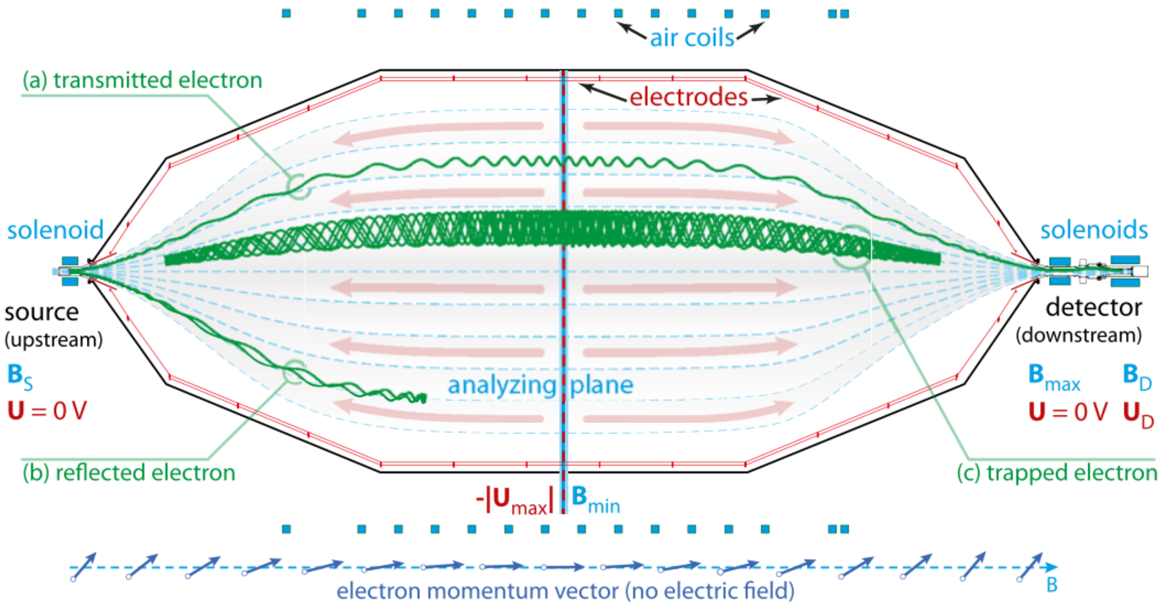

Figure 3.3: Measurement principle of the MAC-E filter. The MAC-E filter consists of a magnetic adiabatic collimator paired with an electrostatic energy filter. Superconducting solenoid magnets at both ends of the spectrometer provide the magnetic guiding field for the electrons. The retarding potential for the energy filter is created by the wire electrodes together with the vacuum vessel on high-voltage. Through the magnetic adiabatic collimation, the momentum vector of the electrons gets transformed resulting in only a longitudinal component. This is depicted by arrows underneath the spectrometer vessel. The retarding potential slows down the electrons towards the analysing plane. Only electrons with sufficient energy pass the filter and are transmitted to the detector (a). In case of insufficient kinetic energy, the electrons are reflected (b). Electrons which originate from inside the spectrometer volume are being trapped due to the magnetic bottle effect at both ends of the spectrometer (c). Figure from [AAA$^+$21].

superconducting solenoid magnets located at the entrance and exit of the spectrometer vessel. Towards the middle of the spectrometer, the so-called analysing plane (AP), the magnetic field drops by several orders of magnitude. The minimal magnetic field B_{min} can be fine-tuned by the air coil system surrounding the spectrometer vessel. One component of the air coil system is the low-field correction system (LFCS) which is used to optimize the homogeneity of the magnetic fields in the MS. Additionally a second component, the earth magnetic field compensation system (EMCS), compensates for the earth magnetic field in the spectrometer.
The force of the magnetic gradient transforms the cyclotron energy of the electrons into the longitudinal component without loss of energy. The conserved variable is the orbital magnetic momentum $\vec{\mu}$ with:

$$\mu = |\vec{\mu}| = \frac{E_\perp}{B} = \mathrm{const}\,. \tag{3.1}$$

$E_\perp$ and B symbolize the transversal component of the kinetic electron energy and the magnetic field, respectively. This adiabatic transformation allows the electrons to be collimated and filtered according to their kinetic energy. This is achieved with a retarding potential functioning as an integrating high-pass filter, which is slowing down the electrons. The retarding potential is created by wire electrodes covering the inner surface of the MS together with the spectrometer vessel on high voltage. Electrons with insufficient kinetic energy are thereby reflected and return, in case of the PS or MS, through the WGTS where they get absorbed by the rear wall. Thus, the reflected electrons contribute to the source plasma depending on the rear wall set point. The sufficiently energetic electrons pass the filter and are guided onto the detector.
With this setup an energy resolution in the range of eV is achieved while working at electrons energies of several keV. Also it ensures a high luminosity for the signal electrons.

Energy resolution

The energy resolution ΔE is determined by the ratio between the minimum and maximum magnetic field strength, B_{min} and B_{max}, in the spectrometer and depends linearly on the energy of the electrons E:

$$\frac{\Delta E}{E} = \frac{B_{\mathrm{min}}}{B_{\mathrm{max}}} , \tag{3.2}$$

whereby $B_{\mathrm{min}} \ll B_{\mathrm{max}}$. B_{max} is always at 4.2 T, whereas B_{min} can be set to different magnetic field settings. Frequently used settings are 1 G, 2.7 G and 6.3 G. The lower settings are mostly used for investigations with added krypton in the source, while the 6.3 G setting is applied for the neutrino mass measurements with pure tritium. Accordingly, for the krypton lines at $\sim 32\,136$ eV in 2.7 G setting, the energy resolution results to $\Delta E \approx 2.1$ eV. When choosing the 1 G setting an energy resolution of down to 0.8 eV is reached. However, the experimental setup does not allow to reduce the energy resolution by minimizing B_{min} at will. The limiting factor for this is the vessel diameter, due to the magnetic flux being constant:

$$\Phi = \int_A \vec{B} \cdot \mathrm{d}\vec{A} = \mathrm{const}\,. \tag{3.3}$$

$\vec{A}$ denotes the infinitesimal area element through which the magnetic field is passing. The equation shows that a smaller magnetic field setting for B_{min} results in a larger fanning of the magnetic field lines. Therefore, when using a small magnetic field setting such as the 1 G setting, the outer magnetic field lines collide with the vessel wall and the guided electrons do not reach the detector. The energy resolution of the MAC-E filter must not be confused with the energy resolution of a particle detector, being the width of the energy distribution of the measured events. In case of the MAC-E filter, the effective energy resolution of the spectrum significantly increases with the knowledge of the width and shape of the transmission function, not only by decreasing the magnetic field setting.

Maximum acceptance angle

For the transmission properties of the KATRIN experiment the source magnetic field B_{src} and the so-called acceptance angle under which the electrons are generated relative to the magnetic field are essential features. The ratio between B_{src} and the maximal magnetic field in the beam tube B_{max} determines the maximum acceptance angle θ_{max} under which electrons still get transmitted. This is because when travelling from the source into regions with higher magnetic field the angle between particle momentum and magnetic field direction increases. If a limit of 90° is reached, the electron gets reflected by which is known as the magnetic bottle effect. Electrons generated under a lower acceptance angle can pass the higher magnetic field and therefore get transmitted. From the magnetic bottle effect the maximum acceptance angle can be derived as

$$\theta_{\text{max}} = \arcsin\left(\sqrt{\frac{B_{\text{src}}}{B_{\text{max}}}}\right). \tag{3.4}$$

It follows that the maximum acceptance angle can be tuned via the magnetic field setting. Since a larger maximum acceptance angle correlates with a longer path length of the electrons in the spectrometer this can be used to optimize the energy loss of the electrons. This then leads to a larger energy loss of the electrons due to scattering processes and synchrotron radiation. Thus, an optimal maximum acceptance angle reduces the systematic uncertainties of the experiment. For $B_{\text{src}} = 2.52\,\text{T}$ and the maximum magnetic field strength applied at the pinch magnet in the detector section $B_{\text{max}} = B_{\text{pch}} = 4.2\,\text{T}$, electrons with an starting acceptance angle of up to 51° get transmitted through the beam line.

Transmission function

The probability for isotropically generated electrons to be transmitted by the MAC-E filter is described by the transmission function:

$$T(E, E_+) = \begin{cases} 0 & \text{if} \quad E_+ < 0 \\ 1 - \sqrt{1 - \frac{E_+ B_{\text{src}}}{E B_{\text{ana}}}} & \text{if} \quad 0 \leq E_+ \leq \Delta E \\ 1 - \sqrt{1 - \frac{B_{\text{src}}}{B_{\text{max}}}} & \text{if} \quad E_+ > \Delta E \end{cases} \tag{3.5}$$

The surplus energy of the electrons $E - qU_0$ is represented by E_+. E and U_0 symbolize the electron energy and the retarding potential, respectively. The transmission function depends on the initial angular distribution in the source. Therefore, other electron sources like the e-gun show different transmission functions [Sch21].
The physical decay process in the source can be described by the differential spectrum $\frac{\mathrm{d}N}{\mathrm{d}E}(E, E_0, m_\nu^2)$ shown in figure 2.1. The transmission function as well as the differential spectrum are connected by convolution to the rate $R(qU_0)$, which is measured by the detector, as follows:

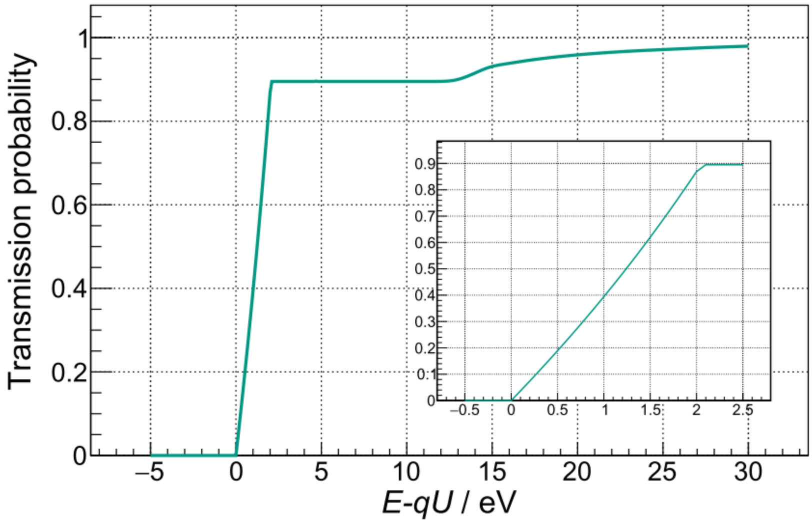

Figure 3.4: KATRIN transmission and response function at nominal conditions for the neutrino mass measurements. It displays the transmission probability dependent on the surplus energy $E-qU$. The response function represents the transmission function for surplus energies $< 2\,\text{eV}$, as shown in detail in the bottom right plot. Plot made with KaFit. Figure from [Ost20].

$$R(qU_0) \propto \int_{qU_0}^{E_0} \frac{\mathrm{d}N}{\mathrm{d}E}(E, E_0, m_\nu^2) \cdot T(E, qU_0)\,\mathrm{d}E\,. \tag{3.6}$$

The differential spectrum depends on the neutrino mass, which is the wanted observable, and on the transmission function. By deconvoluting the transmission function from the rate it is possible to obtain the wanted information from the integral.

As an extension of the transmission function a **response function** can be introduced, covering additional influences on the electron energy after its generation. The most relevant effects are the energy loss of the electrons from inelastic scattering on tritium in the WGTS and an energy broadening by the synchrotron radiation and by the Doppler effect. A plot of the response and transmission function is shown in figure 3.4. The effects are further described in subsection 4.3.2.

As a tool for precision transmission studies the **E-gun**, a high resolution angular-selective electron gun, has been implemented in the RS of the KATRIN experiment. The E-gun is coupled to the MS high voltage. Via illumination of the metallic photocathode by a UV light source, a pulsed electron beam is produced. Those electrons are guided magnetically from the gun through a hole in the rear wall and along the beam line. Other purposes for using the E-gun are for studying the electromagnetic characteristics along the beam line, for investigations and monitoring of the source characteristics, such as column density (CD) stability and energy loss function measurements.

The most prominent MAC-E filter in the KATRIN experiment is the **main spectrometer (MS)**. With its 10 m diameter and a length of 23 m it is also the biggest spectrometer build into the experiment [Val09]. These dimensions allow for a precise filtering of the β-electrons before reaching the detector. The length of the spectrometer is needed to assure that the electrons are collimated adiabatically by a slowly decreasing magnetic field strength. The spectrometer can be operated at down to −35 kV for investigating ^{83m}Kr conversion electrons. The typical operation voltage for tritium measurements lies around −18.6 kV in reference to the grounded WGTS. To limit the energy-scale-related contribution to the KATRIN systematic uncertainty budget and to prevent a significant bias of the neutrino mass, a relative precision of the retarding potential at the order of ppm must be ensured. For this purpose a high-precision high voltage supply and monitoring system is used for the experiment, such as the MoS and an additional high voltage (HV) divider directly measuring the high voltage at the vessel. Furthermore, the HV setup of the spectrometer vessel contributes to background reduction. The inner surface of the vessel is covered with an inner wire electrode (IE) system, which is set a few hundred of volts more negative than the vessel potential [Val09,Pra11,Zac15]. This way, electrons which originate from the walls, e.g. created by cosmic-ray interactions, are reflected back onto the vessel surface [Lei14].

Besides the MS another MAC-E filter, the **pre-spectrometer (PS)**, is build into the beam line as a pre-filter for the low-energy range of the β-spectrum. For a voltage setting of −18.3 kV the PS rejects all electrons except those in the region of interest (ROI) close to the tritium endpoint. Furthermore, it ensures an adiabatic transport of the electrons at all retarding potential settings with its minimum magnetic field of 200 G. This holds even if the PS is grounded.

A third MAC-E filter, the **MoS**, is used in a parallel setup to the beam line for long term energy scale reference measurements. This monitoring is needed for a precise knowledge of the MS retarding potential. For this purpose the MoS is galvanically connected to the HV system of the MS, which means that they have equal vessel voltages and get powered by the same power supply. This setup allows for synchronized data acquisition and real time monitoring. As an electron source an ultra-stable krypton source has been implemented in order to observe its monoenergetic conversion electron lines.

3.1.4 Focal Plane Detector System

The focal plane detector (FPD) system, shown in figure 3.5, consists of a multi pixel silicon p-i-n–diode array detector, readout electronics, two superconducting solenoid magnets, a high-vacuum and an ultra high-vacuum system, calibration and monitoring devices, a scintillating veto, as well as a data-acquisition (DAQ) system. The two

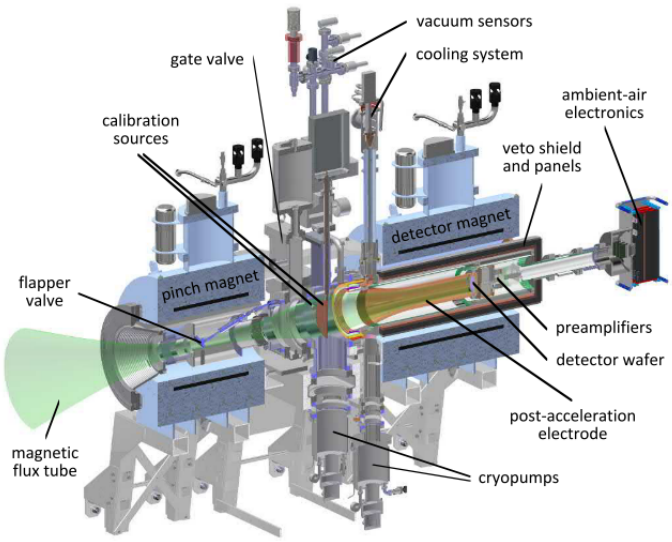

Figure 3.5: Focal plane detector system (left) and the silicone detector wafer (right). In the FPD system two superconducting solenoid magnets, namely the pinch and the detector magnet, reduce the diameter of the magnetic flux tube. The magnetically guided electrons traverse the post-acceleration electrode. By accelerating the signal electrodes, the signal-to-noise ratio is enhanced and backscattering on the detector is reduced. Figure from [Erh16].

Table 3.1: Pixel segmentation of the focal plane detector. Different combinations of the pixels are used in the analysis. Ring 0 denotes the bull's eye composed of four pixels. All other rings comprise twelve pixels. Ring 12 is the outermost ring. Measurement-specific pixel cuts can exclude certain pixels or rings. Pseudo-rings combining three rings provide a larger statistic and a clearer overview over the results. Since each pixel covers the same area their increase in radius decreases for higher ring-numbers.

Ring	Pseudo-ring	Pixels	Outer bound radius / mm
0	0	0 - 3	7.398
1	0	4 - 15	14.796
2	0	16 - 27	19.573
3	1	28 - 39	23.394
4	1	40 - 51	26.674
5	1	52 - 63	29.592
6	2	64 - 75	32.245
7	2	76 - 87	34.699
8	2	88 - 99	36.990
9	3	100 - 111	39.146
10	3	112 - 123	41.190
11	3	124 - 135	43.137
12	3	136 - 147	45.000

magnets are the 4.2 T pinch magnet and the 2.52 T detector magnet, aligned as shown in figure 3.5. Furthermore a post-acceleration electrode (PAE) is build into the system for an improved background discrimination. For this purpose it increases the electron energies by 10 keV which reduces backscattering and increases the signal-to-noise ratio because of the relatively low energy resolution of the detector of about 1 keV. To prevent accumulating a background from external particles the FPD system is passively shielded by lead and copper. Plastic scintillators additionally act as an active veto necessary for the cosmic ray background.
The **FPD** itself exhibits a diameter of 9 cm diameter and a thickness of 500 µm. Its detection surface is sectioned into 148 equal-sized pixels. The pixels form twelve rings around the four bullseye pixels, while consisting of twelve pixels each. The bull's eye is denoted as ring 0. This configuration is shown in figure 3.5. It allows for resolving radial and azimuthal effects in the beamline, which is among other things crucial for the investigation of the source potential in the WGTS. Additional, four pseudo-rings can be defined by combining three rings for each pseudo-ring, as listed in table 3.1. Due to the strong magnetic field in the beam line the electrons are mapped onto the FPD. However, since the alignment of the experiment is not perfect the center particles do not hit the exact center of the detector. Thus, some of the outer pixels cannot be used. However, it can be compensated for the imperfect alignment to some extend in the data analysis [Ost20, Def17, Hac17].

3.2 Data Analysis

The KATRIN experiment consists out of a wide range of components and can be operated in various settings. Therefore lots of operating parameters and sensor data must be taken into account for the analysis of the resulting count rate. This can only be achieved by developing a model for the expected count rate $N_{\mathrm{theo},i}$ for i settings of the retarding energy eU_i, which reflects all those different parameters. Originally, the data is the result of the radioactive β-decay, thus, the signal is of statistical nature. Therefore it obeys a Poissonian distribution, which defines the statistical uncertainties on the count rates. To match the theoretical predictions to the experimental conditions, different parameters are used. For characteristics of the spectrum, which are of interest but are not known well enough, free parameters are used. Common free parameters in the KATRIN analysis are among others the background rate R_{bg}, the intensity of the spectrum I and certain positions in the spectrum, such as the endpoint of the β-spectrum E_0 [Mac16, Kle14]. There are also spectrum characteristics, which need to be considered for the analysis but are not of interest, because no information can be gained from them. Those are represented by so-called nuisance parameters.
To determine the parameters of interest, a comparison between the obtained experimental count rate and the count rate predicted by the model is necessary. For this, a Bayesian or frequentist approach can be chosen. While the frequentist approach interprets probability as the relative frequency of the results of many independent events, the Bayesian approach takes a degree of belief into account. For the Bayesian approach

it is therefore necessary to make assumptions on the parameters beforehand by using a prior. Despite their different approaches both methods coincide with each other for the KATRIN data analysis, which is elaborated in [Kle14].

3.2.1 Likelihood Function

Because it is known that the signal of the KATRIN experiment follows a Poissonian statistic, a frequency distribution of a set of parameters P after an infinite amount of measurements can be predicted. It is referred to as the likelihood L, which is the likelihood of observing the count rate x_i for i settings of the retarding energy eU_i under an assumed probability density function (PDF). It is described by a model f depending on a set of parameters P and a total number of retarding energies n:

$$L(P) = \prod_{i=1}^{n} f(x_i; P)\,. \tag{3.7}$$

For the KATRIN experiment f is represented by a Poissonian distribution.
Due to the statistical fluctuations of P the likelihood function may extend to non physical regions of a parameter. In this case a mathematical continuation of the model is needed.
The Poissonian distribution of the individual number of integrated counts $N_{\text{obs},i}$ for a given retarding potential qU_i and measurement time t_i can be approximated by a Gaussian if the number of signal events is sufficiently large ($\gtrsim 25$). Hence, the likelihood function can approximately be described as product of Gaussian distributions for each measurement point $N_{\text{obs},i}$ [Mac16, Kle14]:

$$L(N_{\text{obs},i}, N_{\text{theo},i}(P)) = \prod_{i=1}^{n} \frac{1}{\sigma_i\sqrt{2\pi}} \exp\left[-\frac{1}{2}\left(\frac{N_{\text{obs},i} - N_{\text{theo},i}(P)}{\sigma_i}\right)^2\right]\,. \tag{3.8}$$

Following from Poissonian statistics, the weights can be derived as

$$\sigma_i = \sqrt{N_{\text{theo},i}(P)}\,. \tag{3.9}$$

Due to computational advantages it is common to search for the global minimum of the χ^2 function instead of maximizing L. It is given as

$$\chi^2 = -2\log L = \sum_{i=1}^{n}\left(\frac{N_{\text{obs},i} - N_{\text{theo},i}(P)}{\sigma_i}\right)^2\,. \tag{3.10}$$

This function is also known as the Pearson's χ^2-statistic or weighted least square [Pla83].
Resulting from the experiment is a set of parameters P minimizing χ^2 as well as a declaration of the corresponding confidence intervals.

Pull Term Method

Additional information about a parameter ψ can be added in form of a pull term. Since a successful search for the global minimum strongly depends on the start values for P, this method can prevent finding only a local minimum. When deploying this method, a penalty term is introduced preventing strong deviations away from the best estimated value $\hat{\psi}$. This penalty or pull term is normalized by its uncertainty σ_ψ and functions as an extension of the χ^2 [Kle14]:

$$\chi^2 = \sum_{i=1}^{n} \left(\frac{N_{\mathrm{obs},i} - N_{\mathrm{theo},i}(P)}{\sigma_i} \right)^2 + \left(\frac{\hat{\psi} - \psi}{\sigma_\psi} \right)^2 + ... \tag{3.11}$$

3.2.2 Statistical and Systematic Uncertainties

Besides the parameter values also statistical and systematic uncertainties are obtained when minimizing χ^2 which are crucial for the interpretation of the resulting values for P. The statistical uncertainty $\sigma_{\mathrm{stat},p}$ of a parameter p corresponds to the second derivative around the minimum of χ^2 as a function of p [Lis17]. Systematic uncertainties $\sigma_{\mathrm{sys},p}$ can be interpreted as an effect on the estimates of free parameters causing a shift of the χ^2 parabola. Alternatively, the pull method can be used to determine the size of the systematic uncertainties. Here, the width of the χ^2 parabola changes in comparison to the purely statistical width in positive or negative direction. This can be used to decrease the uncertainty on a parameter if the uncertainty of the pull term σ_ψ is known from a more sensitive experiment.

For Gaussian distributed values the uncertainties can be given in form of a standard deviation σ. One standard deviation includes 68.27 % of all measured values. It is also common to use confidence intervals of multiple σ.

Due to the Poissonian distribution caused by the radioactive decay process, the counts N are proportional to the total measurement time t_{tot}. Using this, equation 3.9 can be transformed to the statistical uncertainty:

$$\sigma_{\mathrm{stat}} \propto \frac{1}{\sqrt{t_{\mathrm{tot}}}} \,. \tag{3.12}$$

This holds if the parameter enters the model linearly, e.g. this holds for m_ν^2, not m_ν. Since many systematic effects not necessarily follow a Gaussian distribution, the central limit theorem is a useful way to combine them. It states that the quadratic sum of all effects including possible correlations can be approximated to a Gaussian distribution with the error $\sigma_{\mathrm{sys,tot}}$. Since statistic and systematic uncertainties are not correlated by definition, the total uncertainty can be written as:

$$\sigma_{\mathrm{tot}} = \sqrt{\sigma_{\mathrm{stat}}^2 + \sigma_{\mathrm{sys,tot}}^2} \,. \tag{3.13}$$

The Sensitivity on the Electron Antineutrino Mass at the KATRIN experiment

The KATRIN experiment is designed to reach a sensitivity of $0.2\,\mathrm{eV/c^2}$ (90 % C.L.), which corresponds to 5σ discovery potential of $0.35\,\mathrm{eV/c^2}$ [AAB+04]. In the following, the assumptions leading to this sensitivity are introduced shortly and set in context of the recent status of the experiment.

In the KATRIN design report a background rate of 10 mcps has been assumed. After three years of measurement time using a measurement interval of $[E_0 - 30\,\mathrm{eV}, E_0 + 5\,\mathrm{eV}]$, a statistical uncertainty of

$$\sigma_{\mathrm{stat}} = 0.018\,\mathrm{eV^2/c^4} \tag{3.14}$$

can be predicted. Additionally, five major sources for systematic uncertainties have been expected. It is presumed that they individually contribute less than $0.0075\,\mathrm{eV^2/c^4}$ to the total systematic uncertainty budget. Combining them as uncorrelated systematic effects, one finds

$$\sigma_{\mathrm{sys,tot}} = 0.017\,\mathrm{eV^2/c^4}\,. \tag{3.15}$$

Combining statistical and systematic uncertainties using equation 3.13, it follows

$$\sigma_{\mathrm{tot}} = 0.025\,\mathrm{eV^2/c^4}\,. \tag{3.16}$$

The corresponding sensitivity results to be

$$L(90\,\%\,C.L.) = \sqrt{1.64 \cdot \sigma_{\mathrm{tot}}} \approx 200\,\mathrm{meV}, \tag{3.17}$$
$$L(5\sigma) = \sqrt{5 \cdot \sigma_{\mathrm{tot}}} \approx 350\,\mathrm{meV}. \tag{3.18}$$

During the ongoing research it has been discovered, that the background exceeds its assumed rate by a factor 50 [Frä17]. This only leads to a slight decrease in sensitivity of $240\,\mathrm{meV/c^2}$ (90 % C.L.) when being counterbalanced with an optimised measurement time distribution and the use of an increased magnetic field strength in the analysing plane [Tro18]. Additionally, new sources of systematic uncertainties have been discovered, which need to be considered in the systematic uncertainty budget [SM19]. This thesis will concentrate on the systematic contributions caused by inhomogeneities of the source potential.

Weighted average for asymmetric statistical errors

When using the Poisson likelihood L to determine the values of a set of parameters, the profile of the log-likelihood $\ln L$ allows to determine the corresponding uncertainties with

$$\Delta \ln L = -\frac{1}{2}\,. \tag{3.19}$$

Since the profile of the log-likelihood is not a symmetric parabola asymmetric errors arise from equation 3.19. This is especially relevant if the number of results N, the number of terms contributing to the sum which makes up the log-likelihood, is small. In the limit of a large number of results N, the profile of the log-likelihood becomes parabolic [Bar04]. In practice, the Minuit processor MINOS is able to determine the asymmetrical errors during the fitting procedure. Since this calculation is time intensive it is only applied to parameters of interest. For the other parameters the log-likelihood profile is simply assumed to be symmetrical which gives symmetric errors.
For combining results with asymmetric errors $x_{i}{}^{+\sigma_i^+}_{-\sigma_i^-}$ one needs to use a weighted average which takes the asymmetry of the log-likelihood profile into account. If the profile of the log-likelihood is not analytically known an approximation describing the profile can be used. For this purpose [Bar04] suggests the form

$$\ln L(\hat{x}, x) = -\frac{1}{2} \frac{(\hat{x} - x)^2}{\sigma^+\sigma^- + (\sigma^+ - \sigma^-)(x - \hat{x})} \, . \tag{3.20}$$

It can be shown that indeed the likelihood function for a result $\hat{x}$ from a true value x can be described by a Gaussian with its width depending on x with good accuracy. This ansatz leads to an iterative equation for the weighted average [Bar04]

$$\hat{x} \sum_i w_i = \sum_i w_i \left(x_i - \frac{\sigma_i^+ - \sigma_i^-}{\sigma_i^+ \sigma_i^-} (\hat{x} - x_i)^2 \right) \tag{3.21}$$

with the weights

$$w_i = \frac{\sigma_i^+ \sigma_i^-}{\left(\sigma_i^+ \sigma_i^- + (\sigma_i^+ - \sigma_i^-)(\hat{x} - x_i)\right)^2} \, . \tag{3.22}$$

For the average value equation 3.21 must be normalised by the sum of the weights w_i. $\hat{x}$ can be approximated by $\frac{1}{N} \sum_i x_i$.

In case of a distribution of results for one parameter being cut off at a set value, this calculation cannot be used. Not only the values of the results are limited by the cut-off, but also the asymmetric errors. Therefore, the errors towards the cut-off can become much smaller than the opposing error without being statistically more significant. This causes a distortion of the averages when treating the cut-off errors as real errors and using equation 3.21. For this reason as an approximation only the error away from the cut-off is used as an symmetric error.

Chapter 4

Krypton Mode of the KATRIN Source for Investigation of the WGTS Plasma Potential

As a nuclear standard ^{83}Kr is used for calibration purposes in various experiments in astroparticle physics [SBB$^+$20, AAA$^+$18, EEF$^+$01]. Based on this experience ^{83}Kr also finds application in the KATRIN experiment for various investigations along the beamline. In this thesis, it is primarily used to determine systematic effects caused by inhomogeneities of the source potential.
In section 4.1 an introduction into the ^{83}Kr spectrum and its possible applications in the KATRIN experiment is given. Section 4.2 focusses on general plasma properties, as well as on specific plasma effects in the WGTS. Further information about the analysing software and procedures used for the krypton mode are presented in section 4.3.

4.1 Properties of ^{83m}Kr and Applications in the KATRIN Experiment

The Krypton Spectrum

^{83}Kr is characterized by emitting quasi-monoenergetic electrons. As visualized in figure 4.1, the metastable ^{83}Kr is produced by ^{83}Rb via electron capture. The efficiency for this transition amounts to $\sim 74\,\%$. ^{83}Rb disintegrations can also bypass the isomeric state of ^{83}Kr [DKS64]. The nucleus of ^{83}Kr de-excites through two γ-transitions. This energy E_γ is most commonly not released in form of photons but is transmitted onto the shell electrons by internal conversion. Depending on the shell and therefore on the binding energy of the electron $E_{\mathrm{ce}}(\mathrm{bind})$, electrons of different energy are created. Therefore the **electron energy $\boldsymbol{E_{\mathrm{ce}}}$** can be calculated as

$$E_{\mathrm{ce}} = E_\gamma + E_\gamma(\mathrm{recoil}) - E_{\mathrm{ce}}(\mathrm{bind}) - E_{\mathrm{ce}}(\mathrm{recoil})\,, \tag{4.1}$$

where $E_\gamma(\mathrm{recoil})$ stands for the recoil energy after the emission of the γ ray and $E_{\mathrm{ce}}(\mathrm{recoil})$ for the recoil energy after the emission of the conversion electron. The res-

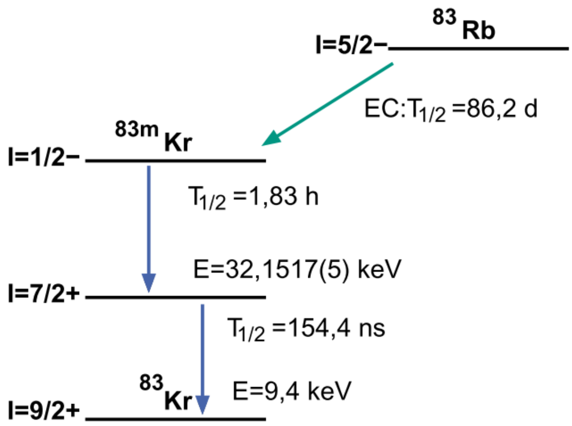

Figure 4.1: Decay scheme of ^{83m}Kr from its mother isotope ^{83}Rb. ^{83}Rb is transformed into the excited ^{83m}Kr state by electron capture. The de-excitation takes place in two steps with different transition energies E and life-times $T_{1/2}$. The angular momentum is decribed by the quantumn number I. Figure from [Ost08], modified.

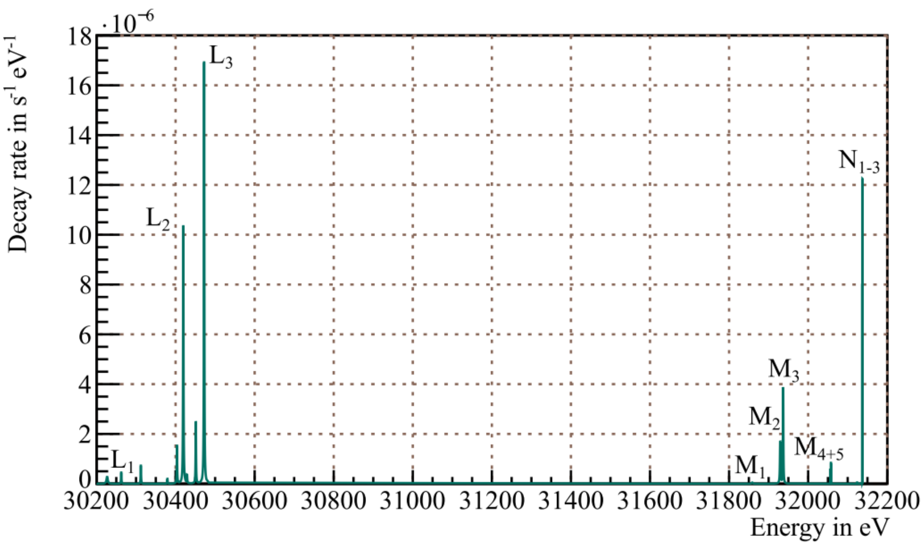

Figure 4.2: Internal conversion line spectrum of ^{83m}Kr for shells L, M and N. The differential decay rate per atom is at its mean inversely proportional to the corresponding line width. This explains why a high decay rate for the N lines is visible even though its total intensity is one magnitude smaller compared to the L and M lines. Figure from [Mac21a].

ulting discrete energy lines in the spectrum are named after their originating shell, K, L, M or N, and are within one shell enumerated by their order of appearance in the spectrum. Thus, N_1 is the first line of electrons from the N shell [VSD+18]. The ^{83}Kr line spectrum is visualized in figure 4.2.

In this thesis, only the transition of ^{83}Kr from the state $I = 1/2^-$ to $I = 7/2^+$ is considered. With its de-excitation energy of 32.15 keV it provides the electron lines for all shells above the K shell to lie at higher energies than the tritium endpoint. In contrast, the transition from $I = 7/2^+$ to $I = 9/2^+$ only shows a de-excitation energy of 9.4 keV, which results in an overlap of the electron lines with the β-spectrum and would hinder the analysis. Consequently, only lines from the 32 keV transition are used in the analysis of this thesis and are named neglecting the transition suffix, thus, $N_2 - 32$ is denoted only by N_2. Analysis of the 9 keV transition lines at KATRIN can be found in [SM19].

The **intensity of the lines** is determined by the rate of conversion, expressed by the internal conversion coefficient α. Since α depends not only on the shell but furthermore on the atomic structure of the regarding nucleus, there is no simple theoretical formula for it. For obtaining reliable results extensive theoretical calculations need to be performed for each shell and atom separately [KBT+08, RFAP78]. Experimentally α can be empirically determined by measuring

$$\alpha_i = \frac{\dot{N}_{i,\mathrm{e}}}{\dot{N}_{i,\gamma}}, \quad i \in K, L, M, N\,. \tag{4.2}$$

Here, $\dot{N}_{i,\mathrm{e}}$ and $\dot{N}_{i,\gamma}$ symbolize the rate of emitted conversion electrons and photons of shell i, respectively.

Additionally to the spectrum of the conversion electrons, satellite lines are produced by **shake up/off effects**. When ^{83}Kr emits an electron due to internal conversion, the distribution of the electric potential of the atom changes rapidly. This leads to an adaptation and rearrangement of the shell electrons. In this process a shell electron can get excited, either to a higher state, called shake up, or to the continuum, called shake off. This causes an energy reduction of the emitted conversion electron according to energy preservation and therefore a low-energy satellite line with the same shape as its main line for the shake up effect. The shake off effect produces a low-energy tail of the satellite line since a continuous range of excitation energies can occur. Since the probabilities for the shake lines are not negligible they must be considered in the modelling of the krypton spectrum [AAK+85]. Satellite lines for the ^{83}Kr L_3 lines are expected to be shifted by $\sim$ 20 eV compared to their main line [Mac21a, SM19, WBB+91].
All literature values of the relevant line properties are summarised in table 4.1.

Table 4.1: Line properties of the ^{83}Kr conversion electrons for the 32 keV transition for shells K to N. The mean conversion electron energy E_{ce}, which can be associated with the absolute line position, and its contribution of the binding energy E_{ce}(bind) is listed. The uncertainty on the absolute line position is comparably large due to the uncertainty on the transition energy. The binding energy is known with more precision and can be used to determine the relative line positions with an improved uncertainty, using equation 4.1. For this, the recoil energies are required to be equal. Furthermore, the currently best values for the natural line width Γ_{ce}, the theoretical conversion coefficient α_{theo} and the resulting intensity I_{ce} per decay are presented. The values are taken from [VSD+18, Ost08, CP01].

Line	E_{ce} / eV	E_{ce}(bind) / eV	Γ_{ce} / eV	α_{theo}	I_{ce} per decay / %
K	17 824.2(5)	14 327.26(4)	2.70(6)	478.0(50)	24.8(5)
L_1	30 226.8(9)	1924.6(8)	3.75(93)	31.7(3)	1.56(2)
L_2	30 419.5(5)	1731.91(6)	1.165(69)	492.0(50)	24.3(3)
L_3	30 472.2(5)	1679.21(5)	1.108(13)	766.0(77)	37.8(5)
M_1	31 858.7(6)	292.74(29)	3.5(4)	5.19(5)	0.249(4)
M_2	31 929.3(5)	222.12(17)	1.230(61)	83.7(8)	4.02(6)
M_3	31 936.9(5)	214.54(11)	1.322(18)	130.0(13)	6.24(9)
M_4	32 056.4(5)	95.036(23)	0.07(2)	1.31(1)	0.0628(9)
M_5	32 057.6(5)	93.79(2)	0.07(2)	1.84(2)	0.0884(12)
N_1	32 123.9(5)	27.52(1)	0.40(4)	0.643(6)	0.0255(4)
N_2	32 136.7(5)	14.67(1)	$\lesssim$ 0.03	7.54(8)	0.300(4)
N_3	32 137.4(5)	14.00(1)	$\lesssim$ 0.03	11.5(1)	0.457(6)

The ^{83}Kr line spectrum results from quasi-monoenergetic conversion electrons. Since the width of a line can be obtained by the Heisenberg uncertainty principle connecting the life time of an atomic state τ to its energy uncertainty, it must be assumed that not all lines exhibit a perfect δ-function shape. Thus, the width can be described as

$$\Gamma_{ce} = \frac{\hbar}{\tau}\,, \tag{4.3}$$

with $\hbar$ being the reduced Planck constant. By solving the time dependent Schrödinger equation the natural line shape results to be a Lorentz profile

$$L(E, E_{ce}, \Gamma_{ce}) = \frac{\mathrm{d}N}{\mathrm{d}E} = A\frac{\Gamma_{ce}}{2\pi}\frac{1}{(E - E_{ce})^2 + \Gamma_{ce}^2/4}\,. \tag{4.4}$$

E_{ce} symbolizes the mean energy of the peak, or in other words the energy of the conversion electron as expected for a monoenergetic line [Hua10, WW97]. In the experimental context systematic effects on the overall line broadening need to be considered. To describe those systematic effects a Gaussian distribution such as

$$G(\Delta E, \sigma^2) = \frac{1}{\sqrt{2\pi\sigma^2}}\exp^{-\frac{\Delta E^2}{2\sigma^2}}\,, \tag{4.5}$$

with a FWHM of $\Gamma_{\mathrm{G}} = \sqrt{8\ln(2)}\sigma$ is used. The standard deviation of the distribution is then applied to the analysis of the tritium spectrum to quantify a possible shift of the neutrino mass value. In order to allow for those systematic effects to influence the overall line shape the natural Lorentzian line can be convolved with a Gaussian, resulting into a Voigt profile

$$V(E, E_{\mathrm{ce}}, \sigma^2, \Gamma_{\mathrm{ce}}) = \int_{-\infty}^{\infty} \mathrm{d}E' G(E', \sigma^2) L(E - E', E_{\mathrm{ce}}, \Gamma_{\mathrm{ce}})\,. \tag{4.6}$$

The FWHM of the Voigt profile can approximately be described by [OL77]

$$\Gamma_{\mathrm{V}} \approx 0.5346\Gamma_{\mathrm{G}} + \sqrt{0.2166\Gamma_{\mathrm{ce}}^2 + \Gamma_{\mathrm{G}}^2}\,. \tag{4.7}$$

Overall, the properties of ^{83}Kr are well suited for the use in the KATRIN experiment: ^{83}Kr provides monoenergetic electron lines which are needed for calibration purposes. The conversion electron energies lie with 11 652 eV (L_1) to 13 563 eV (N_3) relatively close above the tritium endpoint and can therefore be measured with the experimental setup. Furthermore, the half life time of ^{83}Kr of 1.83 h avoids a long term contamination of the experiment. Since the mother isotope ^{83}Rb shows a relatively long half-life time of 86.2 d the source can be used for several weeks. Most importantly, ^{83}Kr is gaseous and can therefore be injected into the source [VSD$^+$18]. This property is crucial for measuring the source potential.

General Applications of the Krypton Mode

The discussed properties of ^{83}Kr allow to investigate a variety of systematic effects along the beam line of the KATRIN experiment. The most prominent purpose for investigations with ^{83}Kr is determining longitudinally and radially dependent source potential properties in the WGTS. Those studies are critical for the neutrino mass measurements since the source potential is the starting potential for the β-electrons and thus affects the recorded spectrum. Therefore, section 4.2 provides a deeper insight into the properties and measurements of the plasma potential. Besides that, ^{83}Kr measurements can be used to optimize and test new measurement procedures, and can help to find systematic contributions along the beamline for which one has to account for in the analysis. A detailed description and discussion of studied systematic effects can be found in sections 5.1 to 5.3.

4.2 Plasma Potential and related Systematic Shifts of the Neutrino Mass

General Plasma Properties

In comparison to other plasmas the KATRIN source plasma exhibits uncommon **properties**, as can be seen in figure 4.3. Since plasmas are characterized by their collective

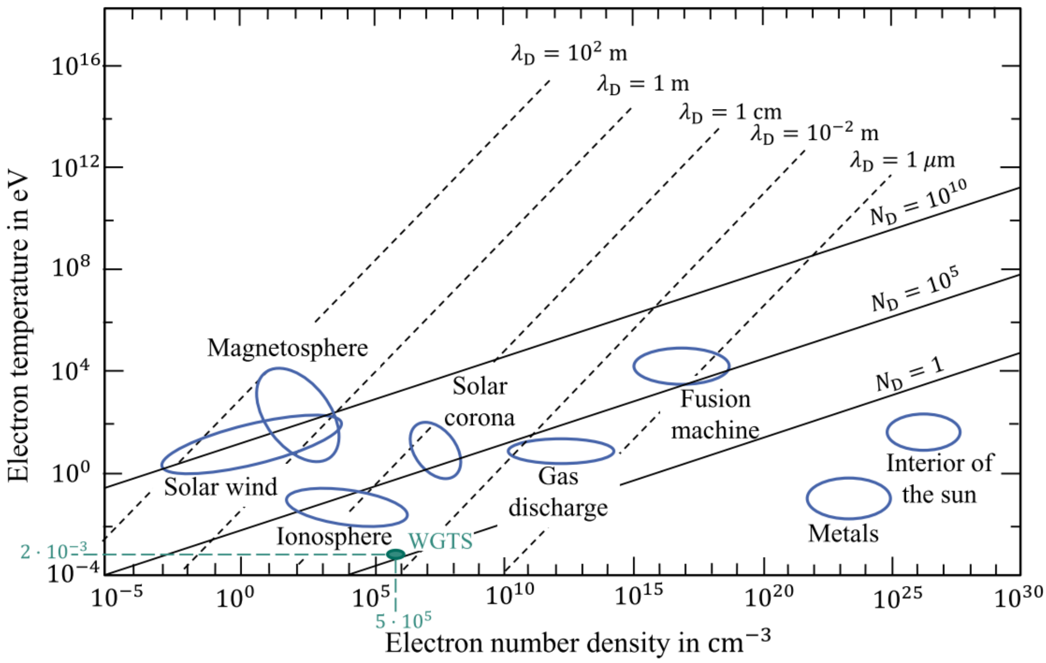

Figure 4.3: Comparison of the KATRIN source plasma to common plasmas. The KATRIN source plasma exhibits an uncommonly low electron temperature. In combination with its electron number density, it shows a rather small plasma parameter N_D. As a consequence, it is on the edge of being an ideal plasma[(1)] [Kuc16, DKMS05]. Figure from [Mac21a], found in [Gal12], idea from [Kuc16], original source unknown.

(1) A plasma is called ideal, if the mean thermal energy of the particles exceeds the mean electrostatic interaction energy [DKMS05].

behaviour of the contributing particles, collective parameters are used for their description [DKMS05]. One decisive parameter of a plasma is its temperature. Even compared to low temperature plasmas with around 10^4 K [DKMS05] the KATRIN source plasma shows an extremely low temperature of only 80 K. The electron density for the WGTS lies at the order of $n_e = 5 \times 10^{11}\,\mathrm{m}^{-3}$ [col04], which is to be classified at the lower end of overall plasma electron densities varying from $10^5\,\mathrm{m}^{-3}$ to $10^{35}\,\mathrm{m}^{-3}$ [DKMS05]. Additionally, the density gradient along the WGTS introduces the evolution of different gas flow regimes. The center of the WGTS shows a hydrodynamic regime, which can be described by continuum mechanics. Towards the ends of the WGTS, especially close to the DPS2, a free molecular regime develops in which intermolecular collisions can be neglected. The transitional regime, must theoretically be described by solving the linearised Boltzmann equation.

Another characteristic of a plasma is its type of **creation process**. Commonly plasmas are induced by high temperatures or large external fields. In contrast, the KATRIN source plasma is generated by the tritium β-decay, which produces 10^{11} electrons and $^3(\mathrm{HeT})^+$ ions per second, and by inelastic scatterings of the electrons on the neutral gas components. During one scattering process one β-electron is able to generate on the order of 50 secondary electrons and ions [Mac21a]. Due to the fact, that almost

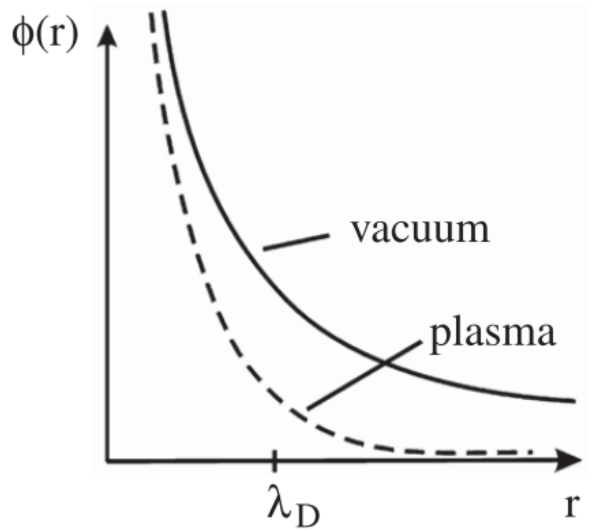

Figure 4.4: Potential distribution of an electric charge in vacuum and in plasma. The plasma potential declines faster with growing distance due to Debye shielding. Since it converges to zero, the plasma characterises as quasi-neutral. Figure from [DKMS05], modified.

all electrons are eventually reflected by the spectrometer and that the rear wall backscattering is on the order of several ten percent [Bab14], the electrons pass through the WGTS many times until they are absorbed at the rear wall. This way many low-energetic secondary electrons are produced, which contribute as thermalised particles to the plasma [SK20]. The ions resulting from the self-ionizing processes are T^+, He^+, $^3HeT^+$ and T_2^+. Chemical reactions or clustering processes can form higher order ions, resulting mainly in T_3^+ and T_5^+.
Relevant for the characterization of the KATRIN source plasma are also its **external influences and boundary conditions**. Those are mainly determined by the potentials of rear wall and beamtube, as well as by the strong longitudinal magnetic fields. The latter results in a small transversal electron mobility additional to their movement along the longitudinal axis. The electrons are able to leave the plasma by entering the rear wall. The movement of the ions is influenced by the rear wall and the DPS dipole electrodes. Radial drifts of the ions towards the beam tube wall are suppressed for the optimal rear wall voltage. This optimal rear wall voltage setting minimises the inhomogeneity of the source potential. It has been observed that the potential of the rear wall mainly influences the radial center of the source plasma while the beamtube potential shows a dominant influence for the outer radii. The effect scales with the set voltage of the rear wall relative to the beam tube.
In conclusion, there are four essential settings influencing the shape of the plasma potential: the temperature, the column density, the source magnetic field and the rear wall voltage.

One key effect determining the behaviour of a plasma is its quasi-neutrality on a macroscopic scale. This is caused by a shielding charged cloud surrounding oppositely charged particles. The exponentially shielding effect of the charged cloud is called **Debye shielding** and can be described via the Debye length

$$\lambda_{\mathrm{D}} = \sqrt{\frac{\epsilon_0 k_B T_{\mathrm{e}}}{n_{\mathrm{e}} e}}\,. \tag{4.8}$$

For the typical conditions in the WGTS, Debye lengths between 0.3 mm and 1 mm are reached [Kuc16]. The shielding effect on the potential of the ion follows

$$\phi(r) = \frac{q}{4\pi\epsilon_0}\frac{1}{r}\exp\left(-\frac{r}{\lambda_{\mathrm{D}}}\right) \tag{4.9}$$

and is visualized in figure 4.4. Defining a sphere with radius λ_{D} around the shielded particle one can obtain the number of particles within this so-called Debye sphere with

$$N_{\mathrm{D}} = \frac{4}{3}\pi n_{\mathrm{e}} \lambda_{\mathrm{D}}^3\,. \tag{4.10}$$

This is also called the plasma parameter [DKMS05].
An overriding mechanism for the generation of Debye spheres are clustering effects of correlated particles, which are close together in the phase space for a certain life time of the so-called clump. It can be found that a smaller clump size leads to a longer life time. For the case that one clump contains multiple Debye spheres, the effective plasma parameter can be enhanced by the number of particles in a clump N_c, resulting in $\Gamma_{\text{eff.}} = N_c/N_{\mathrm{D}}$. Overall clumps can be considered as generalised Debye spheres [MB78].

Plasma Investigations with Krypton

To experimentally understand the plasma potential in the WGTS and to obtain and monitor its properties, measurements with added krypton are necessary. By making use of the krypton line properties, such as the line position and line broadening, different plasma parameters can be obtained. Radially dependent plasma effects influencing those krypton line properties can be easily detected due to the radially aligned pixels of the detector. Thus, a radially shifting krypton line position would hint to a radial inhomogeneity of the plasma potential relative to the retarding potential. Another important parameter is the additional broadening σ to the krypton natural line width Γ by plasma-related inhomogeneities and instabilities. Its value is critical for the neutrino mass analysis since a broadening σ^2 of the energy distribution of starting β-electrons leads to a shift in the neutrino mass of [Mac21a]

$$\Delta m_\nu^2 = -2\sigma^2 - \epsilon_1 \cdot \Delta_{10}\,. \tag{4.11}$$

Additional to the broadening, the so-called energy loss shift of single scattered electrons Δ_{10} scaled by a proportionality factor ϵ_1 causes a shift of the neutrino mass. This parameter is of interest since it is the only parameter carrying information about

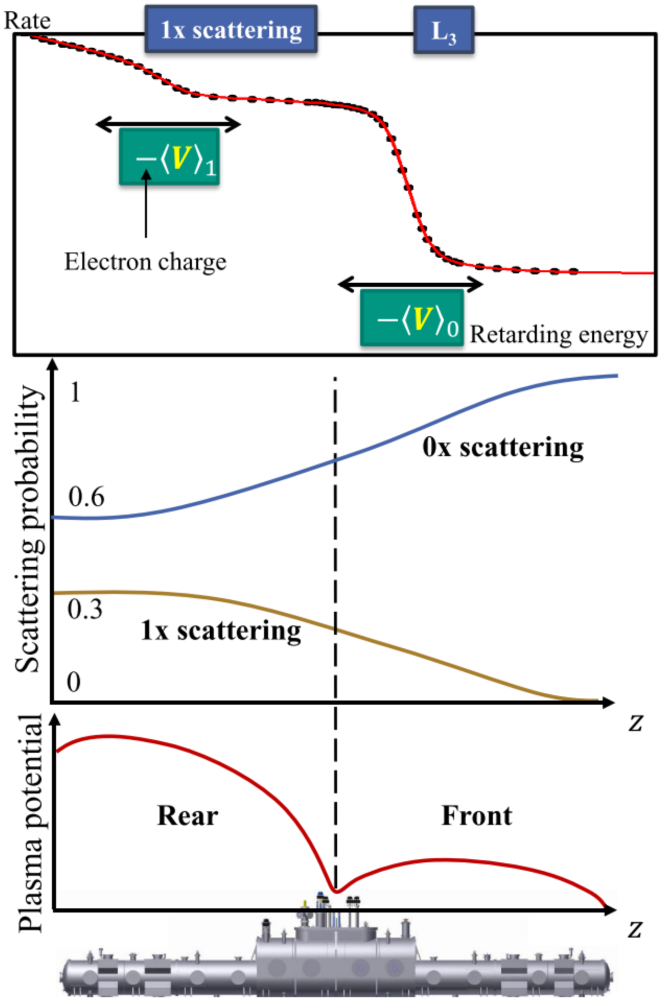

Figure 4.5: Sensitivity on the longitudinal source potential in the presence of inelastic scatterings. Since the scattering probability for a detected electron increases towards the rear part of the source, scattered electrons start in average closer to the rear end of the source in comparison to unscattered electrons. Therefore, their mean starting potential $\langle V\rangle_i$ differs for different scattering multiplicities i. Due to the negative charge of the electrons, a positive starting potential shifts the line position in negative direction. The mean starting potentials $\langle V\rangle_i$ can be directly measured with the krypton line spectrum as additional lines separated by their energy. Figure from [Mac21a].

the longitudinal plasma potential profile. Simulations show, that unscattered electrons mainly origin from the downstream end of the WGTS while single scattered electrons result mainly from the end of the WGTS close to the RW. This is visualised in figure 4.5. Therefore, electrons with different scattering multiplicities i experience a different mean starting potential $\langle V\rangle_i$ [Mac21a]. In the krypton line spectrum the scattered electrons generate a second line at lower energies towards their main line. A theoretical probability of a certain energy loss for i scattering processes is described by the energy loss function $f_i(\epsilon)$. It can experimentally be determined by e-gun measurements and

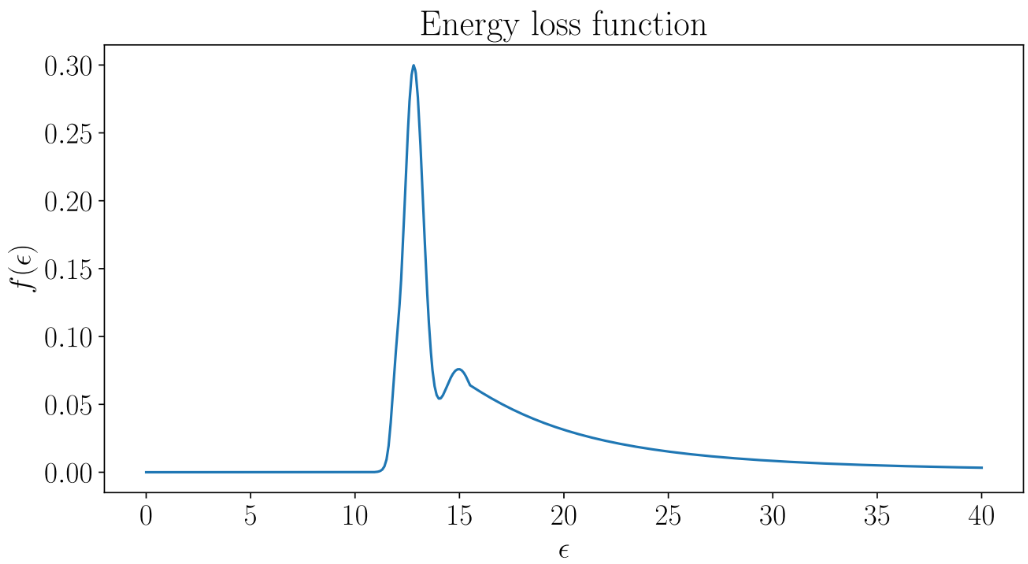

Figure 4.6: Energy loss function $f(\epsilon)$ for single scattered electrons, describing the probability for an electron of loosing the energy ϵ due to inelastic scattering on tritium molecules. It has been measured with the e-gun at 18 keV [ABB+21], but not at 32 keV. Since it is used as a reference value for Δ_{10}, this results in a possible source of systematic uncertainty in krypton measurements. Figure from [Böt20].

is shown in figure 4.6 for single scattered electrons.

Besides obtaining and monitoring the plasma potential with krypton measurements it is also possible to optimize the **RW voltage setpoint**. This is relevant for reducing the source potential inhomogeneities to a minimum by maintaining a maximally-coupled state between RW and plasma. The optimal rear wall voltage is defined as the work function difference between the rear wall and beam tube

$$\Delta\Phi_{\mathrm{RW-BT}} = \Phi_{\mathrm{RW}} - \Phi_{\mathrm{BT}}\,, \tag{4.12}$$

where Φ_{RW} and Φ_{BT} denote the work function of the rear wall and the work function of the beam tube, respectively. With this, an approximation for the mean plasma potential, and therefore for the mean start potential of unscattered electrons, can be derived as [Kle21c]

$$eU_{\mathrm{Pl}} = -\Phi_{\mathrm{BT}} + c_0 \cdot (eU_{\mathrm{RW}} - \Delta\Phi_{\mathrm{RW-BT}})\,. \tag{4.13}$$

Here, c_0 describes the coupling between the plasma and the rear wall, which can be in a maximally-, partially- or de-coupled state [Fri20]. U_{RW} denotes the rear wall voltage. More precisely, the coupling c_0 is defined as the derivative of the mean plasma potential for unscattered electrons with respect to the rear wall voltage

$$\frac{1}{e}\frac{\mathrm{d}eU_{\mathrm{Pl}}}{\mathrm{d}U_{\mathrm{RW}}} = c_0\,. \tag{4.14}$$

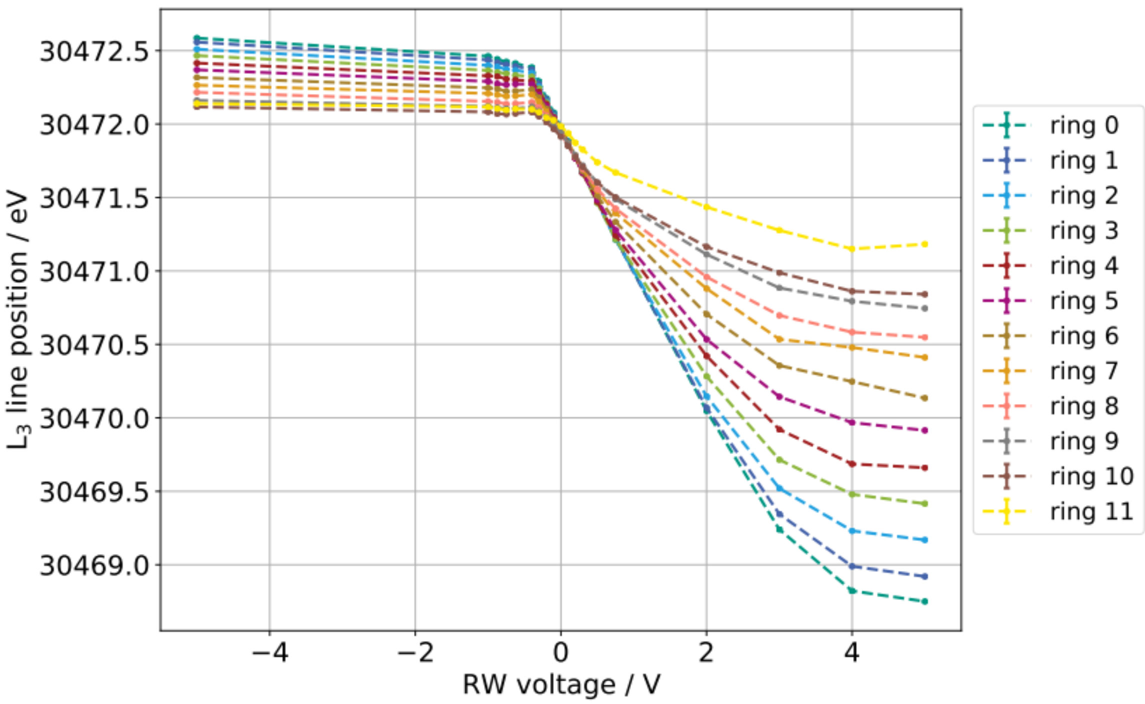

Figure 4.7: Exemplary analysis of the line position dependent on the rear wall voltage, using the L_3 line. The crossing point of the line positions is used to obtain the optimal rear wall voltage. Figure from [Ost20].

Therefore, it is assumed that the optimal setpoint for the RW voltage, where the standard deviation of the mean plasma potential over the rings is minimized, lies in the coupling region with $c_0 = 1$. Here, the plasma is in the maximally-coupled state towards the rear wall. In this ideal case it is expected that RW and beam tube show equal surface potentials and thereby a radially and longitudinally homogeneous plasma potential is reached [Kuc16].
When considering the measured current at the RW and DPS section I_{RW} and I_{DPS} one can equivalently derive the condition that the total WGTS current I_{WGTS} must be zero for the optimal RW setpoint [Kle21b]

$$I_{\mathrm{WGTS}} = |I_{\mathrm{RW}} - I_{\mathrm{DPS}}| \,. \tag{4.15}$$

A suboptimal setpoint of the RW voltage causes an inhomogeneous starting potential distribution of the β-electrons which leads to a significant systematic effect on the neutrino mass measurement [Mac21a, Kuc16].
Overall there are two different measurement approaches for obtaining the optimal RW setpoint. First, when performing so-called *IU* scans one can obtain the point with zero WGTS current. For those measurements different RW voltages U_{RW} are applied while monitoring I_{WGTS}. The second measurement approach uses krypton measurements at different RW voltage setpoints. In the analysis the line positions for each ring and RW setpoint are obtained and compared, as shown in figure 4.7. The crossing point of all

line positions gives the RW setpoint at which the same plasma potential prevails for all rings, giving a homogeneous plasma potential [Kle21a].

4.3 Analysis of the Krypton Spectrum with the KaFit Software Environment

4.3.1 The Software Environment for Spectrum Simulation and Analysis

For data simulations and analysis a versatile and flexible software environment is needed. In the KATRIN collaboration several equivalent software frameworks are used which are suitable for the experiment. Since KaFit features not only the simulation framework for the tritium β-spectrum but also for the krypton line spectrum, it is used for all krypton analysis in this thesis.
KaFit is one package of the parent KASPER framework, providing a unified analysis and simulation software environment developed by the KATRIN collaboration [Kle14, Beh16]. It is written in C++ and enables the individual installation of different packages depending on the respective preferences and needs. To provide more flexibility, simulation and analysis parameters are configured individually in .xml files. KASPER provides different packages covering details of the experimental setup, simulations of the physical processes and requirements for the analysis. For example the Kommon package is used for storing physical constants and to generate random numbers, KGeoBag contains the geometries of the experiment, KEMField calculates the electromagnetic fields in the experiment and Kassiopeia enables the tracking of charged particles in the electromagnetic fields [SM19]. Furthermore, the SSC package is essential for differential and integral spectrum calculations for tritium and krypton [KBD+19, Kle14, Höt12, Käf12]. The analytical spectrum calculations are extended to cover systematic effects like the gas dynamics in the WGTS [Kuc16]. Further systematic effects concerning the spectrum model are discussed in section 5.1. The by the SSC module calculated expected count rate can be used to study the influence of systematic effects on fit parameter sensitivities, for the analysis of measured data or as input for Kassiopeia simulations.
KaFit performs likelihood calculations and χ^2 minimisations based on the obtained expected count rate. This is done by comparing the SSC model to the measured data with χ^2 distribution analysis and Markov Chain Monte Carlo methods, allowing the extraction of the wanted parameters from the spectrum.

4.3.2 Model of the Krypton Mode

The analysis of the krypton line spectrum needs a reference model. This model is dependent on various physical processes in the WGTS influencing the distribution of transmitted electrons in the spectrometer. In the following the most relevant **model settings** are introduced. Their individual influence on the wanted line parameters is

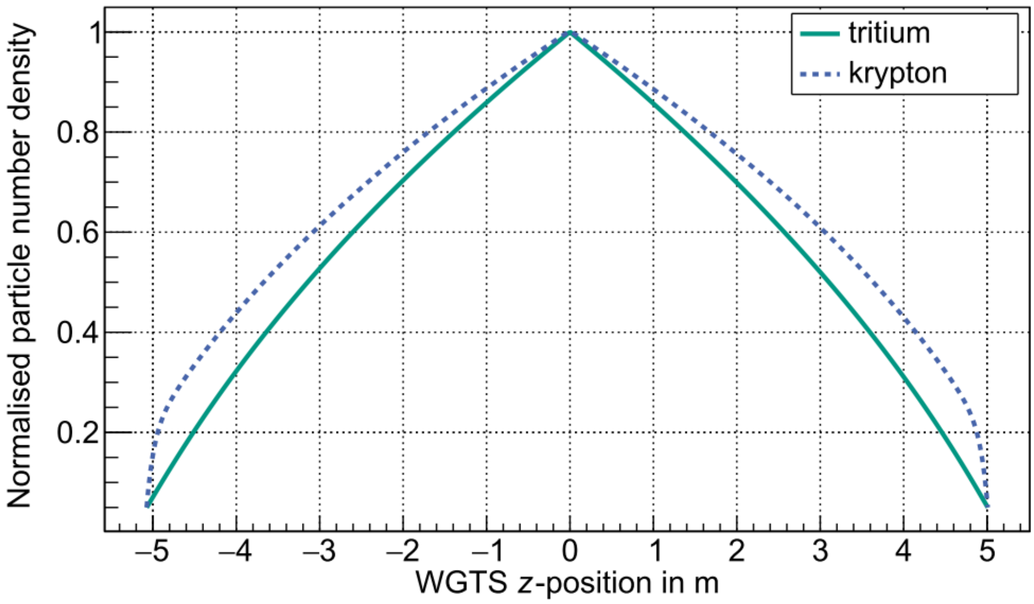

Figure 4.8: Gas density profiles for tritium and krypton at 110 K. The profiles are normalised by the maximum particle number density at the gas injection in the center of the WGTS. The different shapes are due to the different scattering probabilities of tritium and krypton. This leads to different starting potential distributions for both gases. Figure from [Mac16], modified.

analysed and discussed in subsection 5.2.2. Furthermore, the line and experimental parameters studied in subsection 5.2.1 are introduced.

Since the electrons move along the beam line guided by strong magnetic fields they emit synchrotron radiation. This causes an energy loss of the electrons which is relevant for higher order corrections of the transmission function. Therefore, the synchrotron radiation is considered in form of a corrected transmission function. This correction also includes relativistic effects. Another physical effect to be considered is the Doppler effect. It can be accounted for it in the model by introducing an extra Gaussian broadening of the energy scale. This is possible when only considering the projection of the Maxwell-Boltzmann distributed thermal velocity of the particles in the direction of movement, leading to a Gaussian distribution. In detail, the Doppler effect can be separated into two contributions: the thermal movement of the molecules and the bulk movement of the gas flow. Both contributions can be activated separately in the analysis. When modelling the gas density profile in the WGTS a simplified constant or an asymmetric simulated model can be chosen [KS10], as shown in figure 4.8. Moreover, scattering processes play a prominent role for the description of the spectrum. Therefore, the energy loss function of the electrons due to inelastic scattering must be implemented in the model. It is represented by a variety of parameters and correlation factors describing the energy loss for a certain range of energy. In this thesis the energy loss function of the third KATRIN neutrino mass measurement campaign

(KNM3) is used. It was measured at 18 keV. Since the Eloss function is dependent on the energy range using it for the analysis of the N lines at 32 keV might lead to small discrepancies. The measurement of the Eloss function for the 32 keV region is still pending. To estimate the magnitude and impact of this possible discrepancy the KNM1 Eloss function is used. This early Eloss function turned out to be slightly incorrect and can therefore be used to asses the impact of a false Eloss function in comparison to the KNM3 Eloss function. Additionally, changes of the transmission function due to secondary effects of i-times inelastic scattered electrons are covered in the model by the so-called detailed transmission [Gro15]. Here, i=0 for the detailed transmission denotes that only unscattered electrons are taken into account for the calculation. Respectively, i=1 also considers single scattered electrons for the detailed transmission.

In this thesis, only the **N lines** of ^{83}Kr are considered. Since they are the highest energy lines of the krypton spectrum, they come with special advantages and disadvantages. Former analysis of lower krypton lines have shown that they need to be analysed using a non-constant background [Gup21, Böt20, Ost20]. It has been determined that this background results from non-adiabatically transported electrons of higher energetic krypton lines. Therefore, not only the regarding line but also the background region must be measured to allow for a conclusive fit result, taking valuable measurement time. As the highest energetic krypton line the N lines are expected to have a constant background rate. Moreover, they profit from a low background rate of only 0.54 cps, as shown in figure 4.10. The background rate is scaled onto the full detector with its 148 pixels. Nevertheless, a small background slope of $m_{\mathrm{Bg}} = (0.37 \pm 0.05)$ mcps/V has been observed caused by using an experimental measurement mode, the IE mode. The different measurement modes are explained in subsection 4.3.3. The analysis of the background slope is shown in figure 4.10. Therefore, the influence of a background slope m_{Bg} on other parameters is studied for the N lines.
Furthermore, K, L and M lines show a significant natural line width, as shown in table 4.1. Since the natural line width Γ_{ce} and the Gaussian broadening σ_{G} are correlated, it is essential to know the exact value for Γ_{ce}. The larger the natural line width is compared to its Gaussian broadening, the more precisely Γ_{ce} needs to be known. Since the N lines are created by the electrons of the outermost krypton shell, which exhibits a comparably large lifetime, they are assumed to have a vanishing natural line width. Theoretical considerations limit Γ_{ce} to be smaller than 30 meV [VSD+18]. Furthermore, the natural line width depends on the neutralisation time of the excited krypton in the plasma. Collisions with the surrounding electrons can lead to a shorter lifetime and therefore to a broader natural line width of the regarding state of krypton. It is not possible to measure the natural line width of the krypton N lines with the experimental setup of KATRIN due to the additional Gaussian broadening and their strong correlation. Thus, a value for Γ_{ce} within the theoretical limit must be assumed in the analysis.
The major disadvantage of the N lines consists in their low statistic. Compared to L_3 line measurements the rate is reduced by around a factor of 60 [Ost20]. Additionally,

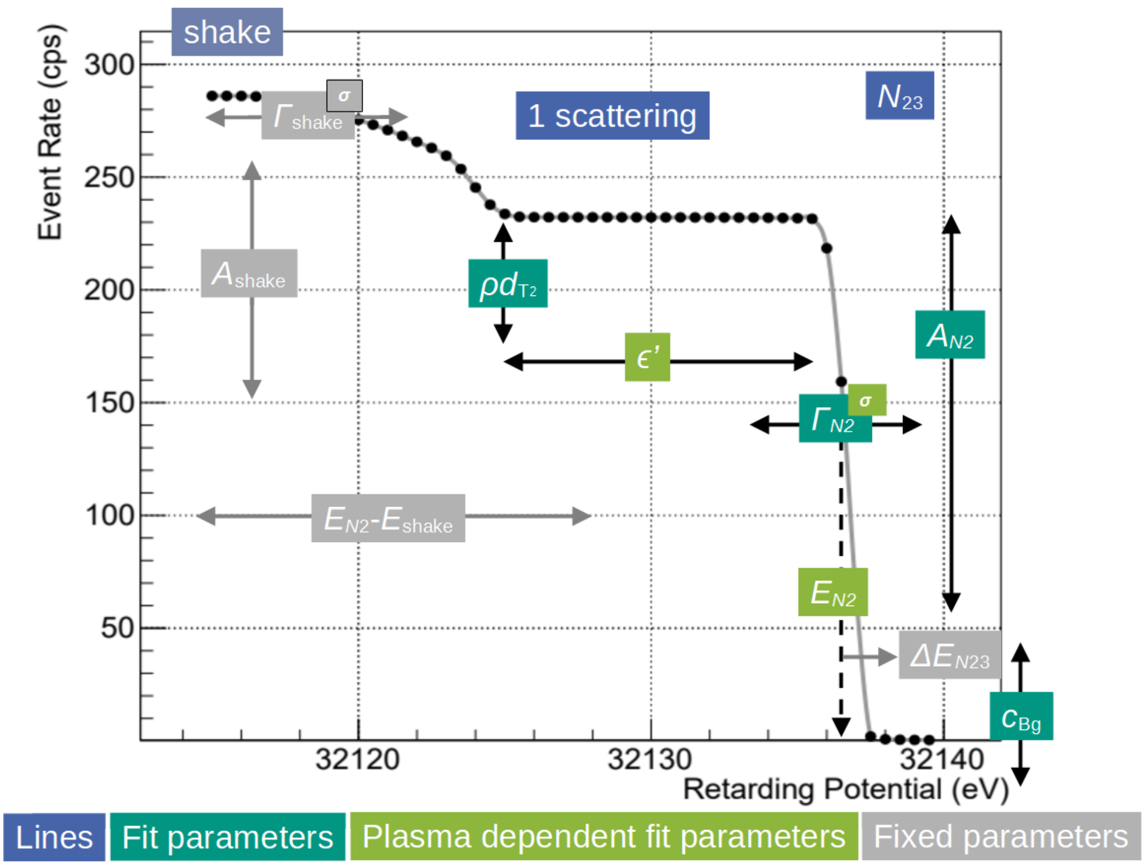

Figure 4.9: Observables of the krypton spectrum, shown for the N_{23} line. The main line is characterised by the parameters of the Voigt profile: the line position E_2, the amplitude A_{N2} and the natural line width Γ_{N2}. Since the N_{23} line is a doublet, the N_3 line properties are given relative to the N_2 line, e.g. the relative line position ΔE_{N23}. The spectrum can show additional line broadening σ due to plasma inhomogeneities or instabilities. Additionally, a background rate c_{Bg} must be considered. ϵ' gives the energy shift of the scattering peak relative to the main line. It equals the Eloss shift Δ_{10} plus a minimal energy loss of $\sim 13\,\mathrm{eV}$. The tritium column density can be fitted due to its linear dependency of inelastic scatterings on the gas. The shake lines must be considered if they overlap with the analysing interval. Figure inspired from [Ost20].

the energy loss region of the N_{23} lines is overlapping with the N_1 and satellite lines. Thus, for obtaining the energy loss shift Δ_{10} the properties of the underlying lines must be well known. Those lines can be measured by not using tritium in the source to avoid scatterings and by instead using helium as a carrier gas for krypton. The carrier gas is necessary to ensure a high krypton rate.

For the detailed analysis of the krypton N line spectrum, several **parameters and their uncertainties** must be considered. As a reference in the spectrum the N_2 line is chosen with a theoretical line position at $E_{N2} = 32\,136.72\,\mathrm{eV}$. In the analysis, the

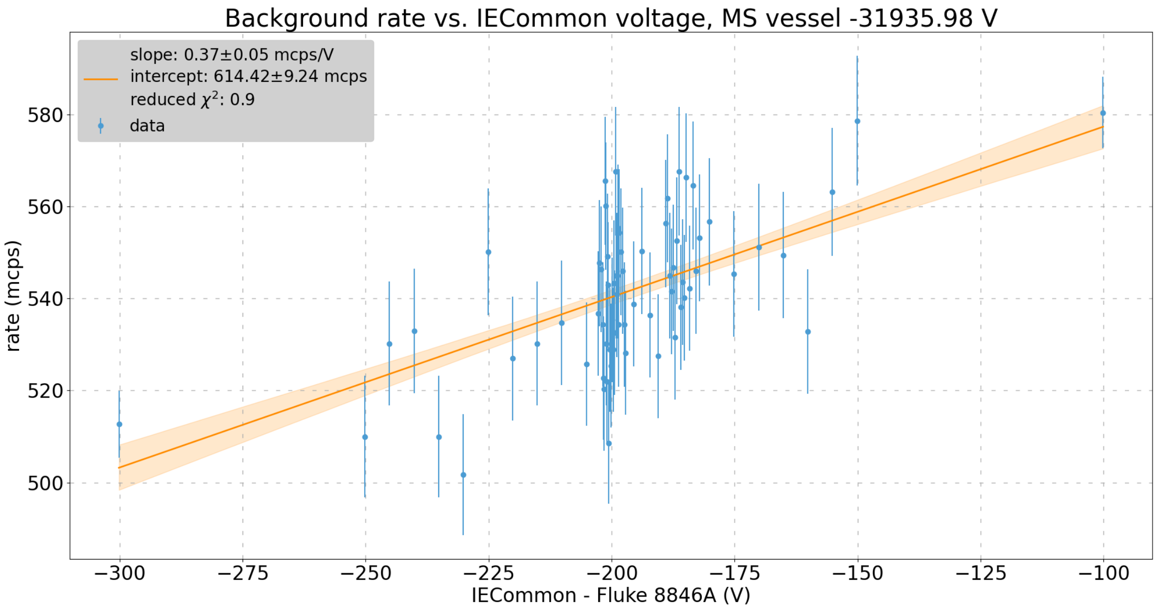

Figure 4.10: Background measurement with linear fit in the N line region for a fixed vessel voltage and varying IE voltages. The fit gives the expected background rate for the full detector of $c_{\mathrm{Bg}} = 0.54\,\mathrm{cps}$ and background slope of $m_{\mathrm{Bg}} = (0.37 \pm 0.05)\,\mathrm{mcps/V}$ for the N lines. Analysis by F. Fränkle.

theoretical N_2 line position is only used as a start value for the free parameter. The positions of the N_1 and satellite lines S_1 and S_2 of the N_{23} line doublet are fitted relative to the N_2 line. Even though this increases the uncertainty on the N_2 line position, this proceeding improves the fit performance. Consequently, the line intensities I are fitted as their normalised ratio I/I_{N2} relative to the N_2 line. The squared natural line width Γ^2 is fitted for each line individually. Though when fitting Γ^2, a pull term must be used due to the strong correlation towards the Gaussian broadening σ_{G}. Furthermore, experimental parameters which influence the transmission properties can be included in the analysis, such as the magnetic field strength in the source B_{src}, in the analysing plane B_{ana} or of the pinch magnet B_{pch}. Also, the source temperature T, influencing the Doppler effect and the gas dynamics in the source, and column density ρd, having an effect on scattering processes and gas dynamics, can be considered in the analysis with their uncertainties. Regarding tritium, its viscosity η is also a relevant quantity for the gas dynamics in the source, which needs to be known for the analysis.

Overall, there are a wide range of different parameters and model settings, whose influences need to be considered in the data analysis. A summary of those parameters with the regarding values and uncertainties used in this thesis can be found in table 4.2. Also, a selection of parameters is visualized on the spectrum of the N_{23} line in figure 4.9.

Table 4.2: List of fit parameter values and corresponding error contributions used for sensitivity studies. σ denotes the parameter uncertainty known from former measurements or literature [VSD+18]. Based on those values calculations by M. Böttcher give assumed parameter uncertainties σ_{He} after krypton line measurements conducted with helium instead of tritium. The reference N_2 line position is set to 32 136.72 eV. For parameters with pixelwise fitted values only the scale of the values is given. The exact values can be found in GlobalKNM3Simulation-PeriodSummary_Jul2020b_32000V_2.7G-000002.ktf. Besides the listed parameters the influence of the KNM3 energy loss function $f_1(\epsilon)$ has been studied. It consists of a range of parameters and correlation factors, which are used in the same configuration for the neutrino mass analysis.

Parameter	Absolute value	σ	σ_{He}
$\Delta E_{S1N2}/\mathrm{eV}$	-17.665	0.18	0.025
$\Delta E_{S2N2}/\mathrm{eV}$	-19.665	0.2	0.03
$\Delta E_{N12}/\mathrm{eV}$	-12.85	0.014	0.006
$\Delta E_{N23}/\mathrm{eV}$	0.67	0.014	0.000 17
I_{S1}/I_{N2}	1.0	0.1	0.0396
I_{S2}/I_{N2}	1.0	0.1	0.0158
I_{N1}/I_{N2}	1.0	0.1	0.003 52
I_{N3}/I_{N2}	1.0	0.2	0.000 256
$\Gamma^2_{S1}/\mathrm{eV}^2$	1.0	1.0	0.16
$\Gamma^2_{S2}/\mathrm{eV}^2$	1.0	1.0	0.12
$\Gamma^2_{N1}/\mathrm{eV}^2$	0.16	0.032	0.012
$\Gamma^2_{N2}/\mathrm{eV}^2$	0.0001	0.0001	0.0001
$\Gamma^2_{N3}/\mathrm{eV}^2$	0.0001	0.0001	0.0001
$m_{\mathrm{Bg}}/\mathrm{eV\,V^{-1}}$	0.000 37	0.000 05	
$B_{\mathrm{ana}}/\mathrm{T}$ (pixelwise)	∼0.000 27	5×10^{-6}	
$B_{\mathrm{pch}}/\mathrm{T}$ (pixelwise)	∼4.24	∼0.004 24	
$B_{\mathrm{src}}/\mathrm{T}$	2.51	0.032 63	
$\rho d/\mathrm{molecules\,m^{-2}}$	3.75×10^{21}	3.75×10^{19}	
T/K	78.8	1.5	
$\eta/\mathrm{Pa\,s}$	5.76×10^{-6}	5.76×10^{-7}	

4.3.3 Measurement and Analysis Settings for the Krypton N Lines

Before the analysed data can be discussed, several concepts and settings regarding the measurement and analysis process must be introduced.

To conduct a measurement at the KATRIN experiment a **measurement time distribution (MTD)** must be chosen. It contains a set of retarding voltages applied by the main spectrometer paired with the amount of measurement time per voltage setpoint. Depending on the chosen measurement mode, additional dead-time between the measurement points is needed to reach a certain set-voltage precision. This is relevant for the KATRIN experiment since the high-voltage applied at the main spectrometer needs to be set with mV precision. Therefore, several seconds for each change of the voltage need to be budgeted for this process when planning the measurement. Since data-taking is not interrupted between measurement points, additional measurement time can be recovered later, if more dead-time was budgeted than needed. Nevertheless, an automatic optimised system for regaining measurement time is only in place for standard scans of the tritium β-spectrum. Due to the non-standardised use of krypton measurements and available krypton measurement settings, an automatic system cannot be used and thus the dead-time must be well assumed beforehand.

During the measurement, the spectrum is scanned according to the MTD alternating in upwards and downwards direction. These scans are called **up- and down-scans**, respectively. Each scan is recorded as a run denoted by an individual run-number. Each rate at one recorded measurement point is transferred into one sub-run of a run. Additionally, the so-called **run-summary** of each run contains a range of information from different sensors of the experiment. Besides the rate and measurement time it covers time-stamps, temperatures, additional voltage readings, tritium gas parameters, the respective RW voltage, BIXS count rates (see subsection 3.1.1) and many more. Those run-summary files are later used in the analysis.

The scans of the spectrum can be performed in different **measurement modes**. These modes differ in the way the retarding voltage is set during the measurement. For the standard setting the retarding voltage is set by the vessel high-voltage while the inner electrodes (IE) stay constant $-200\,\mathrm{V}$ more negative than the vessel voltage. This mode is well understood, which is why it is mainly used for the tritium β-scans. As already discussed, setting the high-voltage with the needed precision takes time. Therefore, other measurement modes have been developed which aspire to reduce the dead-time. One of them is called the IE mode. It is based on the concept that setting a smaller voltage with the same precision should take less time in comparison to the high-voltage. Thus, the vessel high-voltage is set fixed and the retarding voltage is set by the IE. This mode is able to reduce the dead-time but also comes with its own systematic effects, as further discussed in section 5.1. Extending the measurement idea of the IE mode by completely eliminating any dead-time, one arrives at the ramping mode. This mode uses the same setup for setting the retarding voltage as the IE mode, but it does not require a MTD. Instead the retarding voltage is continuously ramped up or down within the measurement interval. Since no separate measurement points are set, no dead-time can occur. The ramping mode can be used with different ramping velocities. For the analysis measurement points need to be defined. Therefore, the data is binned with $1\,\mathrm{s}$ intervals, giving one measurement point per second. This provides a great resolution of the measured spectrum, even though the duration of some calculations in the analysis scales with the number of measurement points. Additionally, this mode also comes with its own systematic effects, which need to be understood and accounted for in the analysis. They are further discussed in section 5.1.

When analysing the data, each run can be fitted separately or runs can be combined beforehand. The combination of the data sets of multiple runs before the analysis is called **stacking**. There are several stacking modes and configurations available for the analysis.
First, the stacking modes implemented in the KaFit environment are introduced. Those modes mainly differ in how they treat and combine different parameters. The stacked-run mode is characterised by summing over the count rates for all runs and calculating a measured time weighted average for the run parameter (RP) and so-called "slow control" (SC) operating parameter values[(1)]. More individual data points are used when applying the appended-run mode. Here, count rates and RP values are used individually from each subrun while only the SC values are averaged. The multi-run mode also uses the individual count rates and RP values from each subrun, but also takes run-wise SC values into account. Therefore, this mode provides the most detailed but also most time-extensive analysis. It has been shown for KNM1 data of the β-spectrum, that all three stacking modes deliver similar results [Cho19]. Additionally, a smart-stacking feature can be used. It bins the data points within a given energy interval and calculates one new measurement point per bin. This feature is needed when combining runs containing different amounts of subruns or when the number of measurement points shall be reduced to reduce the duration of the fit. This mainly concerns data from measurements conducted in ramping mode.
Moreover, several different stacking configurations have been tested during the analysis of this thesis. The standard configuration consists of always stacking paired runs of up- and down-scans together. Denoted as V_0, this configuration is used to account for systematic effects related to the time dependent decay of the krypton source. Details about this effect can be found in subsection 5.1.1. Two more configurations have been tested: always stacking three up- and three down-scans together (V_2) and either stacking six up- or six down-scans together (V_1). The stacking configurations V_1 and V_2 are mainly relevant for the measurements performed in ramp-scan mode since here the duration of one run is significantly shorter compared to the other measurement modes, which increases the amount of needed calculation resources drastically. Additionally, measurements performed in ramping mode show a special systematic effect which becomes visible when analysing up- and down-scans separately and which is shown in subsection 5.1.3.

In order to perform an analysis of the data one also has to choose a set of free parameters plus pull terms if needed. Thus, different **parameter sets** can be defined. First, a minimal set of parameters to describe the N line spectrum is chosen. It is de-

(1) SC values cover additional voltage readouts for the high-voltage and the RW voltage, readouts for different magnet currents and for sensors tracking the temperature and vacuum conditions. The RP are a list of parameters assigned to a run or subrun. They can concern identifiers of the run, e.g. run number and time stamps, LARA values (see subsection 3.1.1), BIXS count rates and pressure sensor readouts monitoring the source conditions.

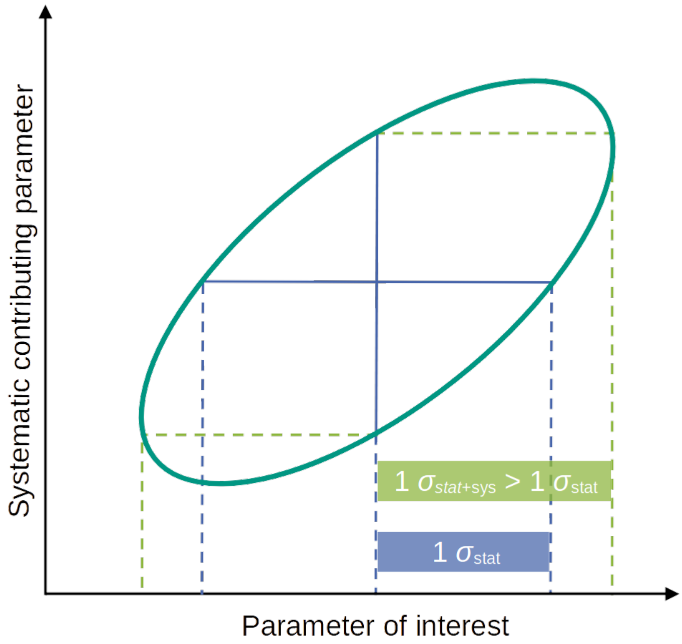

Figure 4.11: Resulting uncertainties from the elliptical log-likelihood profile. The uncertainty on the parameter of interest dependent on the systematic contributing parameter can be read off from the elliptical log-likelihood profile. The estimate of the parameter of interest is obtained by minimising the negative log-likelihood and lies in the center of the ellipse. The horizontal interval between the parameter estimate and the value of the ellipse at the same hight (blue) gives the statistical uncertainty of $1\,\sigma_{\mathrm{stat}}$. To include the systematic contribution by a parameter the horizontal interval between the value of the ellipse at the estimate of the parameter of interest and the second value of the ellipse for the same hight (green) must be considered, giving the combined uncertainty of $1\,\sigma_{\mathrm{stat+sys}}$.

noted as the statistical fit parameter set "stat", since the uncertainties on the resulting parameters are only of a statistical nature. This parameter set consists of the N_2 line intensity I_{N2}, the background rate c_{Bg}, the Gaussian broadening σ_{G}, as well as the N_2 line position E_{N2}. If the analysing interval also covers the energy loss region of the N_2 line, the energy loss shift Δ_{10} and the column density ρd are added to the parameter set. Those four to six parameters are always fitted as free parameters without any pull terms. For other parameter configurations, the "stat" set can be expanded. In order to study the influence of different parameters with different uncertainties on the fit result, all parameters listed in table 4.2 are added with pull terms separately to the "stat" configuration. Figure 4.11 visualises the influence of a systematic contributing parameter on the uncertainty of a parameter of interest. For the studies, the regarding parameter set is named after the added parameter. When adding extra lines, all parameters regarding this line are used as fit parameters. Thus, the N_1 parameter set includes the "stat" parameters, the relative line position, relative line intensity and natural line width of the N_1 line.

When performing **sensitivity studies** either additional fit parameters with pull terms or changes in the model can be introduced. Those studies are performed to determine and quantify the individual systematic contribution of each parameter. Comparing the resulting fit parameters, model dependent systematic effects are expected to cause a shift in the mean values of the plasma dependent fit parameters E_{N2}, σ and Δ_{10}. When adding parameters with their uncertainties using pull terms, this is expected to influence the uncertainty of the resulting fit parameters. In this case, the uncertainties of the plasma dependent fit parameters must be compared. Additionally, there are few effects, which require both a change in the model and an additional parameter, such as the background slope m_{Bg}. Here, a shift of the mean values and an influence on the uncertainty of the plasma parameters must be reviewed. The performed systematic studies are presented in section 5.2.

Chapter 5

Analysis of Systematic Effects in Krypton N Line Measurements

5.1 Description of Systematic Effects

In the following subsections different expected systematic effects, which could have an influence on the parameters of interest σ^2, E_{N2} and Δ_{10} are introduced. These systematic effects are quantified on measured data and further discussed in section 5.3.

5.1.1 Rate Time Dependence caused by the Decay of the Krypton Source

The used krypton source ^{83}Rb exhibits a half life time of 86.2 d. Due to its radioactive decay an exponential decrease of the source activity is expected. This leads to a dependence of the number of detected krypton conversion electrons $N(t)$ on the time t, described by

$$N(t) = N_0 \exp\left(-\frac{\ln 2}{86.2\,\mathrm{d}} t\right) + c_{\mathrm{Bg}}\,. \tag{5.1}$$

Here, $N_0 = N(t = 0)$ is used and a constant background rate c_{Bg} is added.
Since the rate is time-dependent it must have an effect on the measured spectrum. Also, the effect on the spectrum must depend on the scanning direction during the measurement. The deformation of the spectrum for both up- and down-scans is visualised in figure 5.1. With time the activity decreases and less electrons than expected without the effect are measured. For up-scans the curve shape decreases faster than expected which leads to a steeper slope. In case of the down scans the curve shape does not increase as much and as fast as expected otherwise and therefore shows a flatter slope. The slope corresponds to the broadening σ^2 of the line, as shown in figure 4.9, which is one of the parameters of interest.
To account for this systematic effect in the analysis stacking of up- and down-scans is used. This is expected to cover for the effect since the count rates of both scans are averaged, which should cancel out the slightly different slopes.

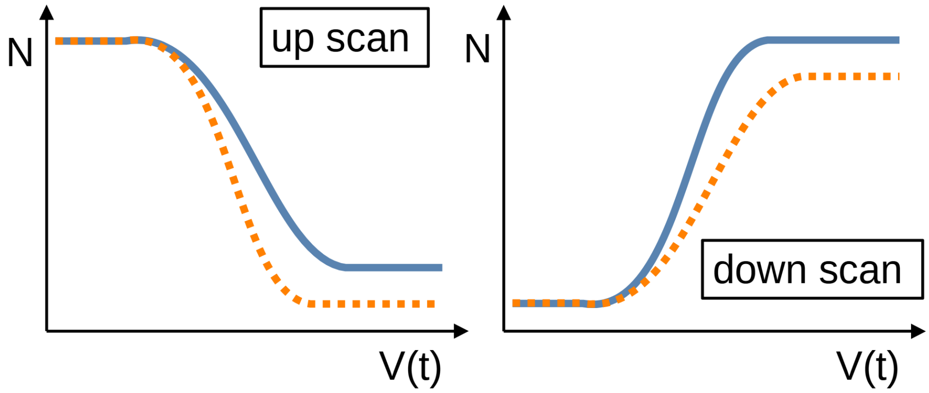

Figure 5.1: Effect of source decay on the spectrum, depending on the scan direction of the measurement. The blue solid line depicts the measured spectrum as expected without the effect, whereas the orange dotted line visualises the effect of the decreasing activity on the number of counted electrons N over time t. The spectrum is plotted over the retarding voltage $V(t)$ changing with t.

5.1.2 Binning Effect

When performing ramp scans the retarding potential does not get set for separate measurement points but gets continuously changed. To create measurement points for the analysis, the detected counts within one bin are assigned to the mean retarding voltage. A fixed binning width of 1 s is used. This means that when looking at one measurement point, this value corresponds not only to one well defined retarding potential, but to a range of retarding potentials within the bin. Furthermore, the range of retarding potential values per bin increases with increasing ramping velocity. It is therefore expected, that the binning could cause a distortion of the spectrum, which must be velocity dependent. Since an additional uncertainty on the retarding energy is introduced, the broadening σ^2 could be sensitive to this systematic effect on the spectrum.

5.1.3 Timing Variations of Ramp Scans

Another systematic effect expected to have an effect on the ramping measurements are timing variations. Since no discrete retarding potentials are set with precision at a certain time it is more challenging to assign the right retarding voltages to the right time stamps. Additionally, it is not known at which retarding potential the ramping scan started or stopped. This causes an additional uncertainty on the retarding energy and may even induce shifts of the measured ramping intervals. These effects might also exhibit a dependence on the ramping velocity.

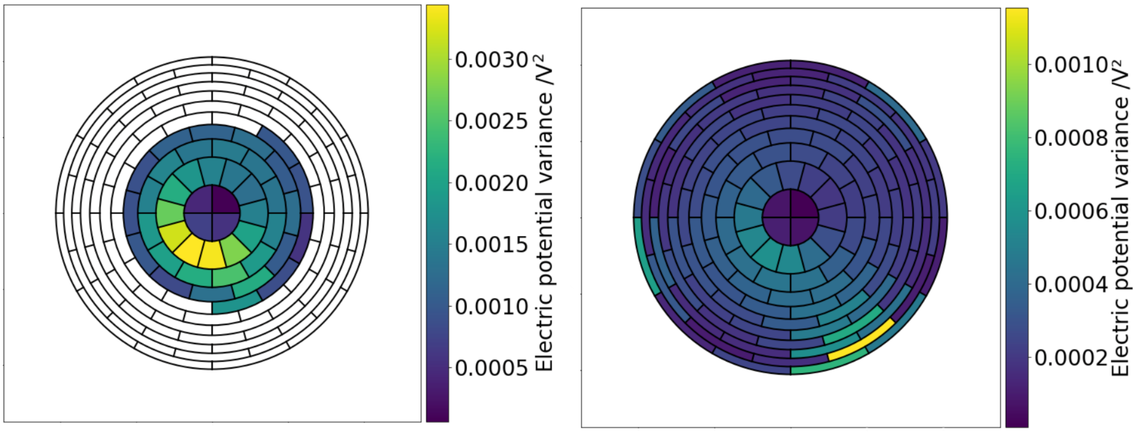

Figure 5.2: Electric potential variance per pixel for 1 G (left) and 2.7 G (right) setting without ring 11 and 12. The values result from simulations and are taken from the KNM3 period summaries listed in appendix A.3. Each electric potential variance value is pixelwise histogrammed onto its position at the FPD.

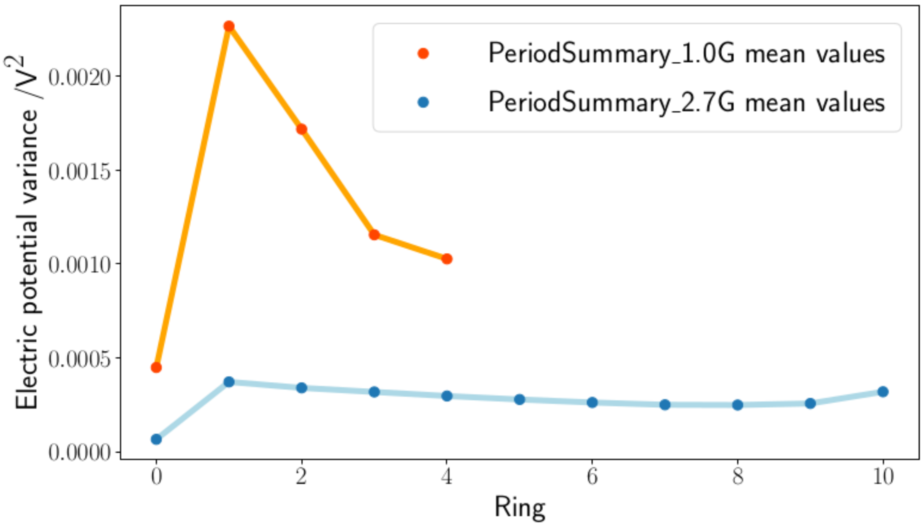

Figure 5.3: Electric potential variance per ring for 1 G (orange) and 2.7 G (blue) setting without ring 11 and 12. Shown are the values of the electric potential variance from figure 5.2 averaged over the rings.

5.1.4 Electric Potential Distribution within a Pixel

The electric potential in the analysing plane exhibits a radial and polar dependency. When mapping the electric potential onto the FPD one can assign each pixel a mean electric potential and a variance. Those two values are dependent on the magnetic field setting since it determines the size of the area through which the electrons are guided. E.g. due to the stronger fan out of the magnetic field lines in the analysing plane for the 1 G setting compared to the 2.7 G setting one detector pixel corresponds to a larger area in the analysing plane and therefore experiences a larger electric

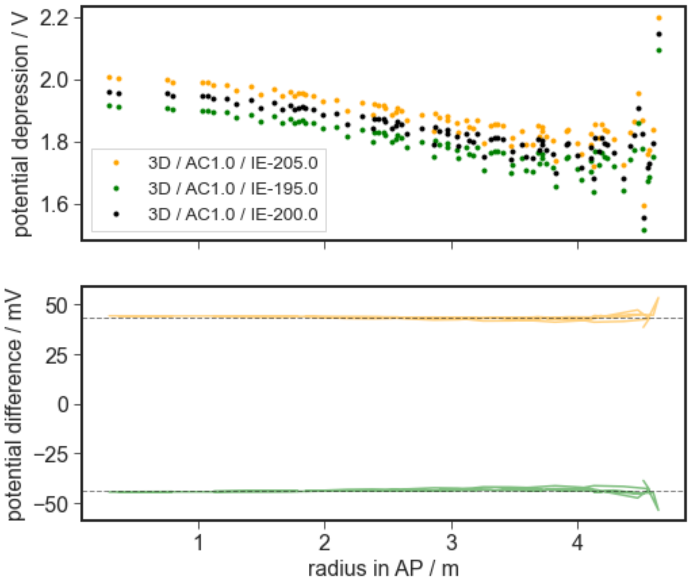

Figure 5.4: Simulation of the inner electrode voltage dependent potential depression. The upper plot shows the progression of the potential depression over the radius in the analysing plane for three different voltages of the inner electrode. The vessel voltage is constant. The setpoint of the IE at −200 V (black) corresponds to the standard offset between vessel and IE. At −205 V (yellow) the IE is set 5 V more negative and at −195 V (green) it is set 5 V more positive than usual. The lower plot shows the difference of the electric potential for IE setpoints at −205 V and −195 V in reference to the usual −200 V setpoint. The colors correspond to the same setpoints as for the upper plot. Simulated by J. Behrens with a 3D main spectrometer model.

potential variance. This is shown in comparison to the 2.7 G setting in figure 5.2. This comparison shows, that the electric potential variance for the 1 G setting varies between $6.2 \times 10^{-5}\,\mathrm{V}^2$ and $3.4 \times 10^{-3}\,\mathrm{V}^2$, whereas the same values for the 2.7 G setting lie between $9.7 \times 10^{-6}\,\mathrm{V}^2$ and $1.1 \times 10^{-3}\,\mathrm{V}^2$. It is visible, that the 1 G setting exhibits larger variances of the electric potential and larger differences of the variance between neighbouring pixels. Furthermore, figure 5.3 shows, that this effect is still relevant when averaging the electric potential variance per ring.
This observation must be accounted for in the analysis since the variance of the electric potential distribution within a pixel leads to an additional broadening σ'^2. This is especially relevant for the 1 G setting since it shows the largest variances and differences between the pixels. Thus, the variance of the electric potential within a pixel has been implemented in the analysis in form of an additional broadening which is added onto the broadening σ^2.

5.1.5 Inner Electrode Voltage dependent Potential Depression

To understand the inner electrode voltage dependent potential depression one first has to understand the “normal” potential depression. Therefore one needs to consider how

the retarding potential in the analysing plane is created.
There are two components of the experiment which create the retarding potential, the vessel and the inner electrode. The vessel is under high voltage, whereas the inner electrode inside the vessel is usually set to be 200 V more negative than the vessel voltage. The field strength of the superposition of both fields is radially dependent and decreases to the center. This is called the potential depression. In the standard measuring mode only the vessel voltage is changed, while the relative IE voltage is constant. Thus, the potential depression does not change.
For the measurements in IE and ramping mode the vessel voltage gets set to a constant value and the IE voltage is varied. In this case the progression of the potential depression over the radius is expected to stay the same while the overall profile shifts in its absolute values. This shift in reference to the standard setpoint of the IE is expressed by the potential difference. Thus, the potential difference changes for each setpoint of the IE, which leads to an inner electrode voltage dependent potential depression. The regarding simulation by J. Behrens is shown in figure 5.4. It predicts a shift of the potential depression per retarding voltage by $-8.8\,\mathrm{mV/V}$. For measurements in IE MTD or IE ramping mode this has the consequence that the shift due to the IE voltage dependent potential depression gets larger the more the IE voltage changes. Therefore, the vessel voltage should be chosen so that the standard IE setpoint of $-200\,\mathrm{V}$ lies in the middle of the measurement interval. Furthermore, since the effect is expected to scale linearly with the IE voltage the data can be corrected for this effect, when the exact vessel voltage is known. The results of further investigations of this systematic effect can be found in subsection 5.3.3.

5.2 Quantification of Systematic Effects in Sensitivity Studies

Studies on the effects of various parameters on the observables σ^2, E_{N2} and Δ_{10} have been conducted. For this purpose two Asimov Monte Carlo data sets are generated, differing in their amount of statistics. An Asimov Monte Carlo data set represents the mean result of many Monte Carlo experiments by setting all observed quantities to their expected values. The data sets are generated with 1 d and 14 d statistics. This enables to study the systematic effects dependent on their amount of statistics. The following settings have been used for the generation of the data:

- The asymmetric gas density profile
- No synchrotron radiation, relativistic effect, Doppler effect or detailed transmission has been used, since these settings are added later in the study.
- The KNM3 Eloss model[(1)]
- The 2.7 G magnetic field setting

(1) The KNM3 Eloss function has only be measured at 18 keV, but not at 32 keV. Therefore, the used Eloss model is expected to be slightly inaccurate for the N lines. Nevertheless, it is here assumed to be the Monte Carlo truth.

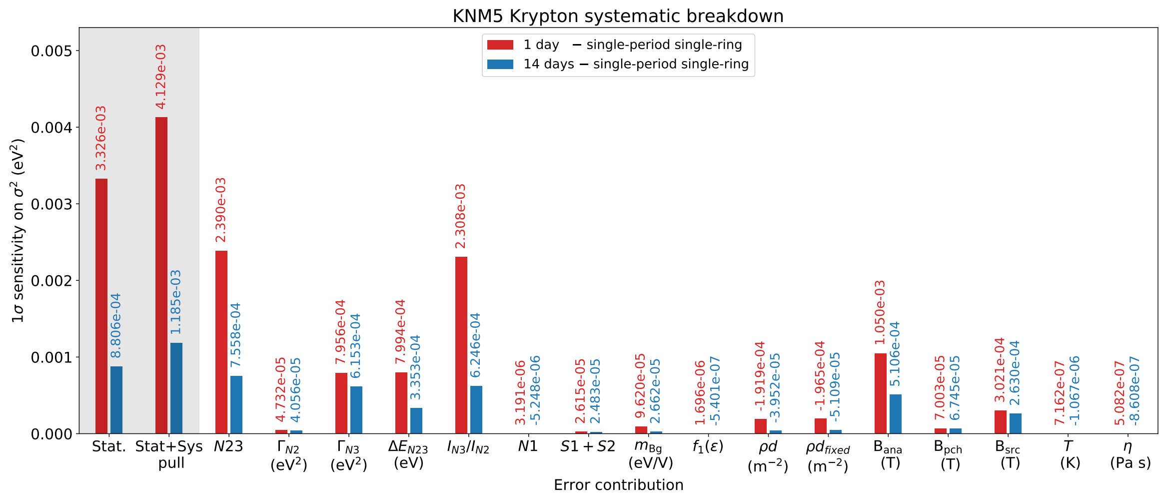

Figure 5.5: Sensitivity on σ^2 dependent on various parameters for 1 d and 14 d measurement time. The depiction is based on the routine introduced in subsection 5.2.1. The uncertainty on σ^2 is dominated by the statistical uncertainty. The significant systematic contributions result from Γ_{N3}, ΔE_{N23}, I_{N3}/I_{N2}, B_{ana} and B_{src}. The uncertainty contributions are reduced with longer measurement times t. The combined uncertainty "Stat+Sys" does decrease quadratically with t.

More details about the model configurations can be found in subsection 4.3.2. All other parameter values have been used in accordance to table 4.2. For the generation the GSL integration method has been used, which is further described at the end of subsection 5.2.2.
Furthermore, the spectrum has been generated using an optimised MTD including the Eloss region with the N_1 line and the N_{23} lines. The values of the optimised MTD can be found in the appendix section A.1.

The parameter dependent effects on the sensitivity on the observables σ^2, E_{N2} and Δ_{10} are discussed in subsection 5.2.1. Additionally, a comparison for reduced uncertainties on the N line parameters from a measurement using helium can be found there. Subsection 5.2.2 provides shift values of σ^2, E_{N2} and Δ_{10} caused by different models.

5.2.1 Parameter Dependent Systematic Studies

For the sensitivity studies the parameters and pull terms listed in table 4.2 have been used. When investigating the effect of a line, all regarding parameters are used. The same model as for the Asimov Monte Carlo data generation has been used. Thus, the Monte Carlo truth is given by the mean values of the parameters as listed in the table 4.2. The uncertainties for the studied parameters are given relative to the "Stat." uncertainty. The corresponding "Stat." fit was performed with the free parameters σ^2, E_{N2}, Δ_{10}, c_{Bg}, I_{N2} and ρd. The "Stat+Sys" fit includes the free parameters of the statistical fit and the systematic contributions of all additional parameters in form

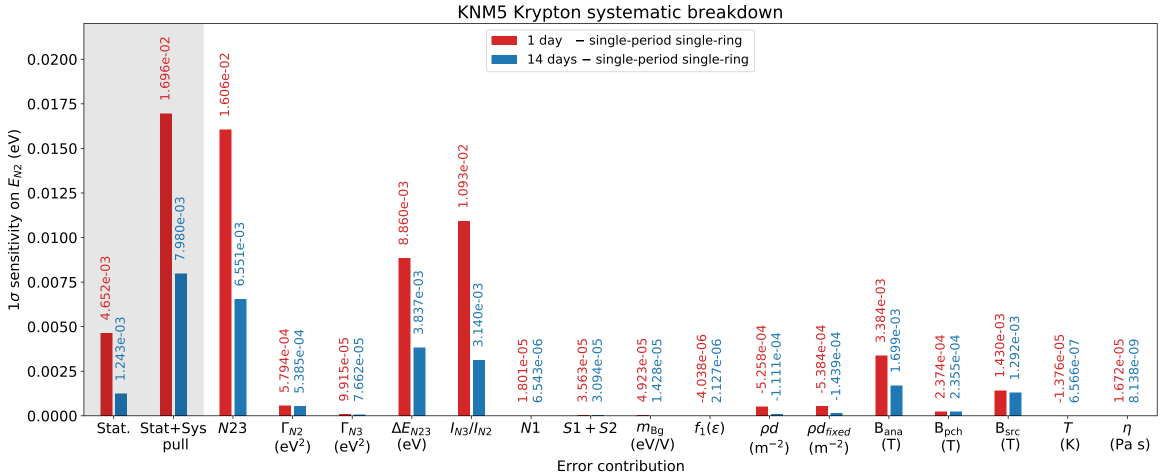

Figure 5.6: Sensitivity on E_{N2} dependent on various parameters for 1 d and 14 d measurement time. The depiction is based on the routine introduced in subsection 5.2.1. The uncertainty on E_{N2} is dominated by the systematic contributions of ΔE_{N23}, I_{N3}/I_{N2}, B_{ana} and B_{src}. The uncertainty contributions are reduced with longer measurement times t. The combined uncertainty "Stat+Sys" does not decrease quadratically with t.

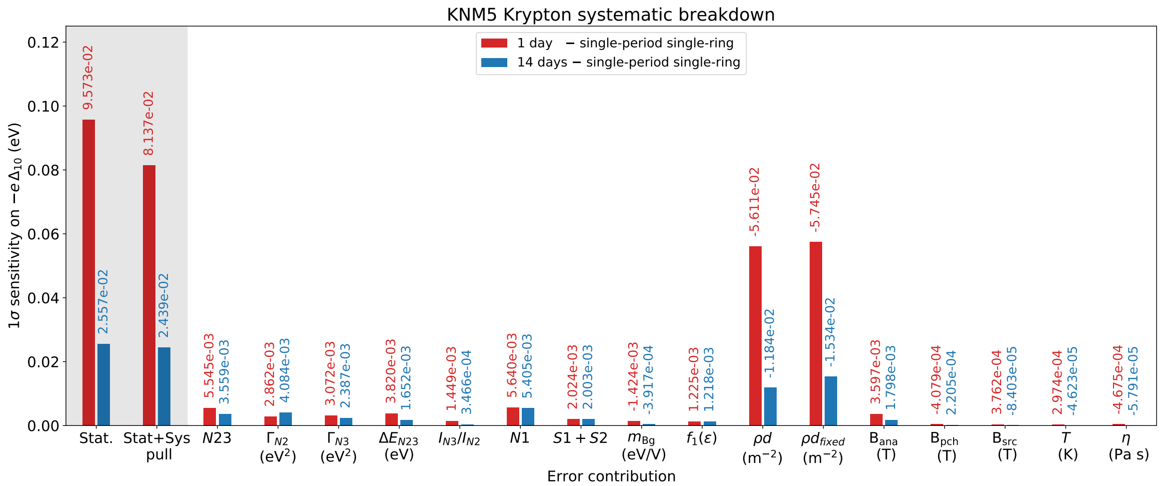

Figure 5.7: Sensitivity on Δ_{10} dependent on various parameters for 1 d and 14 d measurement time. The depiction is based on the routine introduced in subsection 5.2.1. The uncertainty on Δ_{10} is dominated by the statistical uncertainty. The largest systematic contribution result from ρd, which significantly decreases the combined uncertainty "Stat+Sys". The uncertainty contributions are reduced with longer measurement times t. The combined uncertainty does decrease quadratically with t.

of pull terms. The systematic uncertainties of the added parameters σ_{sys} are given relative to the "Stat." uncertainty σ_{stat} with

$$\sigma_{\mathrm{sys}} = \sqrt{\sigma_{\mathrm{tot}}^2 - \sigma_{\mathrm{stat}}^2}\,. \tag{5.2}$$

σ_{tot} is the total uncertainty resulting from the fit. The squared sum of all individual uncertainties does not necessarily equal the "Stat+Sys" uncertainty due to correlations between the parameters.

The sensitivities regarding the **broadening $\boldsymbol{\sigma^2}$** are presented in figure 5.5. In preparation of the high-sensitivity N line measurements in KNM5 (see section 5.5) a sensitivity on σ of 5 meV to 10 meV uniform for 14 d measurement time is aspired [FML+21]. Consequently, the ringwise uncertainty for σ^2 should be lower than $3.2 \times 10^{-4}\,\mathrm{eV}^2$, in the optimal case even lower than $8 \times 10^{-5}\,\mathrm{eV}^2$. The results of the sensitivity study are categorised compared to the aspired sensitivity goals. It is visible that the most relevant effects having an influence on the sensitivity are:

- The natural line width of the N_3 line Γ_{N3}
- The relative line position ΔE_{N23}
- The relative intensity I_{N3}/I_{N2}
- The magnetic field strength in the analysing plane B_{ana}

They contribute a systematic uncertainty at the order of a few $10^{-3}\,\mathrm{eV}^2$. The largest uncertainty contribution after 14 d of measurement time results from I_{N3}/I_{N2} with $0.6 \times 10^{-3}\,\mathrm{eV}^2$. Due to their significant systematic contribution, these listed parameters need to be included in the analysis in order to determine the correct uncertainty on σ^2. The following parameters only contribute slightly at the order of a few $10^{-4}\,\mathrm{eV}^2$ to the systematic uncertainty:

- The magnetic field strength in the source B_{src}
- The background slope m_{Bg} (relevant for short MTD IE measurements)
- The column density ρd
- The magnetic field strength of the pinch magnet B_{pch}

Their systematic effect is relevant compared to the optimal sensitivity goal of $8 \times 10^{-5}\,\mathrm{eV}^2$. The parameters which have no significant effect on the σ^2 uncertainty are:

- The N_2 line width Γ_{N2}
- The N_1 line
- The satellite lines S_1 and S_2
- The Eloss function $f_1(\epsilon)$
- The temperature T without the Doppler effect
- The viscosity η

Thus, for the determination of σ^2 they do not need to be included in the analysis as free parameters.

When considering the contribution of the column density ρd one can see, that it does not add to the systematic uncertainty, but that it reduces the uncertainty on σ^2 slightly compared to the statistical uncertainty by $1.92 \times 10^{-4}\,\mathrm{eV}^2$ for 1 d of statistics. It follows that the pull term of ρd measures ρd more accurate than the data. When fixing the value of ρd the uncertainty on σ^2 stays approximately equal. Therefore, the precision of the external measurement is sufficient to describe the parameter. The decrease of the uncertainty due to the pull term is reduced with more statistics since in this case the data is more sensitive to ρd. It follows from this study, that it is not needed to fit this parameter in the analysis. Nevertheless, when considering real measurement data a discrepancy between the fitted value and the separately measured value of ρd has been observed. It is suspected that this could be due to an inaccurate configuration of the model concerning the scattering probabilities and the cross section for the N lines. Thus, for real measurement data, the value of ρd is not necessarily better known than from the data itself and therefore, ρd needs to be fitted in the analysis.

Overall, when increasing the statistics from 1 d to 14 d, all uncertainties decrease. Since the combined uncertainty "Stat+Sys" decreases quadratically with the measurement time t, the sensitivity on σ^2 is statistically dominated. Though, this does not apply to each individual systematic contribution. If the corresponding uncertainty does not decrease quadratically with t it is dominated by the pull term contribution. In this case the pull term reduces the uncertainty compared to the uncertainty resulting from a completely free parameter without a pull term. With more statistics the data can become more sensitive to the parameter and the influence of the pull term decreases. From the parameters which contribute significantly to the systematic uncertainty, Γ_{N3}, ΔE_{N23} and B_{ana} do not show a quadratically decrease in uncertainty over time and are therefore dominated by their pull terms. This is best visible considering the contributed uncertainties of Γ_{N3}, which reduce from $0.8 \times 10^{-3}\,\text{eV}^2$ for 1 d statistics to only $0.6 \times 10^{-3}\,\text{eV}^2$ for 14 d statistics. The same can be observed for the slightly significant contributions of B_{src} and B_{pch}, which both show close to no reduction in uncertainty.
Consequently, since the combined uncertainty is statistically dominated, increasing the statistics is very effective to reduce the uncertainty on σ^2. In order to reduce the contribution of the pull term dominated parameters, external measurements are needed to improve the pull term uncertainty.

Considering the sensitivity on the **N_2 line position E_{N2}**, shown in figure 5.6, a sensitivity on the meV scale is desirable. The systematic contributions of the parameters are categorised oriented on this limit. Additionally it must be mentioned, that the absolute N_2 line position is not measurable for the KATRIN experiment due to the work functions in the source. But since the krypton line positions are used to detect radial systematic effects in the experiment, only the relative line position is of interest. The most relevant systematic contributions of several meV result from the parameters:

- The relative line position ΔE_{N23}
- The relative intensity I_{N3}/I_{N2}
- The magnetic field strength in the analysing plane B_{ana}
- The magnetic field strength in the source B_{src}

The systematic uncertainty of the N_{23} lines of 16.1 meV for 1 d statistics is mainly composed of ΔE_{N23} with 8.9 meV and I_{N3}/I_{N2} with 10.9 meV. It makes up for almost the total combined uncertainty on E_{N2} "Stat+Sys" of 17 meV and is therefore the largest contributor. The listed parameters should be included in the analysis to obtain an unbiased estimate of E_{N2}. The parameters contributing at the order of a more optimistic limit of 0.3 meV on the sensitivity of E_{N2} are:

- The natural line width of the N_2 line Γ_{N2}
- The column density ρd
- The magnetic field strength of the pinch magnet B_{pch}

As for the sensitivity on σ^2, the column density slightly reduces the systematic uncertainty. Negligible contributions to the systematic uncertainty compared to the aspired sensitivity limits come from the parameters:

- The natural line width of the N_3 line Γ_{N3}
- The N_1 line
- The satellite lines S_1 and S_2
- The background slope m_{Bg}
- The Eloss function $f_1(\epsilon)$
- The temperature T without the Doppler effect
- The viscosity η

The sensitivity on E_{N2} is dominated by systematics since the combined uncertainty "Stat+Sys" does not decrease quadratically with the measurement time t. Also, the statistical uncertainty for 1 d measurement time is small with 4.7 meV compared to the combined uncertainty with 17.0 meV. When considering the individual systematic contributions of the relevant parameters, most of them show an uncertainty which does not decrease quadratically with t due to a dominating pull term. This can be seen for ΔE_{N23}, B_{ana} and B_{src}, but also for the slightly relevant parameters Γ_{N2} and B_{pch}. The latter three show close to no reduction of the corresponding uncertainty with time.
Overall, the significantly contributing parameters need to be included in the analysis. Since the sensitivity on E_{N2} is dominated by systematics, lowering the pull term uncertainty on the significantly contributing parameters by an external measurement would be profitable for the sensitivity. This would even improve the sensitivity for a low statistics measurement. Higher statistics can further reduce the uncertainties.

For the sensitivity on the **Eloss shift $\boldsymbol{\Delta_{10}}$**, shown in figure 5.7, it is aimed at 15 mV for the uniform sensitivity [FML+21]. The ringwise sensitivity then amounts to 48 mV. The only systematic contribution exceeding this limit for a 1 d measurement time results from the column density ρd. Nevertheless, as already discussed for the sensitivity on σ^2, the contribution of ρd reduces the uncertainty on Δ_{10} with -56.1 mV for a 1 d measurement. Since all other systematic uncertainties are comparably small this leads to a combined uncertainty "Stat+Sys" of 81.4 mV being smaller than the statistical uncertainty on Δ_{10} of 95.7 mV. For a longer measurement time of 14 d they become approximately equal with $\sim$ 25 mV. As already discussed, this influence of ρd can not be transferred onto real measurement data due to unsolved discrepancies of the external measurement and the estimate of the fit.

Since all other contributions are small, they are categorised by their systematic contribution after 14 d measurement time being above or below 1 mV. The parameters contributing at the order of a few mV are:

- The natural line width of the N_2 line Γ_{N2}
- The natural line width of the N_3 line Γ_{N3}
- The relative line position ΔE_{N23}
- The N_1 line
- The satellite lines S_1 and S_2
- The Eloss function $f_1(\epsilon)$
- The magnetic field strength in the analysing plane B_{ana}

It is visible that the contribution of Γ_{N2} increases with more measurement time. This is presumably due to statistical fluctuations, since the statistical component of the uncertainty is much larger than the systematic contribution of Γ_{N2}. Furthermore, it can be seen that the uncertainty contributions of the N_1 line, the satellite lines S_1 and S_2 and the Eloss function $f_1(\epsilon)$ do not scale with the measurement time. These contributions can therefore only be reduced by an external measurement and thereby improved pull terms, as shown in the next part. The parameters having negligible influence on the sensitivity on Δ_{10} are:

- The relative intensity I_{N3}/I_{N2}
- The background slope m_{Bg}
- The magnetic field strength of the pinch magnet B_{pch}
- The magnetic field strength in the source B_{src}
- The temperature T without the Doppler effect
- The viscosity η

Overall, high statistics are important for a good sensitivity on Δ_{10}, as well as a good agreement between the values of the column density from the fit and from external measurements.

Impact of Reduced Uncertainties by a Measurement with Helium

A krypton measurement with helium as carrier gas can be used to decrease the uncertainties on the line parameters compared to the literature values shown in table 4.2. For the measurement, helium is used instead of tritium to avoid scatterings in the region of the N lines, which allows to measure the N_1 and satellite lines S_1 and S_2. It is necessary to replace the tritium with another carries gas for krypton to ensure a high krypton rate. Using helium has the advantage that electrons scattering on the helium atoms exhibit a minimal energy loss of 20 eV and are therefore not visible in the measurement interval of the N lines. With tritium in the source the N_1 and satellite lines are superimposed by the energy loss peak of the single scattered electrons because of a minimal energy loss of only 13 eV. In preparation of the high-sensitivity N line measurements in KNM5 also a 1 d helium measurement is planned [FML+21]. It will be performed in the so-called WGTS Loop only mode, which circulates the gas mixture through the source without being able to filter out the accumulating impurities.

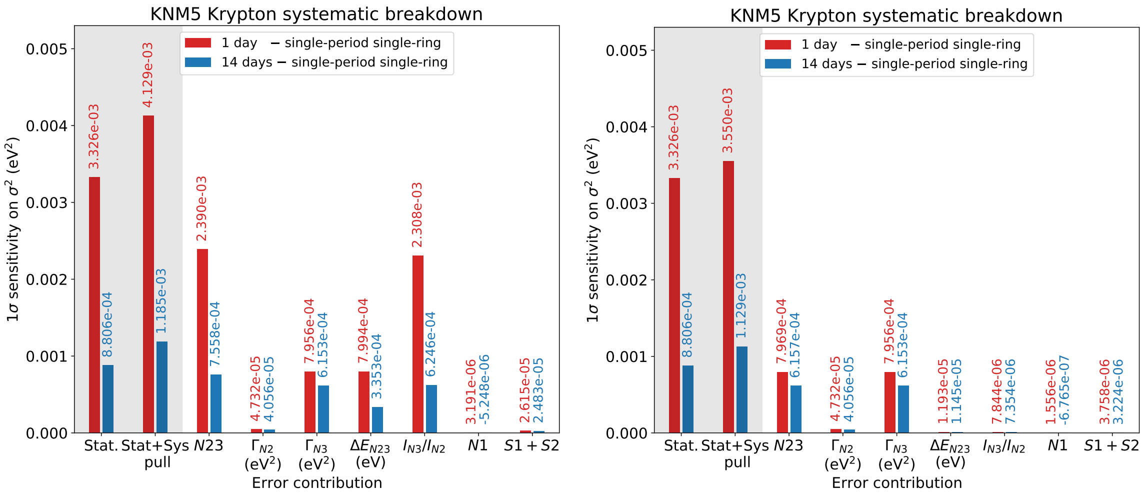

a Literature values

b Values after helium measurement

Figure 5.8: Sensitivity on σ^2 after N line measurements with helium dependent on various parameters (b) for 1 d and 14 d measurement time. In subfigure (a) the sensitivities without the extra measurement from figure 5.5 are shown in comparison. The measurement with helium is expected to reduce the systematic uncertainties on the N line properties since it allows to measure the N lines without scattering effects. The depiction is based on the routine introduced in subsection 5.2.1. The "Stat+Sys" uncertainty includes the systematic contributions of all additional parameters listed in table 4.2. The helium measurement reduces the systematic contributions of the N line parameters significantly, except for Γ_{N3}. Overall, the uncertainty on σ^2 is dominated by statistics.

Furthermore, a column density for this setting of roughly $2.7 \times 10^{20}\,\mathrm{m}^{-2}$ (0.1 %)[(2)] is used. The improved uncertainties have been estimated in a study by M. Böttcher. The values are presented in table 4.2. The expected impact of this helium measurement has been studied in the following systematic studies.

Figure 5.8 shows a comparison of the sensitivity on the **broadening $\boldsymbol{\sigma^2}$** with and without the reduced systematic uncertainties by the helium measurement. For a better overview only the uncertainties added by the line parameters are shown, since the helium measurement does not influence the uncertainties of the other parameters. The combined uncertainty "Stat+Sys" still includes the systematic uncertainty contributions of all parameters. The comparison shows, that a significant reduction of the uncertainty contribution of ΔE_{N23} and I_{N3}/I_{N2} by two orders of magnitude can be achieved. The only significant contributor left of the $N23$ lines is Γ_{N3} with $7.96 \times 10^{-4}\,\mathrm{eV}^2$. This is expected since the assumed uncertainty on Γ_{N3} after the measurement with helium does not decrease compared to the former assumption on this value. The natural line width Γ_{N3} is more difficult to obtain from a measurement than the other line properties since it is strongly correlated with the broadening

(2) Value from a quick preliminary analysis of the helium measurement data by A. Marsteller.

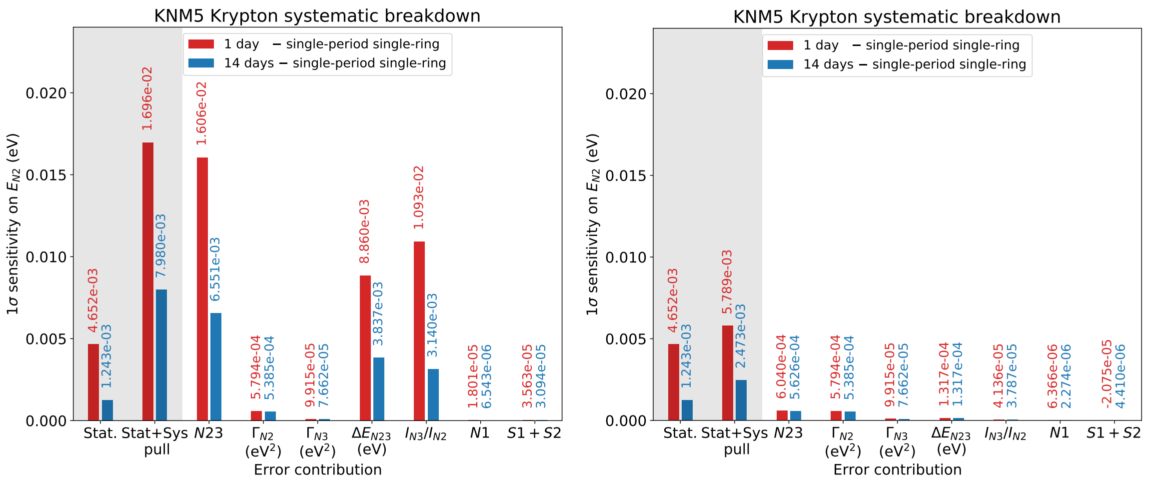

a Literature values **b** Values after helium measurement

Figure 5.9: Sensitivity on E_{N2} after N line measurements with helium dependent on various parameters (b) for 1 d and 14 d measurement time. In subfigure (a) the sensitivities without the extra measurement from figure 5.6 are shown in comparison. The measurement with helium is expected to reduce the systematic uncertainties on the N line properties since it allows to measure the N lines without scattering effects. The depiction is based on the routine introduced in subsection 5.2.1. The “Stat+Sys” uncertainty includes the systematic contributions of all additional parameters listed in table 4.2. The helium measurement reduces the systematic contributions of the N line parameters significantly, which causes the uncertainty on E_{N2} being dominated by statistics.

σ^2. On the other hand, the values for Γ_{N3} from literature only give an upper limit of 30 meV [VSD+18]. Therefore, assumptions must be made for the value and uncertainty on Γ_{N3} based on the available data. Additionally, there is no formation of a plasma in the source during the helium measurements [Mac21a]. This leads to a significant increase of the additional broadening, making it even more unlikely to obtain the natural line width in this measurement setting.
Overall, the systematic impact on the uncertainty of σ^2 is reduced. The combined uncertainty “Stat+Sys” decreases from $1.2 \times 10^{-3}\,\mathrm{eV}^2$ to $1.1 \times 10^{-3}\,\mathrm{eV}^2$ for 14 d statistics. The only significant systematic contribution after the helium measurement comes from Γ_{N3} with $0.6 \times 10^{-3}\,\mathrm{eV}^2$. All other contributions are negligibly small compared to the aspired sensitivity limit on σ^2 of $8 \times 10^{-5}\,\mathrm{eV}^2$. Thus, the regarding parameters can be fixed in the analysis. Understanding Γ_{N3} would eliminate all systematic contributions. But otherwise the helium measurement results only in a small decrease of the combined uncertainty and in a simplified analysis.

A significant reduction of the uncertainties after the helium measurement can be observed for the **N_2 line position E_{N2}** in figure 5.9. Since the uncertainty on this parameter is dominated by systematic uncertainties, the reduction of those systematics has a great impact on the combined uncertainty “Stat+Sys”. It is lowered from

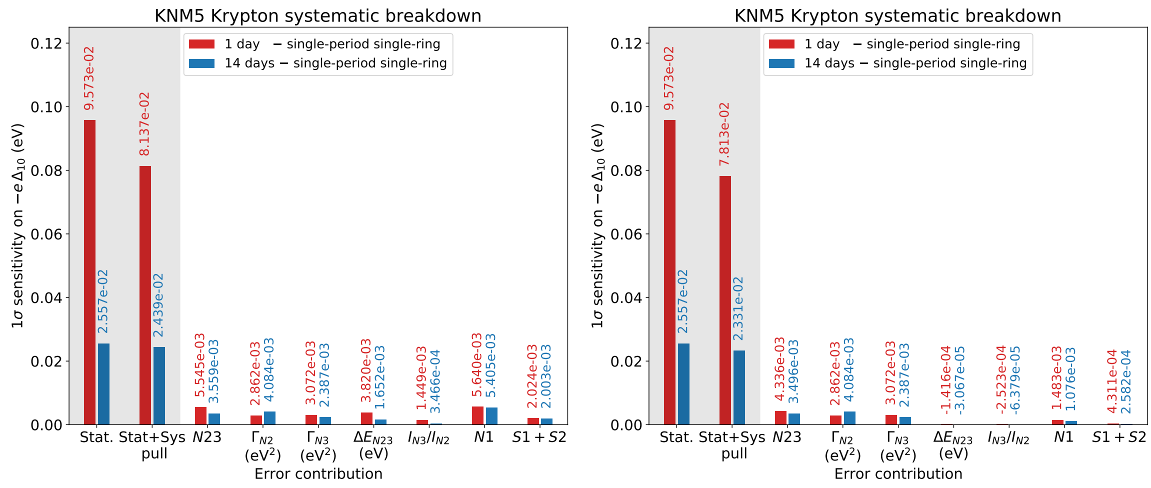

a Literature values　　**b** Values after helium measurement

Figure 5.10: Sensitivity on Δ_{10} after N line measurements with helium dependent on various parameters (b) for 1 d and 14 d measurement time. In subfigure (a) the sensitivities without the extra measurement from figure 5.7 are shown in comparison. The measurement with helium is expected to reduce the systematic uncertainties on the N line properties since it allows to measure the N lines without scattering effects. The depiction is based on the routine introduced in subsection 5.2.1. The "Stat+Sys" uncertainty includes the systematic contributions of all additional parameters listed in table 4.2. The helium measurement reduces the already small systematic contributions of the N line parameters further. Overall, the uncertainty on Δ_{10} is dominated by statistics.

8 meV to 3 meV for 14 d of measurement time. The statistical component of the total uncertainty is 1 meV. For this result the largest contributors of systematic uncertainties, ΔE_{N23} and I_{N3}/I_{N2}, are both reduced to the order of 0.1 meV and lower. The largest remaining uncertainty concerns the natural line width Γ_{N2} with only 0.5 meV after 14 d measurement time. Therefore, the systematic uncertainty on E_{N2} is lowered by the helium measurement by such an amount, that all systematic contributions from the parameters of the krypton N lines are negligible compared to the aspired sensitivity goal of 1 meV.

The uncertainty on the **Eloss shift Δ_{10}** is dominated by statistics, whereas the systematic uncertainties are comparably small. Furthermore, the combined uncertainty "Stat+Sys" is smaller than the statistical contribution, because it is reduced by the uncertainty contribution of ρd. This is visible in figure 5.7 showing all contributing parameters of the study. Figure 5.10 shows the comparison of the uncertainties on Δ_{10} with and without the reduced systematic uncertainties by the helium measurement. It is visible, that the combined uncertainty can be further reduced by the helium measurement from 24.4 mV to 23.3 mV for 14 d statistics, since it decreases the contributions of the N_1 line, the satellite lines S_1 and S_2, the relative line position ΔE_{N23} and the relative intensity I_{N3}/I_{N2} slightly. The significance of the helium measurement for the

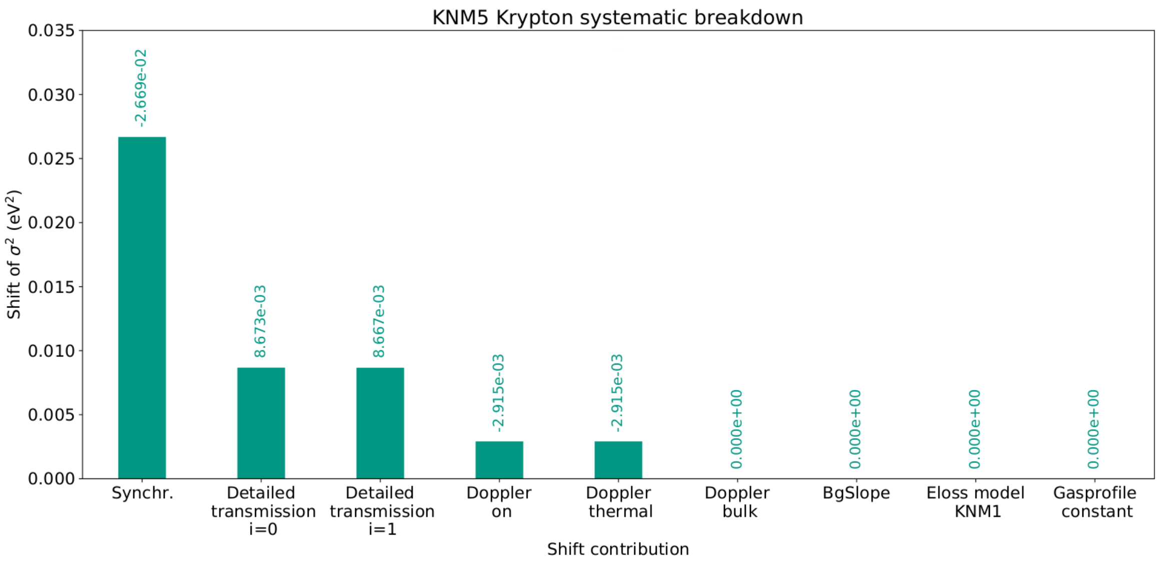

Figure 5.11: Shift of σ^2 dependent on various added model settings for 1 d and 14 d measurement time. The shift is in comparison to the mean value of $4 \times 10^{-3}\,\mathrm{eV}^2$. The depiction is based on the routine introduced in subsection 5.2.2. i denotes the number of scatterings taken into account by the detailed transmission. The main shift contributors on the value of σ^2 are the synchrotron radiation, the detailed transmission for unscattered electrons (i=0) and the Doppler effect.

sensitivity on Δ_{10} becomes visible when considering the uniform uncertainties after 14 d of measurement time. Then the unreduced uncertainty contribution of the N_1 line amounts to 1.7 mV, which is of the same order as statistical uncertainty with 7.9 mV. After the helium measurement the contribution of the N_1 line is only 0.3 mV. Consequently, the helium measurement improves the uncertainties on the uniform level.

In conclusion, the helium measurements will significantly improve the sensitivity on σ^2 if the natural line width of the N_3 line can be understood. The sensitivity on E_{N2} profits directly from the reduced uncertainties of the helium measurement, while the sensitivity on Δ_{10} is significantly improved when considering the uniform values. Furthermore, the helium measurement allows to determine the intrinsic line parameters, excluding the natural line width, with unreached sensitivity [VSD+18].

5.2.2 Model Dependent Systematic Studies

The influence of different model settings on the mean value of the observables σ^2, E_{N2} and Δ_{10} has been studied. In the following systematic studies variations of the model settings are associated with a shift relative to the mean value of the parameter. Thus, the values for the different model settings are given relative to the mean value of the observable, e.g. for the line position E_{N2}

$$E_{N2}(\text{shift}) = E_{N2}(\text{synchr.}) - E_{N2}(\text{mean})\,. \tag{5.3}$$

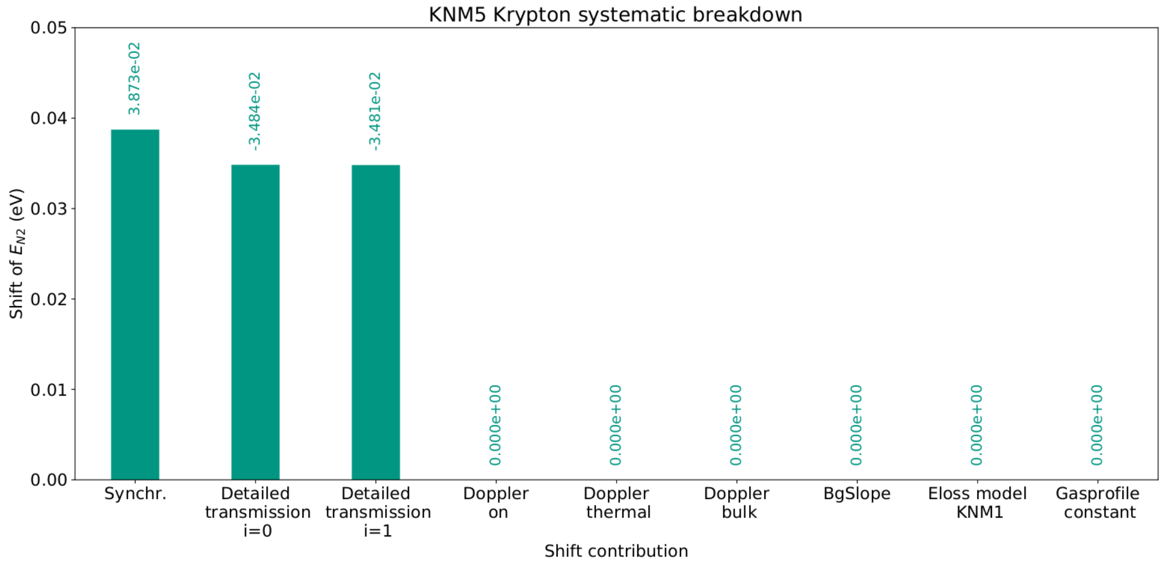

Figure 5.12: Shift of E_{N2} dependent on various model settings for 1 d and 14 d measurement time. The shift is in comparison to the mean value of 32 136.72 eV. The depiction is based on the routine introduced in subsection 5.2.2. i denotes the number of scatterings taken into account by the detailed transmission. The main shift contributors on the value of E_{N2} are the synchrotron radiation and the detailed transmission for unscattered electrons (i=0).

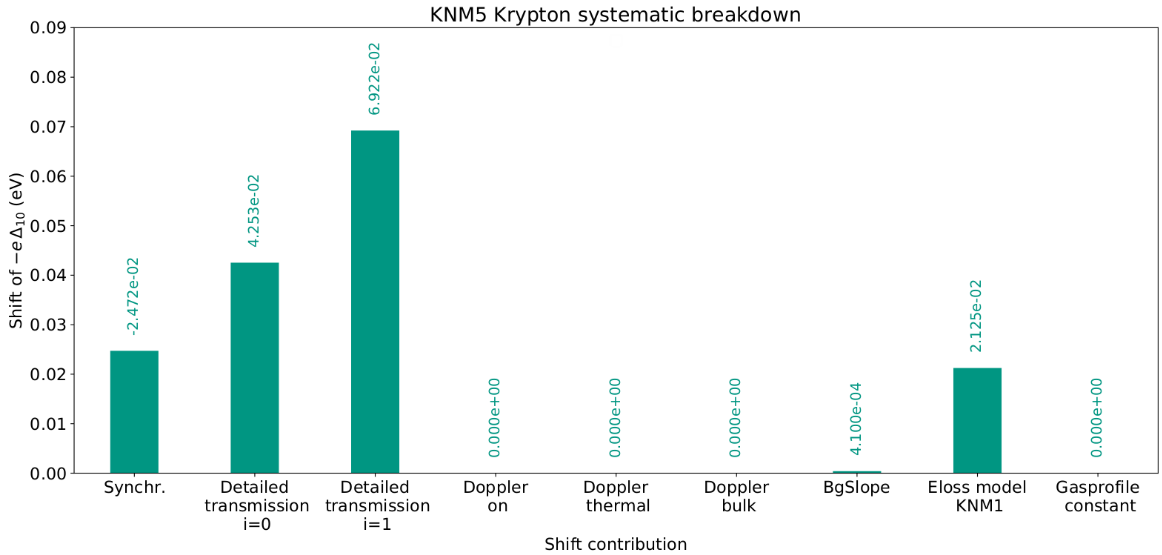

Figure 5.13: Shift of Δ_{10} dependent on various model settings for 1 d and 14 d measurement time. The shift is in comparison to the mean value of 0 eV. The depiction is based on the routine introduced in subsection 5.2.2. i denotes the number of scatterings taken into account by the detailed transmission. The main shift contributors on the value of Δ_{10} are the synchrotron radiation, the detailed transmission for single scattered electrons (i=1) and the Eloss model.

E_{N2}(shift) denotes the shift of the line position resulting from the linear difference between the line position with included synchrotron radiation in the model E_{N2}(synchr.) and the line position of the standard fit E_{N2}(mean). The corresponding standard fit was performed with the free parameters σ^2, E_{N2}, Δ_{10}, c_{Bg}, I_{N2} and ρd. The shift value can have a positive or negative sign. A negative sign implies that when adding this parameter to the model the mean value of the observable decreases. A positive sign stands for a shift of the mean value in positive direction when adding this parameter. The different model settings are introduced in subsection 4.3.2. Model settings causing a significant shift must be considered in the analysis of measured data.

First, the effect of the model on the **broadening $\boldsymbol{\sigma^2}$**, shown in figure 5.11 is considered. The contributed shift of the model setting does not depend on the amount of statistics. This observation can be transferred onto all other model dependent systematic studies. The largest influence on the mean value of σ^2 is contributed by the synchrotron radiation and the detailed transmission function. Taking the synchrotron radiation into account in the model causes a shift of the mean value of $26.7 \times 10^{-3}\,\mathrm{eV}^2$ in negative direction. The adding of the detailed transmission to the model causes a shift towards more positive values by $8.7 \times 10^{-3}\,\mathrm{eV}^2$. In this case, higher orders of scatterings i included in the detailed transmission do not effect the shift on σ^2. This is expected, since the N_{23} lines are not superimposed by a scattering peak. The Doppler effect also leads to a significant contribution, shifting the mean value towards smaller values by $2.9 \times 10^{-3}\,\mathrm{eV}^2$. The Doppler mode "on" combines the two Doppler modes "thermal" and "bulk". It is visible that only the "thermal" component contributes significantly with $2.9 \times 10^{-3}\,\mathrm{eV}^2$, while the effect of the "bulk" mode remains negligible. The shift of the "bulk" mode is at the same order as the numerical instabilities at around $10^{-6}\,\mathrm{eV}^2$ and is therefore set to $0\,\mathrm{eV}^2$. This proceeding applies to all following studies. The background slope, the usage of the KNM1 compared to the KNM3 Eloss model and the gasprofile does not shift the mean value significantly and can therefore be neglected.

The largest shifts of the **$\boldsymbol{N_2}$ line position $\boldsymbol{E_{N2}}$** are caused by adding the synchrotron radiation and detailed transmission to the model. This can be seen in figure 5.12. The added synchrotron radiation causes a shift of the mean value towards larger values of 38.7 meV, whereas the detailed transmission contributes a shift of 34.8 meV in the opposite direction. For E_{N2} the shift value of the detailed transmission does not depend on higher orders of scatterings i considered in the model. All other model settings cause a shift at the order of numerical instabilities and can therefore be neglected.

The mean value of the **Eloss shift $\boldsymbol{\Delta_{10}}$** is shifted in the opposite direction by the model compared to the values shown in figure 5.13 due to the fit observable being $-e\Delta_{10}$. Here, the shift regarding Δ_{10} are given. As observed for the other observables, the synchrotron radiation contributes a significant shift of 24.7 mV relative to the mean value of Δ_{10}. An even larger shift in negative direction is caused by adding the detailed transmission to the model. When only considering the unscattered electrons (i=0) the shift amounts to $-42.5\,\mathrm{mV}$. The shift increases to $-69.2\,\mathrm{mV}$ when additionally taking the single scattered electrons (i=1) into account for the detailed transmission. This contribution is by far the largest and therefore the most important one for the mean value of Δ_{10}. Another significant shift can be obtained when using the outdated KNM1 Eloss model instead of the more recent KNM3 Eloss model. It amounts to $-21.3\,\mathrm{mV}$. This result agrees with the observations from KNM1. It was found that the KNM1 Eloss function was shifted by around $20\,\mathrm{meV}$ due to a wrong binning [HLL+20]. Knowing that the used KNM3 Eloss function only applies for the $18\,\mathrm{keV}$ energy region it can be presumed that it might cause a shift at the same order of magnitude as the KNM1 Eloss function. This shows that finding and implementing the correct Eloss model for the $32\,\mathrm{keV}$ region is necessary to obtain the true value of Δ_{10} from krypton N line measurements. All other model settings give a shift below $1\,\mathrm{mV}$ and can therefore be neglected.

Overall, the synchrotron radiation, detailed transmission and Doppler effect cause significant shifts on the mean values of the observables and must therefore be used in the analysis of measured data to obtain the correct values. When the measurement interval includes the Eloss region, the detailed transmission for single scattered electrons and the most precise Eloss model for electrons with energies in the range of $32\,\mathrm{keV}$ should be used. All other contributions were found to be negligible. In future studies the influence of the energy dependence of the inelastic cross section should be additionally investigated.

Influence of the KNM1 Eloss Model Dependent on the Analysing Interval

An inaccurate Eloss function can cause a shift which is dependent on the analysing interval. This is presumed, since a rear wall voltage dependency of Δ_{10} in the KNM2 krypton measurements was obtained for the inner rings [Mac21a]. In the corresponding analysis pseudoring 0 shows a slope of $20.7\,\mathrm{mV/V}$ for Δ_{10} dependent on U_{RW}. This slope decreases towards the outer rings. Since the coupling to the rear wall is radially dependent this could be due to a physical or systematic effect. A systematic effect could result from the fact that the line position is dependent on the rear wall voltage. Since a fixed MTD is used for the measurement a line shift changes the measurement interval of the Eloss region. To simulate the order of magnitude of the systematic effect Asimov data with an extended Eloss region are simulated. The used retarding voltages can be found in appendix section A.1. The analysis uses the KNM1 Eloss model as a known inaccurate Eloss model and a varying analysing interval. The result for the Eloss shift Δ_{10} is shown in figure 5.14. The lower energy limit of the total analysing interval x is varied. $x = 21\,\mathrm{eV}$ corresponds to the analysing interval of the other sensitivity studies. It is visible that the contributed negative shift of the KNM1 Eloss model increases with a decreasing analysing interval by $1.04\,\mathrm{mV/V}$. In comparison to the slope obtained for the KNM2 measurement the estimation of the systematic influence cannot fully explain the behaviour of $\Delta_{10}(U_{\mathrm{RW}})$. Therefore, a physical cause is probable if the differences of the true Eloss model for $32\,\mathrm{keV}$ electrons to the used KNM3 model

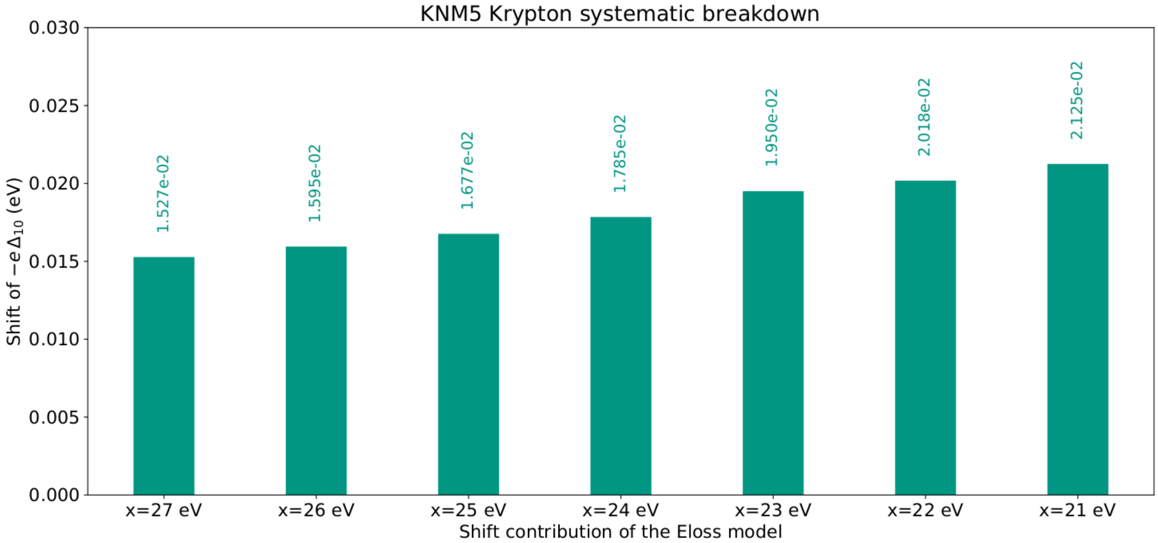

Figure 5.14: Shift of Δ_{10} with the KNM1 Eloss model dependent on the analysing interval for 1 d and 14 d measurement time. The shift is in comparison to the mean value of 0 eV. The lower energy limit of the total analysing interval x is varied. The depiction is based on the routine introduced in subsection 5.2.2. The shifts on Δ_{10} increase with a decreasing analysing interval by 1.04 mV/V.

are not significantly larger than the 20 meV difference between the KNM1 and KNM3 Eloss model [HLL+20].
For completeness, the dependency on the analysing interval has also been studied for σ^2 and E_{N2}. As expected, no influence could be found. The results are presented in section B.1 in figures B.1 and B.2.

Influence of the Source Slicing

In this study the influence of the source slicing regarding the longitudinal components of the model is determined. Since no longitudinal dependent source potential has been used only the detailed transmission can be studied to have an effect dependent on the slicing of the source. Therefore, adding a longitudinal dependent source potential might change the obtained results. Thus, the study is used to check the correct implementation of the detailed transmission in KASPER.
For the calculation of the response function the volume of the WGTS is sliced into voxels. The source is longitudinally segmented into N_{ini} initial slices to select N_{ini} values of the longitudinal distribution of the source parameters, e.g. the source potential, the density, the magnetic field and temperature. The number of slices N then gives the number of calculated source spectra. The calculation is based on the average of the selected source values from the initial slicing corresponding to each slice N. Thus, the usage of more N slices enables a more detailed treatment of the source parameters. It allows to take longitudinal dependent models and parameters into account, like the gas density profile, the magnetic field and therefore the maximum acceptance angle and

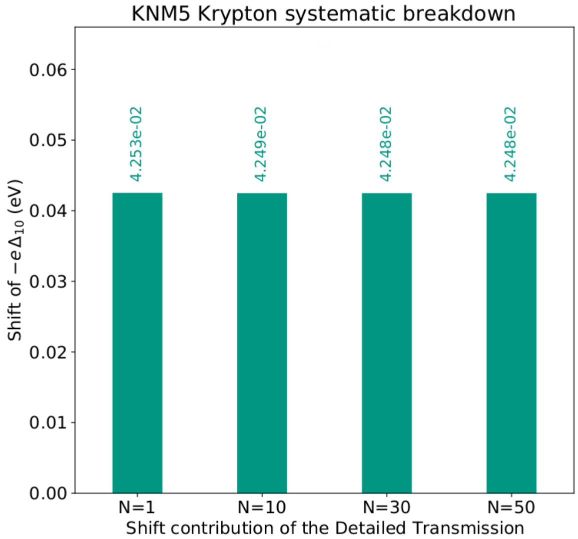

Figure 5.15: Shift of Δ_{10} with the Detailed Transmission model dependent on the number of slices of the source N for 1 d and 14 d measurement time. The shift is in comparison to the mean value of 0 eV. Here, the detailed transmission for unscattered electrons (i=0) has been used. The depiction is based on the routine introduced in subsection 5.2.2. The shifts on Δ_{10} are independent on the number of slices N.

the temperature. In the used model only the gas density profile and the temperature was used as a longitudinal dependent model setting.
From analytical calculations it is expected that for a homogeneous source potential the averaged scattering probabilities contributing to the response function are independent on the gas density distribution for a constant magnetic field [Gro15]. If these assumptions hold additional calculations of N slices should not be necessary. Therefore, it is expected that the influence of the detailed transmission on the observables should not change when increasing the number of slices N if a sufficient number of initial slices N_{ini} is used. For an inhomogeneous source potential the longitudinal profile of the scattering probabilities must be used for the calculation of the spectra, which might produce a dependence on N.
For the study the by [Gro15] recommended amount of $N_{ini} = 100$ slices is used. As shown in figure 5.15 for the influence on Δ_{10} no dependency of the detailed transmission for unscattered electrons (i=0) on the number of slices N could be found. The same result was obtained for the observables σ^2 and E_{N2}, which can be found in appendix section B.1 shown in figures B.3 and B.4.
Therefore, for the studied model a slicing of N=1 is sufficient.

Comparison of Integration Methods

The KASPER framework uses the Romberg method for the numerical integration [Kle14]. Furthermore, a new integration method, the QAGS GSL method, has been implemented into KaFit [GSL]. The integration of the line spectrum is an improper

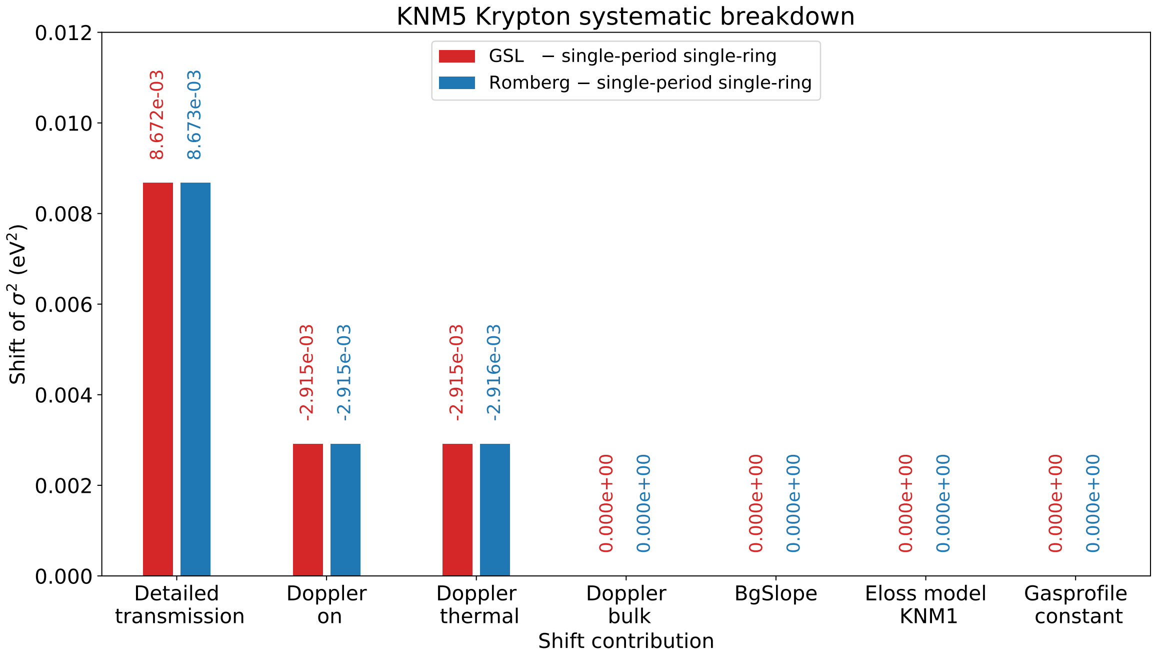

Figure 5.16: Shift of σ^2 dependent on various model settings for two different integration methods, the GSL and the Romberg integrator. The shift is in comparison to the mean value of $4 \times 10^{-3}\,\text{eV}^2$. The depiction is based on the routine introduced in subsection 5.2.2. The shifts on σ^2 are independent on the used integration method.

integration since the upper limit is infinite. This is because the Lorentzian distribution of the lines stretches out to infinity. The Romberg integration method can only handle finite integrals, thus a cut-off needs to be used. An advantage of the GSL integration method is that it can transform the infinite integration interval without using a cut-off(3). A more practical advantage of the GSL method is that it saves computation time compared to the Romberg method. The Romberg method tries to achieve a certain precision in every integration interval, which can lead to problems for intervals with few or no counts. GSL provides an adaptive integration procedure which divides integration intervals in such a way that overall errors decrease and that local difficulties can be found and handled. This even works for integrable singularities. Therefore, the GSL method would be the integrator of choice if its results are consistent with the ones of the Romberg implementation. Since important analysis have been done with one of the algorithms an agreement between the results of both would ensure the comparability of the different analysis results.
This study cross-checks if both integration methods provide the same results. The comparison based on the systematic studies of the model regarding the broadening σ^2 is shown in figure 5.16. The same comparisons regarding E_{N2} and Δ_{10} can be found in

(3) There is an experimental cut-off since the very few electrons with a very large surplus energy are not properly and adiabatically transported through the experiment and are therefore not contributing to the measured spectrum. This is not implemented in the model due to its complexity and since the effect is negligibly small for the N lines.

section B.1 in figures B.5 and B.6. For all studies no significant disagreement between the two integration methods could be found.

5.3 Comparison of Different Measurement Modes, Settings and Analysing Strategies

In the following section various measurement modes, settings and analysing strategies are compared based on measurements conducted in KNM4. The measurement settings and run numbers are listed in table A.1. At the end an optimal configuration of measurement and analysis is suggested. Regarding the results of the sensitivity studies in section 5.2, the fits were performed including all relevant systematic effects. The model includes the synchrotron radiation and detailed transmission for unscattered electrons. The Doppler effect is not included since its effect on the broadening is Gaussian distributed and thus can be manually subtracted in squares after the fit. Besides the "Stat." fit parameters, ΔE_{N23} and I_{N3}/I_{N2} were fitted with the regarding pull terms. Furthermore, B_{ana} was added as a free parameter since the sensitivity studies obtained it to have a relevant effect on the uncertainties of the plasma parameters. Furthermore, possible deviations of the magnetic field strength from the reference values obtained by simulations can influence the values of the broadening if B_{ana} is fixed. All data of a measurement can be stacked if there are no strong drifts of the settings of the experiment.

5.3.1 Comparison of Analysing Strategies concerning Value Fluctuations into Unphysical Regions

Some of the N line parameters exhibit expected values close to an unphysical region < 0. This concerns the broadening σ^2, the natural line widths Γ_{N2} and Γ_{N3} as well as the rate of the background c_{Bg}. It is expected that the obtained values of those parameters fluctuate into the unphysical region since their mean values lie close to the physical boundary and the width of their distribution is broad enough to cross the boundary if allowed. To enable this fluctuation a mathematical extension of the physical region covering the unphysical region must be chosen. This extension should be constructed in such a way that the distribution of the resulting values in fact is Gaussian to allow simple averaging and calculation of the uncertainties. Additionally, these fluctuations into the unphysical region can only appear if corresponding fluctuations of the counts are possible. Otherwise the distribution must be cut off at the physical limit.

For the mathematical extension towards the unphysical region for σ^2 a point of reflection ansatz is used in the model implemented in KaFit [BGZ+11]

$$V(\sigma^2 < 0) = 2V(\sigma^2 = 0) - V(|\sigma^2|)\,. \tag{5.4}$$

Here, V denotes the Voigt line profile. Furthermore, the model sets negative counts to zero while lowering the other counts by a corresponding constant factor. Based on

Table 5.1: Impact of limits on the parameters c_{Bg}, σ^2, E_{N2} and B_{ana} for the KNM4 MTD IE measurement in 2.7 G. Shown are the weighted means of the parameters for the pixels of rings 0 to 9. For σ^2 and E_{N2} Minos errors and therefore asymmetric weighted means have been calculated. For parameters with a lower limit only the upper uncertainty was used to calculate a symmetrical weighted mean. To symbolise the asymmetry of the uncertainties the lower uncertainty on those means is calculated by means of $1/\sqrt{\sum_i \left(1/\sigma_i^-\right)^2}$ using the lower Minos errors σ_i^-. Lower errors close to zero are symbolised by ϵ. For the free fit pixel 101 was excluded since the fit values were several orders of magnitude off. Pixel 6 was excluded for c_{Bg} of the free fit because the uncertainty on this value was several orders of magnitude lower than the other uncertainties. $\overline{E_{N2}}$ denotes $E_{N2} - 32\,136\,\mathrm{eV}$. Additionally, the normalised χ^2 is given for each fit.

Parameter	Free fit	Fit with $c_{\mathrm{Bg}} \geq 0$	Fit with $c_{\mathrm{Bg}} \geq 0 \wedge \sigma^2 \geq 0$
$c_{\mathrm{Bg}}/\mathrm{mcps}$	-589±21	0±1	0±1
$\sigma^2/10^{-3}\,\mathrm{eV}^2$	$1.72^{+0.22}_{-0.18}$	$1.01^{+0.21}_{-0.15}$	$1.40^{+0.20}_{-\epsilon}$
$\overline{E_{N2}}/\mathrm{meV}$	$702.6^{+1.9}_{-1.8}$	$704.3^{+3.8}_{-3.8}$	$693.8^{+1.8}_{-1.8}$
$B_{\mathrm{ana}}/\mathrm{G}$	2.636±0.003	2.638±0.003	2.629±0.003
χ^2/N_{DOF}	1.36	1.48	1.50

this model extension the KNM4 MTD IE measurement data for the 2.7 G setting has been analysed. When fitting the data without constraining the broadening and the background rate by a limit a negative background rate of (-589 ± 21) mcps results, as shown in figure 5.17. Fits without a constraining limit on any of the parameters are in the following referred to as free fit. A negative background rate is clearly unphysical and cannot appear by fluctuations of counts. Therefore, a limit should be set so that $c_{\mathrm{Bg}} \geq 0$. It is furthermore assumed, that the model extension for negative backgrounds might reduce the line width, since it causes a constant shift on all count rates. This would mean, that the negative background rate is a compensation effect. Since the normalised χ^2 for this fit is with $1.36 > 1$ there must be some discrepancy between the measurement data and the used model. It is unclear if a measurement setting was different than expected or if the model does not describe the experiment properly in this case. For the analysis with $c_{\mathrm{Bg}} \geq 0$ almost all values of the background rate run into the limit at 0, giving $c_{\mathrm{Bg}} = 0 \pm 1$ mcps. When considering the development of the other parameters, summarised in table 5.1, one finds that setting this limit reduced the broadening from $\sigma^2 = (1.72^{+0.22}_{-0.18})10^{-3}\,\mathrm{eV}^2$ to $(1.01^{+0.21}_{-0.15})10^{-3}\,\mathrm{eV}^2$. This shows, that the negative background has the same effect as a smaller broadening, it reduces the line width. The N_2 line position and magnetic field strength do not change significantly by setting $c_{\mathrm{Bg}} \geq 0$. The results for σ^2 for the free fit and the fit with the limited background rate are shown in figure 5.18 and figure 5.19, respectively. For the results of the free fit fluctuations into the negative regime are visible, but the distribution is still reminiscent of a Gaussian distribution. When setting the limit $c_{\mathrm{Bg}} \geq 0$, the mean value is visibly lowered by a second accumulation of values in the negative region.

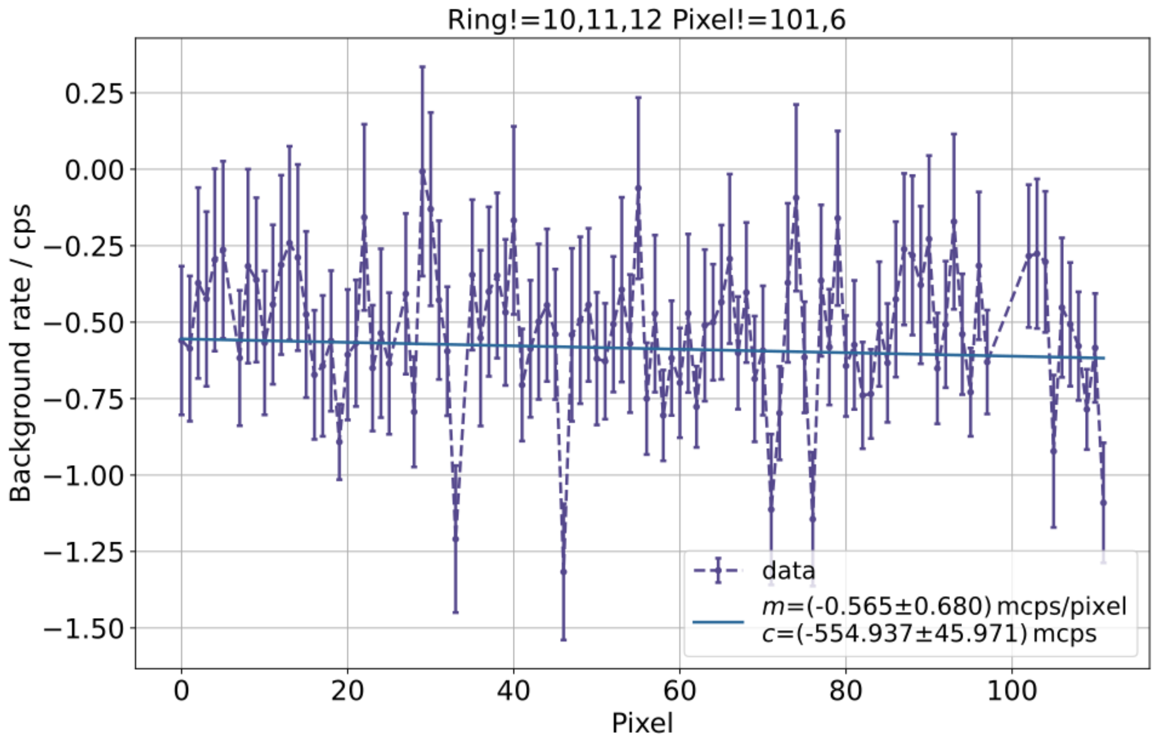

Figure 5.17: Background rate for the KNM4 MTD IE measurement at 2.7 G obtained by a pixelwise fit without limits on parameters (free fit). Shown are the pixelwise values of rings 0 to 9, excluding pixels 101 and 6. The linear fit gives the values of the slope m and the offset c. The weighted average is $c_{\mathrm{Bg}} = (-589 \pm 21)$ mcps.

This could hint that setting the limit might have created a second minimum of the negative log-likelihood. This distribution might be due to the natural line width being fixed at a too large value of 10 meV. If this value was chosen too large the broadening σ^2 would try to compensate for it leading to low or even negative fit results. Since the line width is composed of a more complicated relation than just the sum of the broadening and the natural line width, the broadening cannot simply compensate for a wrong setting of the natural line width. Therefore, it is expected that the obtained values of the broadening do not show a Gaussian distribution.
Furthermore, a reduction of the line width could be due to the used mathematical model extension for σ^2, described by equation 5.4. Since the Voigt profile $V(|\sigma^2|)$ is broader than $2V(\sigma^2 = 0)$ the underlying spectrum could be described by a W line shape. An example is shown in figure 5.21. This line shape shows an underfluctuation of the count rates at both sides of the line making the width of the line profile smaller when being convoluted with the transmission function. Those underfluctuations are only possible for a large enough background, since the corresponding count rates cannot be negative. Furthermore, the line must have a width > 0, otherwise it cannot obtain a W line shape. Overall, this concept is not fully understood yet and needs further investigations. The increase of the normed χ^2 to 1.48 compared to the free

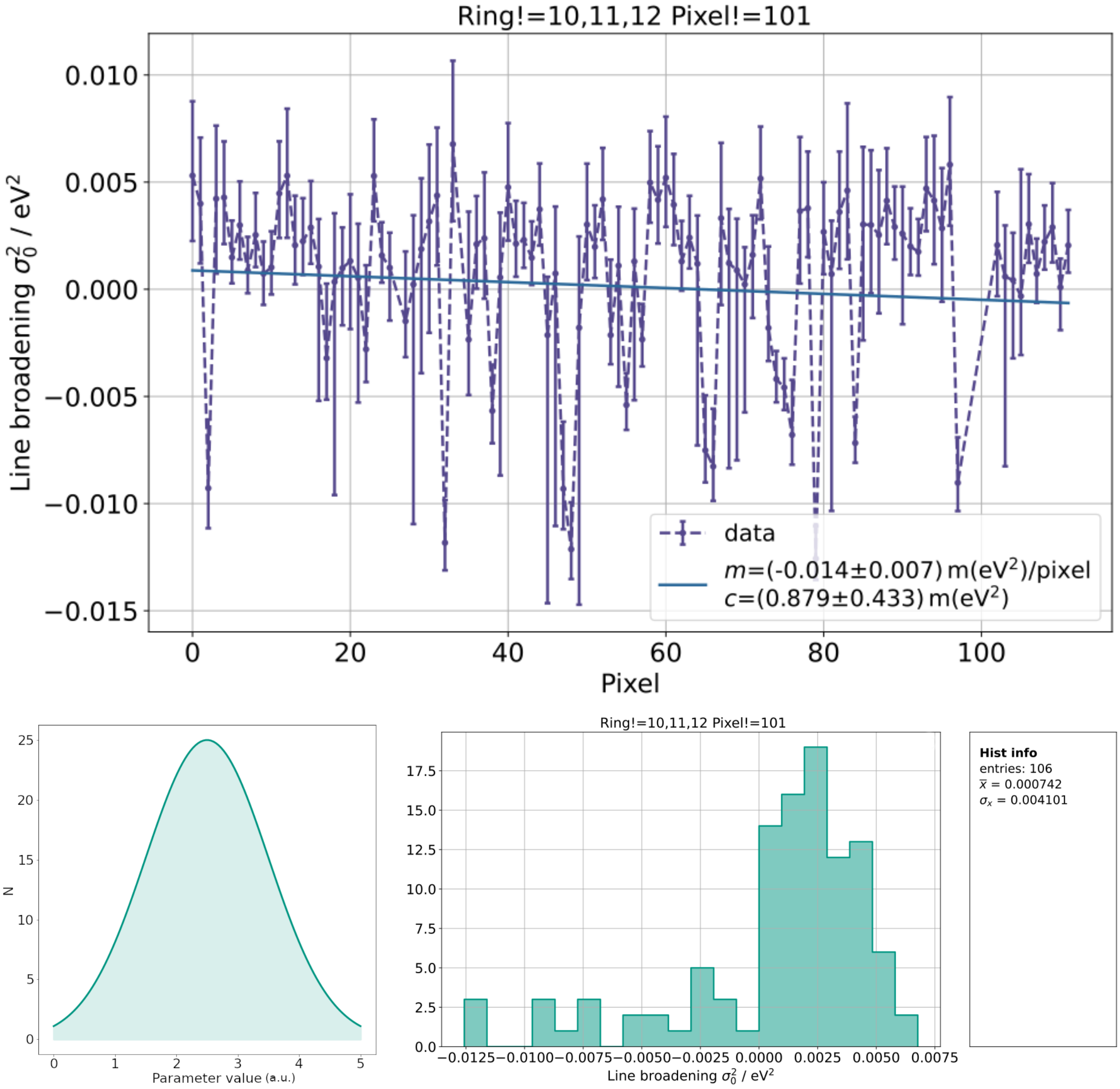

Figure 5.18: σ^2 for the KNM4 MTD IE measurement at 2.7 G obtained by a pixelwise fit without limits on parameters (free fit). Shown are the pixelwise values of rings 0 to 9 (upper plot) and their histogram (lower right plot). The linear fit in the upper plot gives the values of the slope m and the offset c symmetrical weighted by the upper errors. The asymmetric weighted average is $\sigma^2 = (1.72^{+0.22}_{-0.18})10^{-3}\,\text{eV}^2$. The histogram gives the unweighted mean $\bar{x}$ and the standard deviation σ_x. The lower left plot shows the presumed distribution of the histogram, a Gaussian distribution. The histogram deviates from the Gaussian distribution due to a large tail in the negative region. Possibly the model extension to negative values is inaccurate. Additionally, the normalised χ^2 is with 1.36 too large and hints to discrepancies between the data and the model.

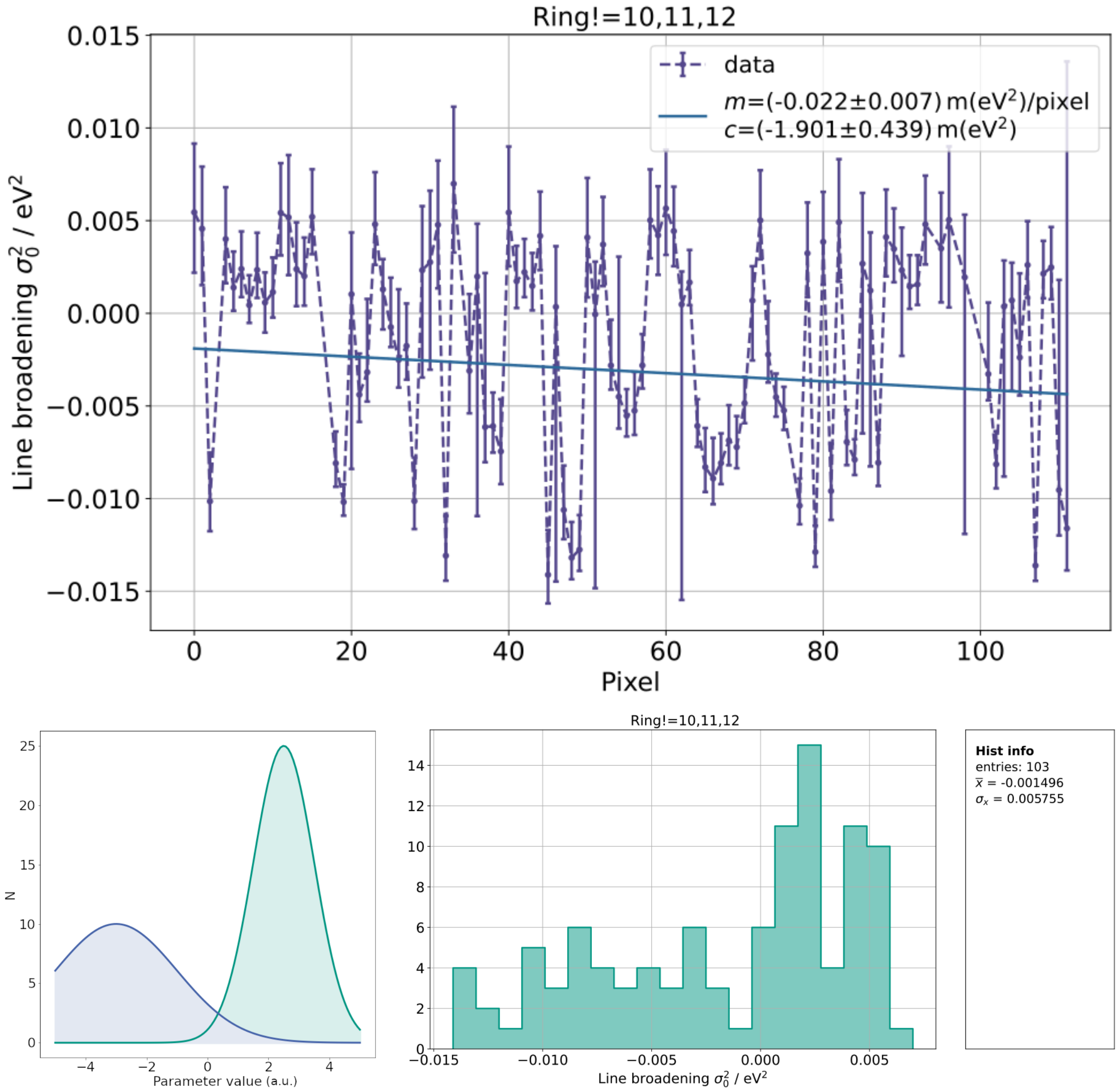

Figure 5.19: σ^2 for the KNM4 MTD IE measurement at 2.7 G obtained by a pixelwise fit with a limit on the background rate (fit with $c_{\mathrm{Bg}} \geq 0$). Shown are the pixelwise values of rings 0 to 9 (upper plot) and their histogram (lower right plot). The linear fit in the upper plot gives the values of the slope m and the offset c symmetrical weighted by the upper errors. The asymmetric weighted average is $\sigma^2 = (1.01^{+0.21}_{-0.15})10^{-3}\,\mathrm{eV}^2$. The histogram gives the unweighted mean $\bar{x}$ and the standard deviation σ_x. The lower left plot shows the presumed distribution of the histogram, two Gaussian distributions, one in the positive and one in the negative range.

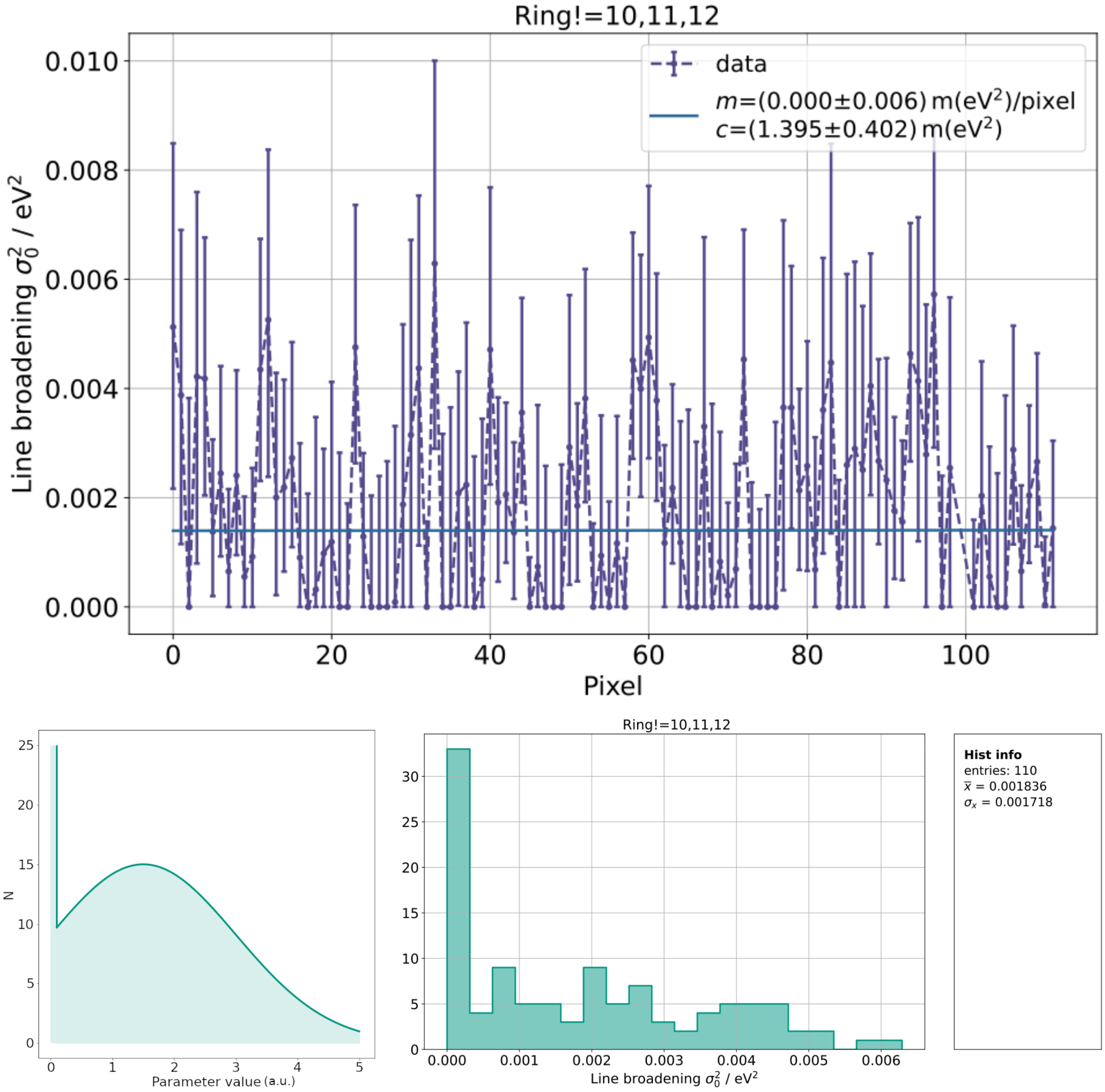

Figure 5.20: σ^2 for the KNM4 MTD IE measurement at 2.7 G obtained by a pixelwise fit with a limit on the background rate and on the broadening (fit with $c_{\mathrm{Bg}} \geq 0 \wedge \sigma^2 \geq 0$). Shown are the pixelwise values of rings 0 to 9 (upper plot) and their histogram (lower right plot). The linear fit in the upper plot gives the values of the slope m and the offset c symmetrical weighted by the upper errors. The symmetric weighted average is $\sigma^2 = (1.40^{+0.20}_{-\epsilon})10^{-3}\,\mathrm{eV}^2$ using the upper errors. The lower uncertainty on the average reflects the limited uncertainties of the lower errors and was calculated separately. Lower errors close to zero are symbolised by ϵ. The histogram gives the unweighted mean $\bar{x}$ and the standard deviation σ_x. The lower left plot shows the presumed distribution of the histogram, a Gaussian distributions with values accumulating at the limit $\sigma^2 = 0$.

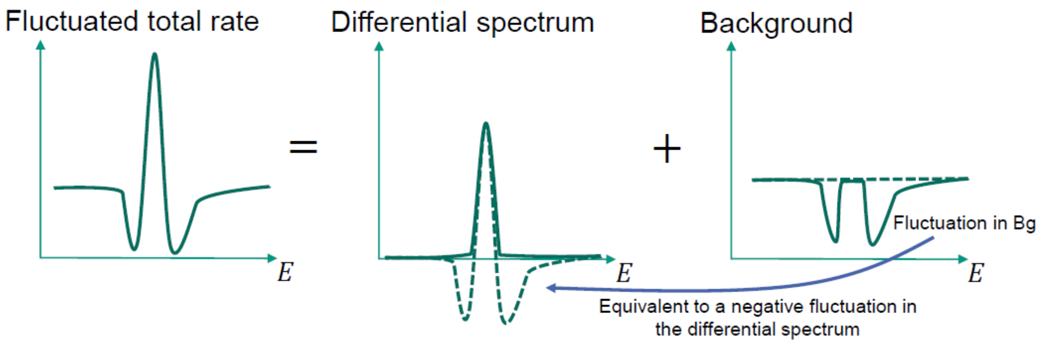

Figure 5.21: Hypothesis of how fluctuations can cause smaller line widths. A W line shape in the differential spectrum (dotted line) is needed to obtain a smaller total line width after the convolution with the transmission function. For narrow lines the underfluctuations close to the line causing the W line shape would have to extend in the negative region. This is not possible for the differential spectrum (solid line) since negative counts would be needed. But when adding a background the corresponding underfluctuations for the W line shape become possible. The fluctuations of the background might look differently than depicted here, since only the differential spectrum is convoluted with the transmission function and the background is added later. Figure from [Mac21b].

fit with 1.36 might be due to the peculiar model extension for the background rate leading to unphysical negative background rates.

Since the mathematical model extension does not provide a Gaussian distribution yet, a limit was set not only on the background rate but also on the broadening. The result for σ^2 is shown in figure 5.20. In this case a Gaussian distribution is expected with a positive mean value and with the amount of values assumed to fluctuate into the negative region accumulating at the limit $\sigma^2 = 0$. This is approximately what was obtained in the fit, although the Gaussian seems to be very flat. In this case it is not meaningful to use the lower errors to determine the weighted average since the errors are cut at the set limit. As an approximation the upper errors are used as symmetrical errors giving $\sigma^2 = (1.40^{+0.20}_{-\epsilon})10^{-3}\,\mathrm{eV}^2$. The displayed lower error was calculated separately by combining the lower errors to symbolise the asymmetry caused by the limit. ϵ denotes a lower errors close to zero. This is the case if a fit result lies in the limit causing the lower error to be zero. This notation is used in all following sections. In order to determine the best estimate for σ^2 from the distribution one could perform Monte Carlo simulations where the real value is varied until the Monte Carlo distribution is approaching the distribution of the fitted values. The best estimate for σ^2 is obtained when the distribution of the fitted values and the Monte Carlo simulated distribution are equivalent. Here, a large number of entries of the histogram is needed. Nevertheless, implementing this method exceeds the time frame of this thesis. Another approach would be to combine several different fits by restraining them to have a common fit parameter. With this one could set a common broadening for every ring or the full detector while calculating other parameters ring- or even

Table 5.2: Comparison of the 1 G and 2.7 G magnetic field settings by reference to the values of σ^2 and E_{N2}. The magnetic field settings are compared for the MTD IE and the ramping measurement mode. The ramping velocity is 30 mV/s. Shown are the weighted means of σ^2 and E_{N2}. The averages for the 1 G and 2.7 G settings cover the pixelwise values of rings 0 to 3 and of rings 0 to 9, respectively. $\overline{E_{N2}}$ denotes $E_{N2} - 32\,136\,\mathrm{eV}$. Additionally, the normalised χ^2 is given for each fit. The data was obtained in the KNM4 measurement campaign.

Parameter	MTD IE 1 G	MTD IE 2.7 G	Ramp 1 G	Ramp 2.7 G
$\sigma^2/10^{-3}\,\mathrm{eV}^2$	$3.23^{+0.26}_{-0.19}$	$1.40^{+0.20}_{-\epsilon}$	$5.01^{+0.28}_{-0.21}$	$1.73^{+0.18}_{-\epsilon}$
$\overline{E_{N2}}$/meV	$582.4^{+2.4}_{-2.4}$	$693.8^{+1.8}_{-1.8}$	$589.7^{+2.1}_{-2.1}$	$700.1^{+1.4}_{-1.4}$
$\mathrm{n}\chi^2/N_{\mathrm{DOF}}$	2.42	1.50	1.03	0.94

pixelwise. As an example one could fit one ring with twelve different values for the line position and other parameters, but only with one common broadening to increase the statistical sensitivity on the latter. This would allow to directly obtain the estimates of the broadening with a single fit, leading to a higher statistic and therefore a more narrow distribution. Both methods are in preparation for future analysis.
Considering the other parameters it is visible that when limiting the broadening the magnetic field strength B_{ana} decreases by around 0.01 G. This has the effect of causing a more narrow transmission function which can compensate for a supposedly too large total line width. Also the line position is lowered by around 10 meV compared to the resulting values without a limit on σ^2. The normalised χ^2 only increases slightly to a value of 1.5.

For the following analysis in this thesis limits are used on the background rate and broadening, if not stated differently. This method is chosen since the mathematical model extensions for the unphysical region of the parameters are not fully understood and do not result in Gaussian distributions of the obtained fit values. If indeed a too large value for the natural line width of the N_{23} lines was chosen, this will show in a slightly smaller line position and magnetic field strength and will effect the broadening.

5.3.2 Comparison of Magnetic Field Settings

In the KNM4 krypton measurement campaign measurements in the 1 G and 2.7 G magnetic field setting have been performed. By comparing the values of σ^2 and E_{N2} for those settings systematic shifts caused by inaccuracies in the field modelling can be studied. In the optimal case of finding the same values for both magnetic field settings one can assume that the model correctly and precisely reflects the magnetic setup of the experiment.
The obtained values are presented in table 5.2. Compared are the magnetic field settings for the MTD IE and the ramping measurement mode. It is obvious for both

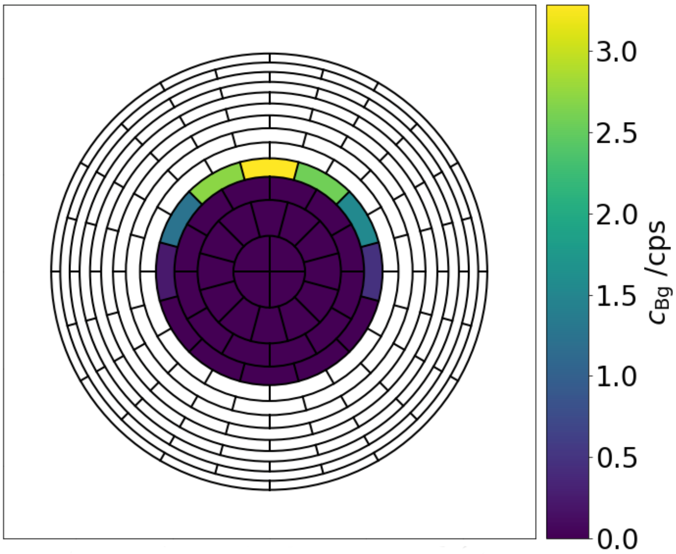

Figure 5.22: Background rate of the MTD IE measurement at 1 G mapped onto the FPD. It shows an unusually increased background rate c_{Bg} for the upper half of ring 3 which is vertically symmetric. This could be due to the electrons being scattered on the wire electrodes or on some part of their mounting.

Table 5.3: Comparison of the ringwise standard deviations of the ringwise line positions for the 1 G and 2.7 G magnetic field settings. The corresponding fit results of the KNM4 MTD IE measurements are shown in figure 5.23. The standard deviations are each compared with the averaged total ("Stat+Sys") uncertainty for both magnetic field settings by their quadratic difference Δ. The total uncertainties are 15.0 meV for the 1 G setting and 19.4 meV for the 2.7 G setting. Marked in red are the values of the quadratic difference for which the standard deviation is larger than the statistical uncertainty.

	1 G		2.7 G	
Ring	Std/meV	Δ/meV	Std/meV	Δ/meV
0	8.2	12.6	9.731	16.7
1	16.2	5.9	13.3	14.1
2	22.1	16.2	12.1	15.1
3	26.7	22.1	17.1	9.0

measurement modes that the 1 G setting leads to a much larger broadening than the 2.7 G setting. For the MTD IE measurement mode one finds a significantly increased broadening by a factor of 2.4 for the 1 G setting compared to the 2.7 G setting. The discrepancy between the magnetic field settings regarding σ^2 is even larger for the ramping mode. Here, the broadening increases by a factor of 2.9 . The difference between the values are so large compared to their uncertainties that it is unlikely caused by the method of determining the average. This hints to additional systematic factors not covered by the analysis which cause an additional broadening in the 1 G setting. The

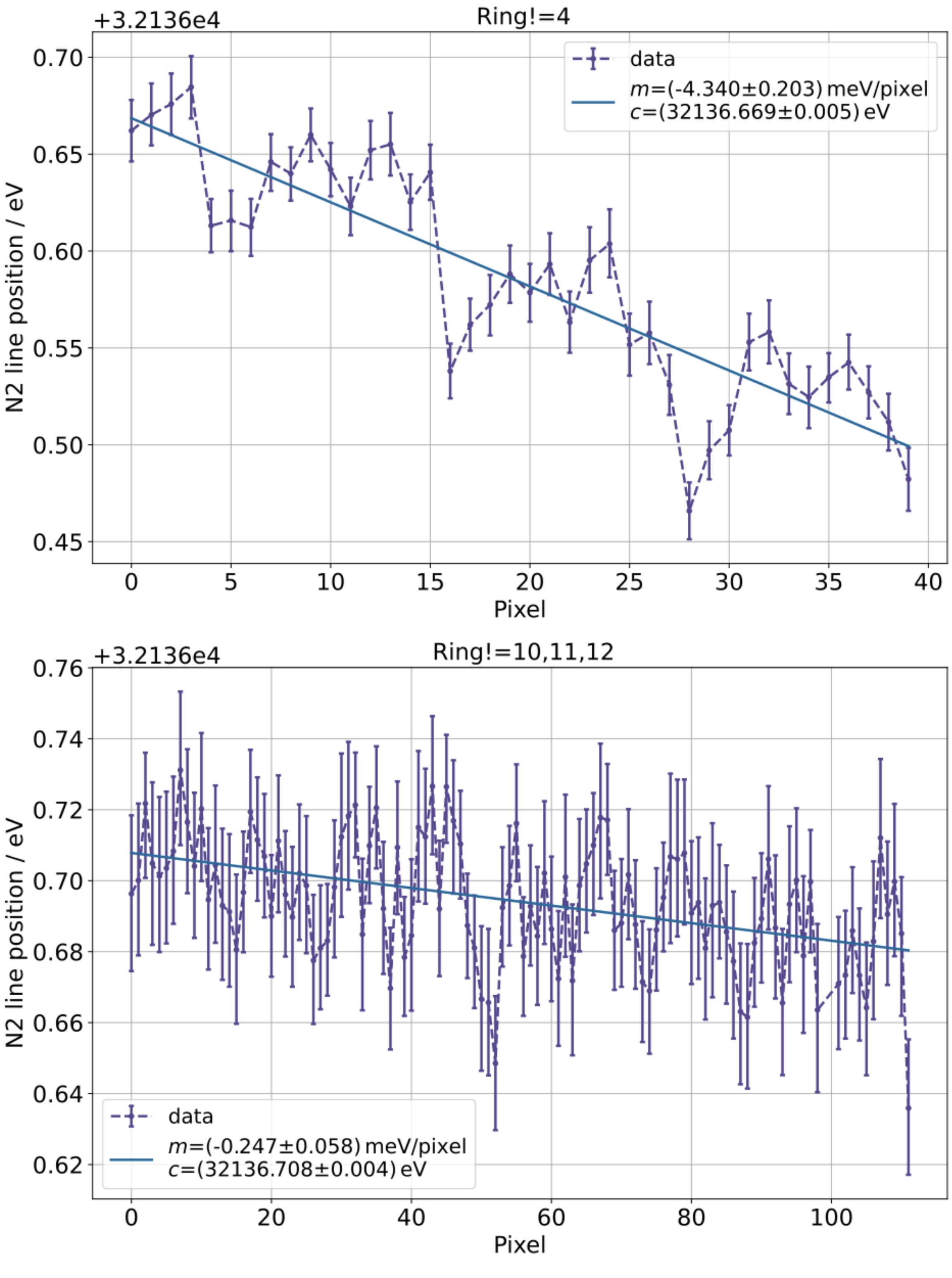

Figure 5.23: Comparison of the pixelwise N_2 line position for 1 G (upper plot) and 2.7 G (lower plot) magnetic field setting. The fitted data originates from the KNM4 MTD IE measurements. The line positions for the 1 G setting show a ringwise structure. The corresponding ringwise averages can be found in table 5.4. Their ringwise standard deviation can be found in table 5.3.

analysis already accounts for the effect of the electric potential distribution within a pixel, discussed in subsection 5.1.4. Thus, this source of systematic effect is already considered. The same effect can also occur for the magnetic field, which is not covered in the analysis. With equation 3.2 and a variance of the magnetic field inhomogeneity at the order of $10^{-6}\,\mathrm{G}^2$ one can assume an effect on the energy resolution for the N_{23} line electrons at the order of meV. Therefore, the resulting effect can be considered as small. Potentially, collisions of the electrons with the vessel could effect the broadening, since the 1 G setting is the only one where this happens for the electrons of the outer rings. As shown in figure 5.22, a significantly increase background for the upper pixels of ring 3 was found for all measurements in the 1 G setting. It is presumed that the electrons are scattered on the wire electrodes or on some part of their mounting. Since this is only visible in the 1 G measurements it might suggest an even stricter pixel cut for the analysis of this magnetic field setting. Furthermore, a problem with the magnetic field simulation for the 1 G setting used in the analysis was obtained. Values for the magnetic field in the analysing plane of around 1.78 G were found while values around 1 G were expected. The error in the simulation was due to a wrong setting of the air coil currents. Wrong values for the magnetic field strength in the analysing plane are compensated by the fit since B_{ana} is included as a free fit parameter. However, that does not apply to the simulation of the other field values. Based on the simulation of the magnetic field in the analysing plane the values for the electric field are mapped onto the FPD pixels. Therefore, the error in the simulation leads to a wrong mapping of the electric retarding potential to the pixels. This clearly has an influenced on the results of the measurements in the 1 G setting. Consequently, a re-analysis of the data is needed. Overall, the origin of the additional broadening for the 1 G setting is still not fully understood and will need further investigations.

Comparing the N_2 line positions listed in table 5.2 one can see that for both measurement modes the line position is 110 meV higher in the 2.7 G setting than in the 1 G setting. This discrepancy could, as discussed for the broadening, be caused either by additional collision effects of the electrons on the vessel of the 1 G setting or with high probability by the error in the simulations of the fields for the 1 G setting. When considering the pixelwise N_2 line positions, shown in figure 5.23 for the MTD IE measurements, a strong slope of (-4.340 ± 0.203) meV/pixel is visible for the 1 G setting. The slope of the 2.7 G measurement amounts only to (-0.247 ± 0.058) meV/pixel. This behaviour can equally be found for the ramping measurements. Since the measurements were conducted at a rear wall voltage of 0 V, a radial dependency on the line position can in general be expected. Furthermore, the measurements were conducted within one day, thus, strong drifts between the measurements are not expected. Thus, the comparably large slope found for the 1 G setting is most probably due to the wrong field simulations and the therefore wrong mapping of the electric retarding potential onto the pixels. Furthermore, a ringwise structure can be found in the pixelwise values of the line position in 1 G. This structure allows to draw conclusions about the alignment of the experiment. If all components of the experiment are correctly aligned then the electrons coming from the center of the source would pass the center

Table 5.4: Comparison of the MTD, MTD IE and ramping measurement modes by means of σ^2 and E_{N2}. All measurements were performed in the 1 G setting. "Ramp" refers to the ramping mode with a ramping velocity of 30 meV/s. $\overline{E_{N2,i}}$ denotes $E_{N2} - 32\,136$ eV for ring i. Without the index i the value refers to the weighted average over rings 0 to 3. The uncertainties on σ^2 are calculated as explained in subsection 5.3.3. Additionally, the normalised χ^2 is given for each measurement mode.

Parameter	MTD	MTD IE	Ramp
$\sigma^2/10^{-3}\,\mathrm{eV}^2$	$1.56^{+0.26}_{-\epsilon}$	$3.23^{+0.26}_{-0.19}$	$5.01^{+0.28}_{-0.21}$
$\overline{E_{N2}}$/meV	$579.6^{+2.6}_{-2.6}$	$582.4^{+2.4}_{-2.4}$	$589.7^{+2.1}_{-2.1}$
$\overline{E_{N2,0}}$/meV	$680.8^{+8.4}_{-8.5}$	$673.1^{+8.0}_{-8.0}$	$697.1^{+6.2}_{-6.3}$
$\overline{E_{N2,1}}$/meV	$632.4^{+4.4}_{-4.5}$	$635.3^{+4.2}_{-4.2}$	$641.4^{+3.9}_{-4.0}$
$\overline{E_{N2,2}}$/meV	$565.8^{+5.0}_{-5.0}$	$568.5^{+4.5}_{-4.5}$	$578.5^{+3.7}_{-3.8}$
$\overline{E_{N2,3}}$/meV	$514.1^{+4.5}_{-4.7}$	$520.2^{+4.2}_{-4.2}$	$531.5^{+3.8}_{-3.8}$
nχ^2	2.27	2.42	1.03

of the analysing plane would be detected at the center of the FPD. Thus, for a perfect alignment and a radially symmetric potential the pixels within a ring would give one common value for the line position, leading to a steplike structure for the pixelwise values. If this was the case, then the standard deviation of the values within a ring must be equal or smaller than the individual total uncertainty per pixel. For larger standard deviations, additional effects must be considered which could be caused by an imperfect alignment. Since the performed fit only provides an uncertainty including systematic contributions, the standard deviation can become smaller than the total uncertainty. However, in principle the standard deviation should not become smaller than the statistical uncertainty. The standard deviations per ring and the quadratic difference Δ between the standard deviation and the averaged fit uncertainty per pixel are shown in table 5.3 for both magnetic field settings. For the 1 G setting only ring 0 fulfils the condition for a small enough standard deviation of 8.2 meV. The standard deviations of the other rings are larger than the averaged total uncertainty of 15.0 meV. The steplike structure is nevertheless clearly visible for the pixelwise values at the 1 G setting. Since for this specific magnetic field setting large areas of the analysing plane are mapped onto only a few pixels, it must be more sensitive to the alignment than other settings and therefore shows this structure. For the 2.7 G setting, figure 5.23 does not show a steplike pattern for the pixelwise line position values. Nevertheless, for this magnetic field setting all ringwise standard deviations are smaller than the averaged total uncertainty of 19.4 meV. Thus, the alignment seems to be sufficient for the 2.7 G magnetic field setting.

5.3.3 Comparison of Measurement Modes

A measurement can be conducted in one of three different measurement modes, the MTD, MTD IE and ramping measurement mode, which are introduced in subsection 4.3.3. The MTD measurement mode is frequently used and already well implemented and understood. In contrast, the MTD and ramping measurement modes are of experimental nature, seeking to reduce dead time between single measurement points and thereby making the measurement process more efficient. The comparison is able to show, if additional systematic effects caused by the new settings influence the observables and how well the new modes are already understood.
The three measurement modes are compared for the 1 G setting. The resulting values for the parameters of interest σ^2 and E_{N2} can be found in table 5.4. Since the 1 G setting shows a ring-dependent pattern of the pixelwise N_2 line positions, ringwise averaged values are additionally provided in the table. Regarding σ^2, it is visible that the broadening increases for the new measurement modes, the MTD IE and ramping mode. For the MTD mode σ^2 amounts to $\left(1.557^{+0.260}_{-\epsilon}\right)\ 10^{-3}\,\mathrm{eV}^2$. Since a lower limit is used on σ^2 for the fit, this value is symmetrically weighted using the individual upper errors. The lower error is calculated separately. ϵ denotes a lower error close to zero. This proceeding is applied to all following values of σ^2 if not mentioned otherwise. When using the inner electrode to set the retarding voltage, as it is done for the MTD IE mode, σ^2 increases by a factor of 2.1 . This is expected since the effect of the inner electrode voltage dependent potential depression, discussed in subsection 5.1.5, is not yet covered by the analysis. To include this effect into the analysis the fixed value of the vessel potential must be known at the order of 100 meV. This was not the case for the KNM4 measurements, since only the sum of the vessel and IE voltage could be read out with the needed precision. Furthermore, the energy scaling factor for the inner electrode voltage dependent potential depression must be well known and understood. Additional measurements in KNM5 were conducted by the KATRIN krypton team to obtain and cross-check the predicted energy scaling factor of 8.8 meV/eV from simulations by J. Behrens. Unfortunately, discrepancies were found between measurement and simulation, which could not completely be resolved. Namely, the measurements seemed to show a radial dependent effect, which was not expected from the simulation. Therefore, further investigations will be necessary to fully understand the MTD IE measurement mode and to consistently implement it into the measurement and analysing routines.
The broadening σ^2 increases even further when using the ramping mode. Here, it is referred to the ramping mode with a ramping velocity of 30 meV/s. σ^2 shows an increase by a factor of 3.2 compared to the MTD mode. As for the MTD IE measurement mode the broadening is again effected by the inner electrode voltage dependent potential depression. It is assumed to increase the broadening. Furthermore, the binning effect explained in subsection 5.1.2 might be the source for the additional broadening compared to the MTD IE mode. This effect can only appear for ramping measurements since the continuous ramping of the retarding voltage makes it necessary in the first place to bin the data into measurement data points. For the other modes those points

are predefined by the MTD within uncertainty. To further investigate and develop the ramping mode one needs to quantify the binning effect on σ^2 separately from other systematic effects and to find a concept to account for this effect in the analysis. As a first attempt obtaining the standard deviation per bin and subtracting it from the broadening might give a viable result at leading order.
Regarding the mean N_2 line position, table 5.4 shows a slight increase for the MTD IE mode compared to the MTD mode by 2.8 meV and also for the ramping mode compared to the MTD IE mode by 7.3 meV. The corresponding uncertainties are at the order of 2 meV. This increase in line position can be found not only for the overall average but also for the rings 1 to 3. Only the MTD IE value of ring 0 does not fit in the pattern. This could be due to fluctuations since ring 0 comprises only four pixels and the statistical errors are of the same order as the differences between the values. Since the values of the MTD and MTD IE mode do not differ significantly, the influence of the inner electrode voltage dependent potential depression seems to be minor. However, there seem to be relevant systematic effects influencing the line position which must be ramping mode specific. It can be excluded that the difference in line position is due to a work function shift since the measurements were performed consecutively within one day. A possible systematic effect already discussed with regard to its influence on σ^2 is the binning. Another ramping mode specific systematic could lie in the timing problems of this mode, discussed in subsection 5.1.3. An imprecise knowledge of the retarding voltage leads to a distortion of the spectrum. If the ramping of an up-scan started earlier than the associated time stamp this would mean that a higher retarding voltage is already reached than one would expect at that time. The analysis of this data would then show a reduced value for the line position caused by the offset of the retarding voltage. In analogy, the line position will be shifted to higher values if the ramping of a down-scan would start earlier than expected. This line shift effect has been observed in an early analysis of the KNM4 ramping measurement data. For this analysis the data of the up- and down-scans were stacked separately with each fit stacking six runs. The result is shown in figure 5.24. Since the line positions for the up-scans are shifted to lower values and the line positions for the down-scans are shifted to higher values it is plausible that the rampings started earlier than expected. The amount of the shift seems to be constant over the measurement time, since the values of the earlier and later taken runs are in good agreement. The shift of the line position between up- and down-scans seems to amount from around 100 meV to 150 meV for a ramping velocity of 30 mV/s. Since this is only the result of an early analysis, a re-analysis is needed to correctly quantify the effect. Overall this shows, that timing problems of the ramp scans can lead to a significant effect on the values of the line position. It is further assumed, that also the broadening might be affected by the line shift when stacking up- and down-scans together.

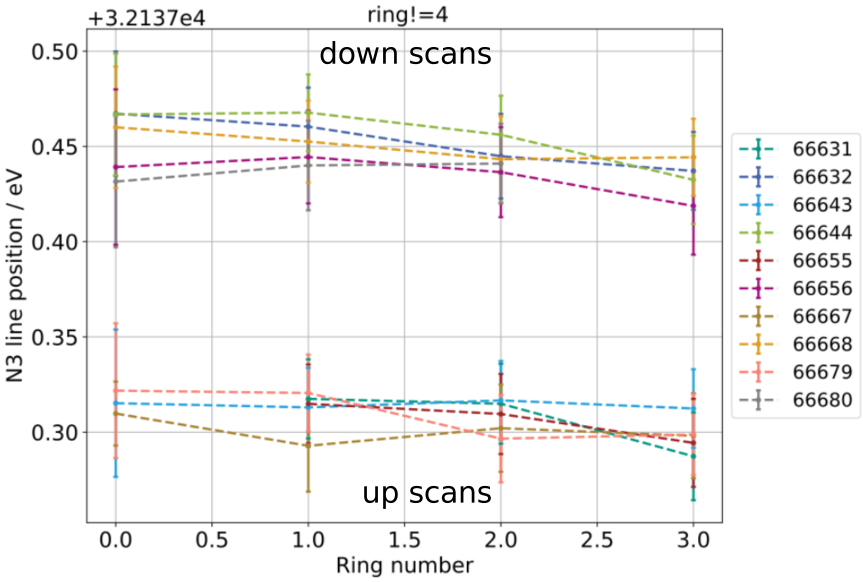

Figure 5.24: Ringwise N_3 line position of the KNM4 ramping measurements effected by the line shift. The measurement was conducted at the 1 G magnetic field setting with a ramping velocity of 30 mV/s. The data of the up- and down-scans is stacked separately with each fit stacking six runs. For each fit the first of the stacked six run numbers is shown on the right of the plot.

5.3.4 Comparison of the Ramping Velocities and Bin Widths of the Ramping Measurements

For further investigations of the ramping mode, measurements with different ramping velocities were conducted in KNM4. Compared are the ramping velocities of 30 mV/s, 60 mV/s and 90 mV/s. It is expected that the impact of the binning increases for higher velocities.
To simulate the binning effect the ramping measurements at 30 mV/s are additionally analysed using an adjustable binning of 60 mV or 90 mV, thereby making it comparable to the measurements with 60 mV/s and 90 mV/s ramping velocity. This is possible since the observed rates in the ramping mode are binned with 1 s intervals to produce the measurement points.
The results for the broadening σ^2 are shown in table 5.5. Regarding the values for the 30 mV/s ramping measurement analysed with different binning widths, there seems to be no clear relation between σ^2 and the binning. The 30 mV binning gives the largest broadening, which relates with a factor 2.4 to the smallest obtained broadening for the 60 mV binning. The broadening for the 90 mV binning is slightly larger compared to the 60 mV binning. If the impact of the binning effect would get stronger for larger binning widths a larger broadening for larger binning widths would have been expected. Thus, either there is no dependency of σ^2 on the binning or the method of obtaining the average might be not precise enough for parameters close to zero. The histogram of σ^2, visible in figure 5.25, shows that a significant part of the fit results with the 60 mV

Table 5.5: Comparison of $\sigma^2/10^{-3}\,\mathrm{eV}^2$ for different binning widths b. The data was obtained in the 1 G magnetic field setting for different ramping velocities in KNM4. For comparison the measurement at 30 mV/s, which equals a 30 mV binning, was additionally analysed with a 60 mV and 90 mV binning. The uncertainties on σ^2 are calculated as explained in subsection 5.3.3.

Binning b	Ramp at 30 mV/s	Ramp at b/s
30 mV	$5.01^{+0.28}_{-0.21}$	$5.01^{+0.28}_{-0.21}$
60 mV	$2.10^{+0.21}_{-\epsilon}$	$6.25^{+0.40}_{-\epsilon}$
90 mV	$2.64^{+0.23}_{-\epsilon}$	$2.56^{+0.33}_{-\epsilon}$

binning went into the limit. Those values additionally show an underestimated upper uncertainty, which distorts the weighted average. Therefore, the small values for σ^2 might be caused by the amount of fit results in the limit shifting the average towards smaller values. This makes clear that using the weighted average is not suited to obtain the best estimate. As already discussed, instead a Monte Carlo method should be used for this purpose. Additionally, the large part of fit results in the limit for the larger binnings is probably due to lower statistics per fit compared to the 30 mV binning. Due to technical problems only 10 instead of 30 runs were stacked per fit for the larger binnings. The lower statistics per fit cause a broader distribution and therefore more values must end up in the limit. Therefore, equal statistics per fit are relevant for the comparability of values close to zero.

The results for σ^2 at different ramping velocities also do not show a clear dependency on the bin width. It is again visible that the values for σ^2 obtained by the 60 mV/s and 90 mV/s ramping measurement suffer from a significant amount of fit values in the limit. This is probably due to low statistics per fit, as already discussed. Here again, only 10 runs per fit could be stacked. Since an increasing ramping velocity corresponds to a shorter measurement time per run, the statistics per fit are even lower than for the fits using the adjustable binning. Therefore, the broadening for the 60 mV/s and 90 mV/s ramping velocity are expected to be larger than calculated with the weighted average. This shows, that the weighted average is not precise enough for parameters close to zero and must be obtained by Monte Carlo simulations or multi-fits.

When considering the fitted values for the magnetic field strength in the analysing plane B_{ana} in table 5.6 one can see that the estimates are increased for the measurements at ramping velocities 60 mV/s and 90 mV/s. The values for B_{ana} for the 30 mV/s ramping measurement analysed with different bin widths agree within the uncertainties. In contrast, B_{ana} for the 60 mV/s ramping measurement is increased by 80 mG compared to the 30 mV/s ramping measurement. The 90 mV/s ramping measurement gives an increase of 170 mG for B_{ana}. It seems like the systematic effect expected to give an additional broadening for the higher ramping velocities has led to a larger magnetic field strength in the fit, due to their correlation. However, B_{ana} seems to better compensate the effect of the binning than the broadening.

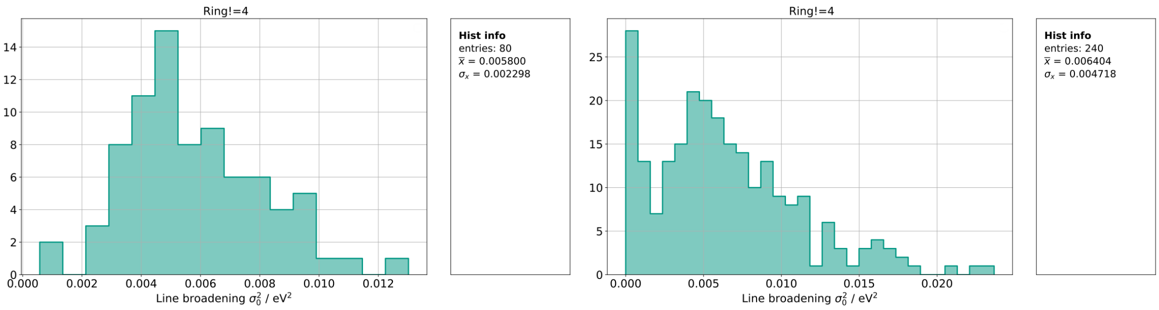

Figure 5.25: Comparison of the distributions of σ^2 for the ramping measurement at 30 mV/s with a binning with of 30 mV (left) and 60 mV (right). The data was obtained at the 1 G magnetic field setting in KNM4. $\bar{x}$ and σ_x represent the unweighted mean value and standard deviation, respectively. The weighted averages can be found in table 5.5. The histogram for the 60 mV binning has 3 times more entries than the one for the 30 mV binning, since only 10 instead of 30 runs were stacked for each fit due to technical challenges. Thus, the separate fits had 3 times less statistics.

Table 5.6: Comparison of B_{ana}/G for different binning widths b. The data was obtained in the 1 G magnetic field setting for different ramping velocities in KNM4. For comparison the measurement at 30 mV/s, which equals a 30 mV binning, was additionally analysed with a 60 mV and 90 mV binning.

Binning b	Ramp at 30 mV/s	Ramp at b/s
30 mV	0.960 ± 0.006	0.960 ± 0.006
60 mV	0.971 ± 0.005	1.038 ± 0.006
90 mV	0.969 ± 0.005	1.131 ± 0.006

The values of the N_2 line position E_{N2} can be compared in the same way as σ^2 and are presented in table 5.7. There is again no clear relation to the bin width visible. It is unclear how the values can be interpreted and how effects like the binning should influence the line position. A dependency on the binning could not be confirmed. The values might furthermore be influenced by an error in the analysis.

Table 5.7: Comparison of $\overline{E_{N2}}$/meV for different binning widths b. $\overline{E_{N2}}$ denotes $E_{N2} - 32\,136$ eV. The data was obtained in the 1 G magnetic field setting for different ramping velocities in KNM4. For comparison the measurement at 30 mV/s, which equals a 30 mV binning, was additionally analysed with a 60 mV and 90 mV binning.

Binning b	Ramp at 30 mV/s	Ramp at b/s
30 mV	$589.7^{+2.1}_{-2.1}$	$589.7^{+2.1}_{-2.1}$
60 mV	$575.9^{+1.7}_{-1.8}$	$553.9^{+2.0}_{-2.4}$
90 mV	$577.0^{+1.7}_{-1.8}$	$682.1^{+2.1}_{-2.7}$

5.3.5 Conclusion

Different measurement modes, settings and analysing strategies have been compared in this section. As a result for further measurements, the following configurations are suggested:

- When averaging values with corresponding asymmetric Minos errors one should use an asymmetric weighted average, as discussed in subsection 3.2.2.
- For the broadening of the N_{23} lines it is advised to manually set a limit at zero for the fit, since using the mathematical model extension below the limit does not show a significant improvement of the normalised χ^2 and does not result in a Gaussian distribution of σ^2. While a tuning of the model extension might improve the obtainable distribution, it can be doubted that the extension to the negative region is even possible due to the next to vanishing width of the N_{23} lines. When using the limit, calculating a weighted average becomes inaccurate. For the future it is recommended to use Monte Carlo simulations of the distribution of the values to obtain the best estimate or to use a common broadening for several pixels already in the fit. The latter allows to obtain the observables with increased statistics directly without averaging.
- For the magnetic field setting 2.7 G is recommended since it gives the larger statistic since all rings can be used. Furthermore, the 1 G setting might be effected by collision effects of the electrons with the vessel making a stricter pixel cut necessary. However, this would further decrease the statistics. Additionally, it is more sensitive to inner pixel field inhomogeneities and to the alignment. The latter might be useful for measurements testing the alignment. For all other purposes the 1 G setting shows no notable advantages.
- Regarding the measurement modes, the MTD mode is still the most reliable and best understood mode. Nevertheless, the MTD IE mode might be used if the inner electrode voltage dependent potential depression can be precisely determined. This would allow to speed up the measurement process by a few seconds per measurement point since it reduces the time for setting each retarding voltage. In addition to the effect of the inner electrode voltage dependent potential depression, the ramping mode suffers from serious timing problems.
- There might be other systematics effects besides the binning which have not been understood. Therefore, it is advised to not use the ramping mode without further investigations.

5.4 Optimum Rear Wall Voltage in KNM5

In order to perform high sensitivity N line measurements it is essential to determine the optimal rear wall voltage setpoint. Using this optimal setpoint for the RW voltage minimises inhomogeneities of the source potential, as discussed in section 4.2. This is important to avoid systematic shifts of the neutrino mass.

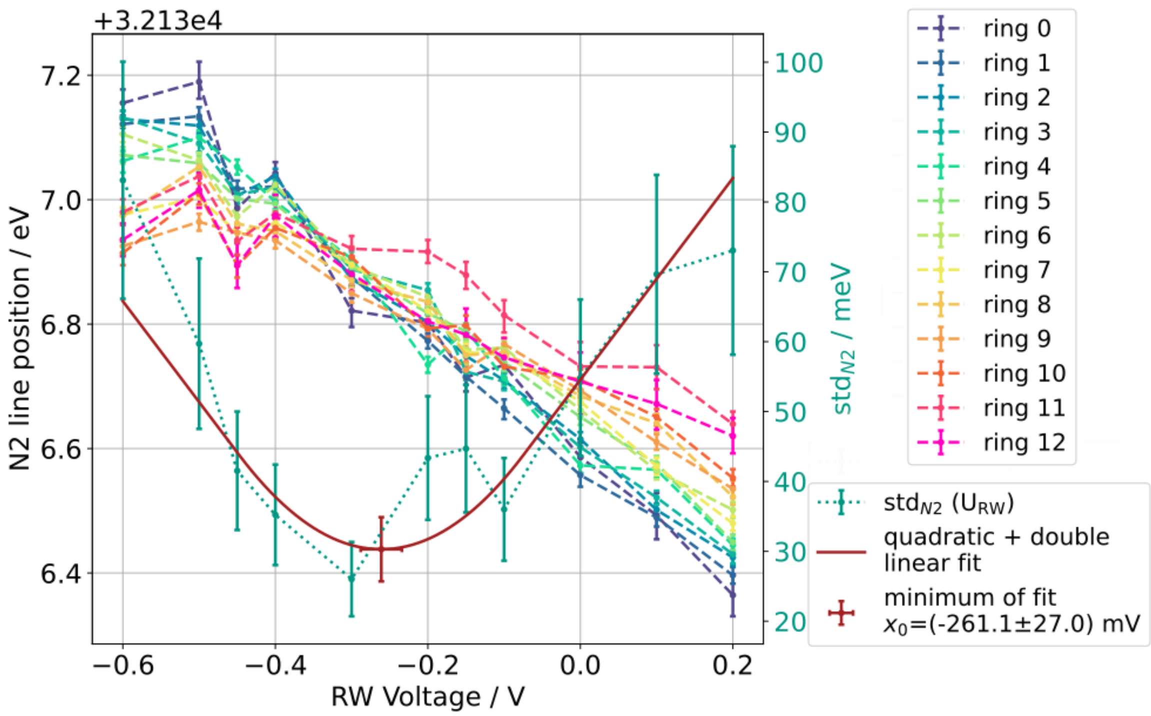

Figure 5.26: Rear wall dependent ringwise N_2 line positions. The data results from the KNM5 krypton measurements at the 2.7 G magnetic field setting. The standard deviation of the N_2 line position per RW voltage is fitted with a quadratic and double linear fit. Its minimum gives the optimal RW voltage setpoint.

The optimal RW voltage setpoint is obtained by measuring the krypton line positions at different RW voltages. The optimal RW voltage is defined as the RW voltage of minimal standard deviation of the line positions over the rings, since at that point the radial dependencies of the source potential are minimised. Here, the line position of the N_2 line is analysed. The result of the analysis for RW voltages between -0.6 V and 0.2 V is shown in figure 5.26. In this interval the electric potential determining the line position is coupled to the RW voltage for the inner rings, with decreasing coupling for the outer rings. To obtain the point of minimal radial dependency, the standard deviations of the line positions per RW voltage are shown and fitted by a quadratic and double linear function. The linear relation of the function is chosen based on the expected linear increase of the distances between the lines away from the minimum. The quadratic relation is needed to model the minimum [Ost20]. Using this function, the minimum giving the optimal RW voltage setpoint is found at (-261.1 ± 27.0) mV. The L_3 line position is equally suited for the determination of the optimal RW voltage. Therefore, as a cross-check the L_3 line position was analysed dependent on the RW voltage, suggesting an optimal RW voltage setpoint of -300 mV [Gup21]. After considerations, an optimal RW voltage setpoint of -300 mV was chosen.

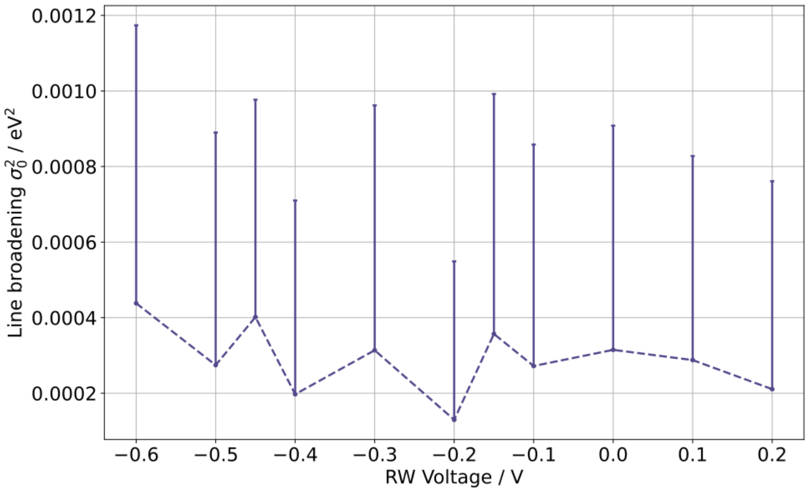

Figure 5.27: Line broadening σ^2 for various rear wall voltage setpoints. The data results from the KNM5 krypton measurements at the 2.7 G magnetic field setting. Since σ^2 is fitted with a lower limit the average is weighted symmetrically by the upper uncertainties. To reflect the asymmetry of the uncertainties, the lower uncertainties were calculated separately. ϵ denotes a lower error close to zero. The symmetric weighted average results to $0.269^{+0.171}_{-\epsilon} 10^{-3}\,\mathrm{eV}^2$.

Additionally, the RW voltage dependency of the broadening σ^2 was reviewed, as shown in figure 5.27. No clear RW voltage dependency of σ^2 could be found due to uncertainties being at the same order of magnitude as the obtained values for the broadening. The weighted average is obtained to be $0.269^{+0.171}_{-\epsilon} 10^{-3}\,\mathrm{eV}^2$. This value is not corrected by the contribution of the Doppler effect. The correction would shift the value into the negative range. As in the previous sections, there are obvious problems with fitting and averaging the pixelwise broadening. Due to the low statistics per fit more results end up in the set limit. The uncertainties of those results are often underestimated and thus distort the weighted average. Furthermore, the natural line width was most probably estimated too large. Both problems contribute to a too small broadening. In order to check for a RW dependency of σ^2, a reanalysis using a smaller natural line width and a common broadening per ring would be necessary.

5.5 Analysis of KNM5 *N* Line Measurements

In the KNM5 krypton campaign high sensitivity N line measurements were conducted. These measurements aim for a best case scenario at a sensitivity for σ of 10 meV and for Δ_{10} of 15 mV in order to reach a sensitivity of 0.017 eV^2 on the shift of the squared neutrino mass [FML+21]. The energy interval of the measurement includes the N_{23} lines, as well as their energy loss region and the N_1 and satellite lines. The spectrum is measured using the MTD measurement mode in the 2.7 G setting. The measurement time per run amounts to 2.5 h, while using the measurement time distribution listed

Table 5.8: Results of the high sensitivity N line measurements in KNM5. Listed are the weighted averages over rings 0 to 9. The background rate c_{Bg} and the broadening σ^2 are fitted with a lower limit. $\overline{E_{N2}}$ symbolises $E_{N2} - 32\,136\,\mathrm{eV}$. The values of the plasma parameters are corrected based on the results of the sensitivity studies in subsection 5.2.2. (*) refers to a pixelwise analysis which obtains a common broadening per ring for all rings. Unlike all other analyses in this thesis a natural line width of 0 eV was used.

Parameter	Value	Corrected
χ^2/N_{DOF}	0.96	
$c_{\mathrm{Bg}}/\mathrm{cps}$	0.506 ± 0.004	
$\rho d/\mathrm{m}^{-2}$	$3.11\,10^{21} \pm 6.86\,10^{18}$	
$B_{\mathrm{ana}}/\mathrm{G}$	2.625 ± 0.003	
$\sigma^2/10^{-3}\,\mathrm{eV}^2$	$1.61^{+0.24}_{-\epsilon}$	$-1.31^{+0.24}_{-\epsilon}$
$\overline{E_{N2}}/\mathrm{meV}$	$999.7^{+1.6}_{-1.7}$	$999.7^{+1.6}_{-1.7}$
Δ_{10}/mV	$29.15^{+10.40}_{-11.04}$	$2.46^{+10.40}_{-11.04}$
χ^2/N_{DOF} (*)	0.95	
$\sigma^2/10^{-3}\,\mathrm{eV}^2$ (*)	$4.01^{+0.26}_{-0.24}$	$1.10^{+0.26}_{-0.24}$

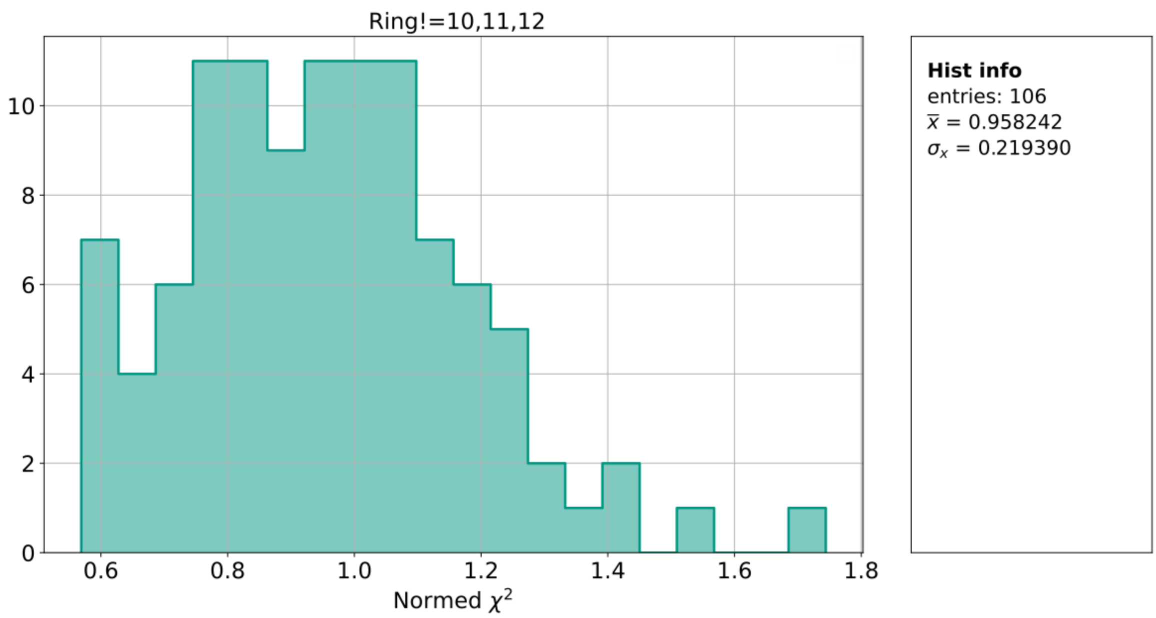

Figure 5.28: Distribution of the normed χ^2 values of the high sensitivity N line measurements in KNM5 for rings 0 to 9. $\bar{x}$ and σ_x denote the average and the variance of the distribution, respectively.

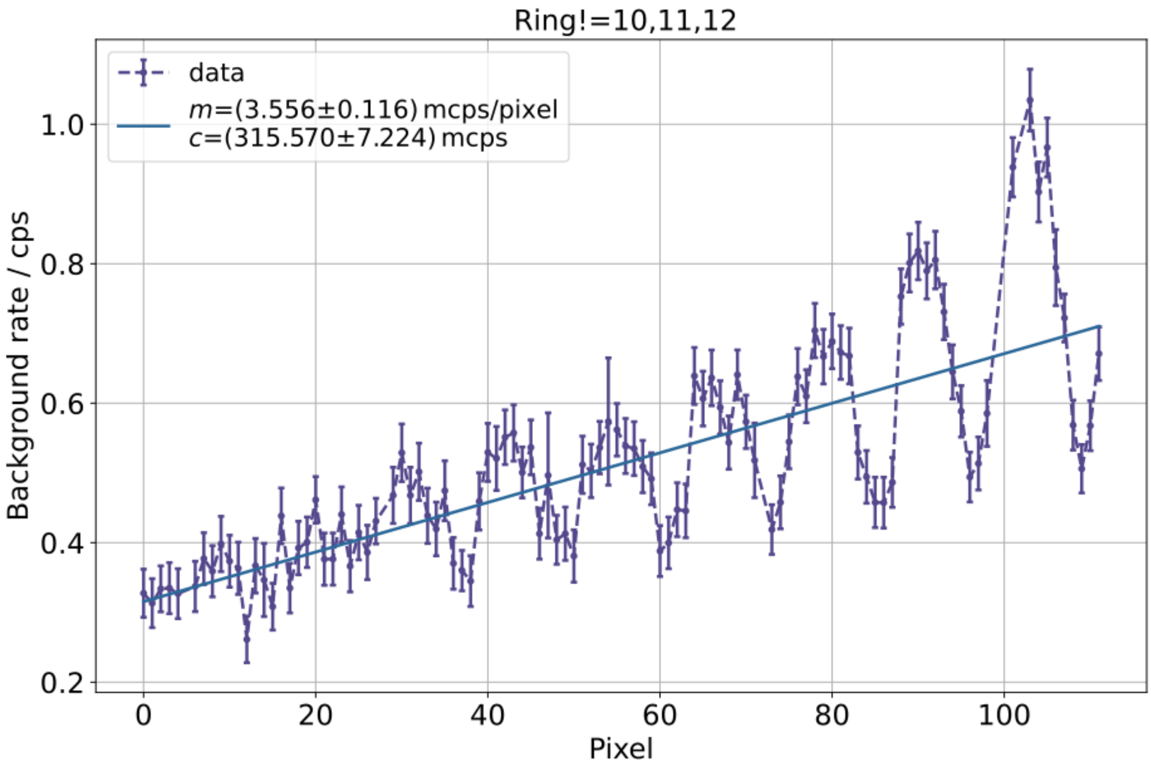

Figure 5.29: Pixelwise background rate of the high sensitivity *N* line measurements in KNM5 for rings 0 to 9. The results are fitted linearly with slope m and offset c. The weighted average amounts to (0.506 ± 0.004) cps. The results are shown at their pixelwise positions on the FPD in figure 5.30.

in section A.1. The analysed 79 runs are listed by their run numbers in section A.2, leading to a total measurement time of 197.5 h included in the analysis.

Since only slight drifts were observed during the measurement causing an additional broadening at the order of 1 mV, all runs are stacked together. As in the previous analysis, the model and fit parameters suggested by the sensitivity studies were used, excluding the influence of the Doppler effect and the detailed transmission for single scattered electrons. Since the sensitivity studies simulate the measurement conditions for the high sensitivity N line measurements in KNM5, the results can be used to correct the obtained values by the shift of the unaccounted systematics. However, for a final analysis, the sensitivity studies should be repeated using the real measurement data. Furthermore, the measurement and analysing settings recommended by section 5.3 are applied and the optimal rear wall voltage setpoint obtained in section 5.4 is used. The results of a selection of parameters are listen in table 5.8.

The average of the normalised χ^2 of the fit results is 0.96. The corresponding distribution of the nχ^2 values is shown in figure 5.28. It shows no unexpected features.

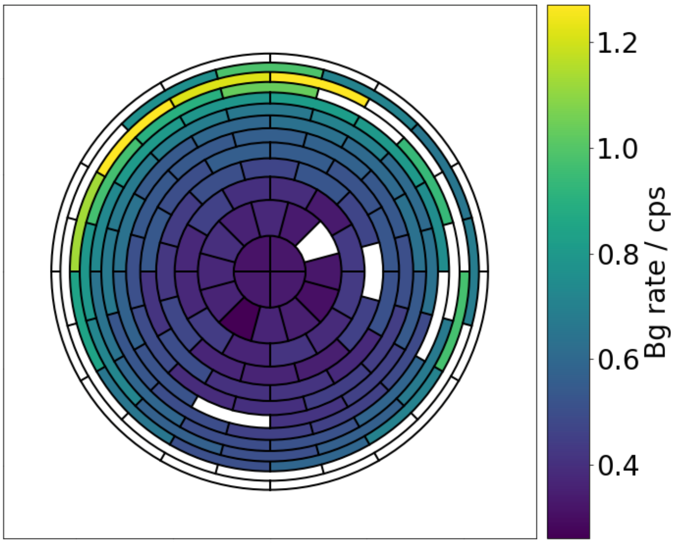

Figure 5.30: Pixelwise background rate of the high sensitivity *N* line measurements in KNM5 mapped onto the FPD. The values for the upper left pixels are significantly increased compared to the lower right values of the same ring. This might be an effect of the misalignment. The pixelwise values with uncertainties are shown in figure 5.29.

The width of the χ^2-distribution is $\sqrt{2/N_{\mathrm{DOF}}} = 0.22$, with N_{DOF} being the number of degrees of freedom in the fit. The calculated width seems to match the distribution. Furthermore, the uncertainty on the average is assumed to scale with $1/\sqrt{N_{\mathrm{entries}}} = 0.1$. Here, N_{entries} denotes the number of entries in the histogram. Thus, the averaged $\mathrm{n}\chi^2$ agrees with 1 within the uncertainties and therefore the fit parameters are able to describe the data well.
Considering the pixelwise background rate c_{Bg}, shown in figure 5.29, a ring-dependent oscillation pattern with increasing amplitude and offset can be found. The radial increase of the structure amounts to (3.556 ± 0.116) mcps/pixel. When mapping the pixelwise values onto the FPD, the radially increasing rate of the background becomes visible, as shown in figure 5.30. This dependency has been observed in former analysis and has been studied by [Hin18]. It is assumed that the background rate, which is 30 times higher than estimated in [AAB$^+$04], results from Rydberg states with a short lifetime and a low energy state which spontaneously decay close to the vessel walls. The increase of the rate towards the outer rings origins from this background coming from the vessel walls. Additionally, a polar asymmetry can be found in figure 5.30, which explains the oscillating pattern in figure 5.29. The upper left pixels of the detector exhibit an increased background rate compared to the other pixels of the same ring, while the lower right pixels show a decreased background rate in comparison. This observation results most likely from misalignment effects. The weighted average for c_{Bg} results to (0.506 ± 0.004) cps, which is close to the predicted 0.540 cps used for the sensitivity studies in section 5.2. This is relevant since the sensitivity studies are used to correct the obtained values of the plasma parameters for systematic shifts.

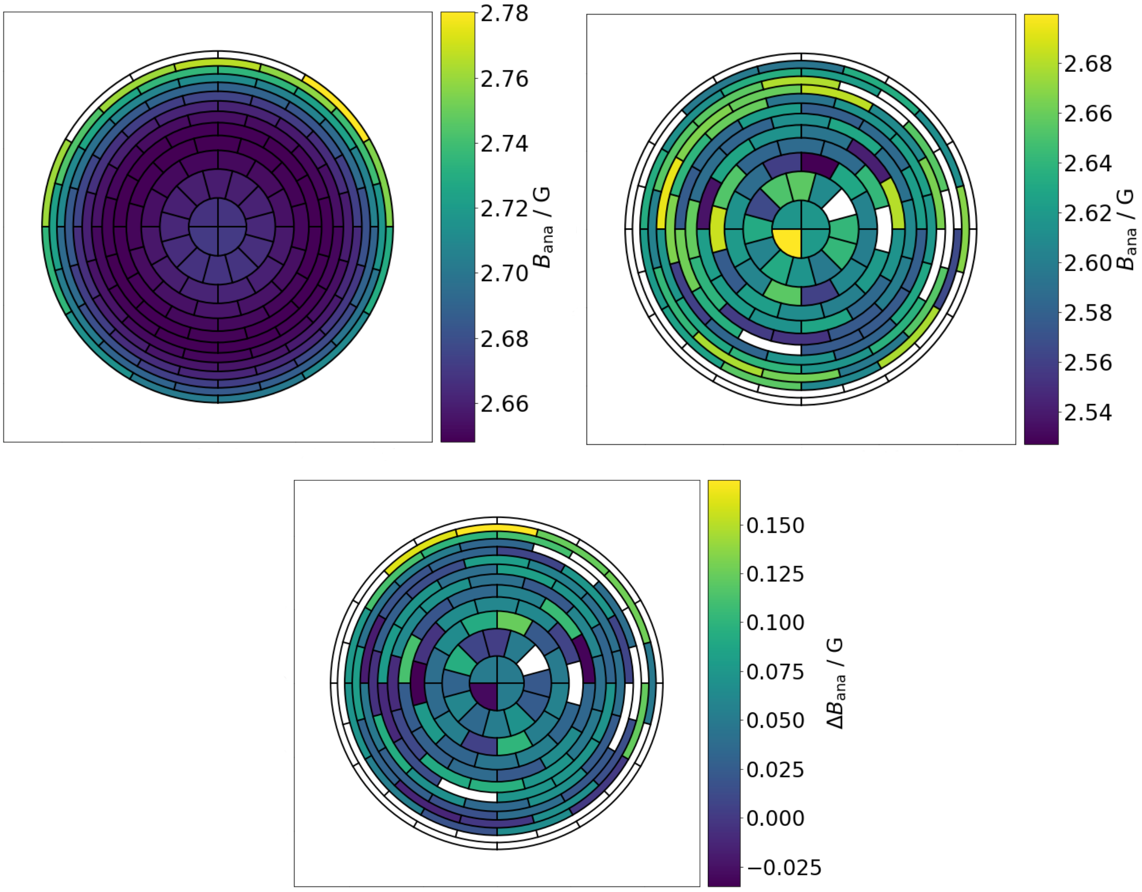

Figure 5.31: Pixelwise values of B_{ana} of the high sensitivity N line measurements in KNM5, mapped onto the FPD (upper right) and compared with the simulated values in the period summary file (upper left). The lower FPD plot shows the pixelwise difference between the values for B_{ana} of the simulation and the fit: $\Delta B_{\mathrm{ana}} = B_{\mathrm{ana,simulation}} - B_{\mathrm{ana,fit}}$.

Furthermore, the column density ρd was fitted, with an expected value of $3.82 \times 10^{21}\,\mathrm{m}^{-2}$ (76 % CD). In comparison, an average of only $(3.11\,10^{21} \pm 6.86\,10^{18})\ \mathrm{m}^{-2}$ (62 % CD) was obtained in the analysis, which is 18 % smaller than expected. This discrepancy is not yet fully understood. Since no problems with the measurement could be found, it might result from an imprecise modelling. The value of $\rho d \sigma$, being the product of the column density with the inelastic scattering cross section, can be determined by Egun measurements using 18 keV electrons. Since the Egun cannot reach the energy scale of the krypton N lines, the inelastic scattering cross section is extrapolated for energies of 30 keV based on [Liu73]. Nevertheless, for the N lines, an extrapolation for energies up to 32 keV is needed. However, the theoretical uncertainty of the cross section is too small to explain the observed discrepancy. Furthermore, the slicing of the source might have an influence on the column density. It was observed that not slicing the source at all in the analysis leads to smaller values of the column density. Consequently, until the problems are resolved it is recommended to add the column

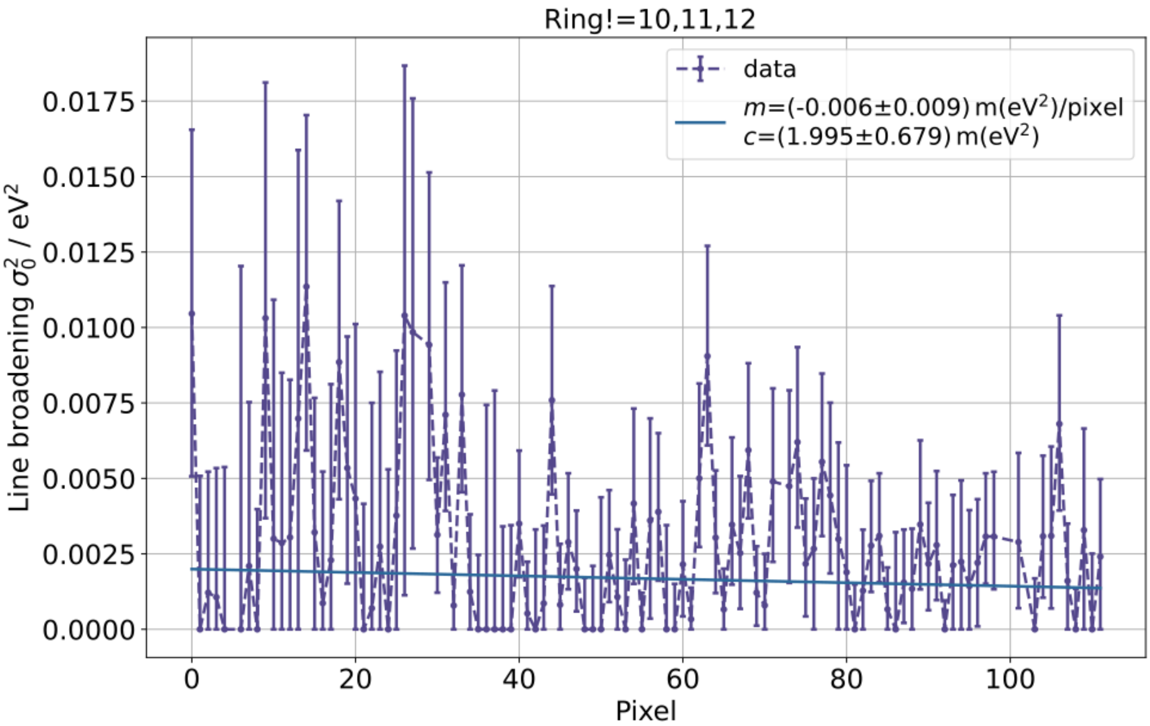

Figure 5.32: Pixelwise broadening σ^2 of the high sensitivity N line measurements in KNM5 for rings 0 to 9. The results are fitted linearly with slope m and offset c using the upper uncertainties. The weighted average amounts to $\left(1.61^{+0.24}_{-\epsilon}\right)\ 10^{-3}\,\mathrm{eV}^2$. Since σ^2 is fitted with a lower limit only the upper uncertainties are used to symmetrically weigh the average. The lower uncertainty is calculated separately, with ϵ denoting a lower uncertainty close to zero. The distribution of the values is shown in figure 5.33.

density as a free fit parameter to avoid bias, although the value from the external calibration would decrease the uncertainties on σ^2, E_{N2} and Δ_{10} , as shown in subsection 5.2.1.

Since the magnetic field strength B_{ana} is fitted as a free parameter, the corresponding pixelwise estimates can be compared with the simulation, as shown in figure 5.31. It is visible that the simulations predicts a radial dependent magnetic field strength which first slightly decreases and then increases towards the outer rings. Also, the alignment center is slightly shifted towards the lower right side. The estimates from the fit show show no obvious pattern. The difference between the simulated and fitted values for B_{ana} shows, that a majority of the fitted pixelwise values exhibit a roughly 50 mG smaller magnetic field strength than predicted by the simulation. Comparisons between simulations and magnetic field sensors in the experiment lead to the conclusion that a 50 mG to 60 mG lower magnetic field for the fit result than currently simulated can be expected for the 2.7 G setting [Blo22]. Therefore, the obtained difference is of the correct order of magnitude. Finally, an averaged magnetic field strength of (2.625 ± 0.003) G has been obtained.

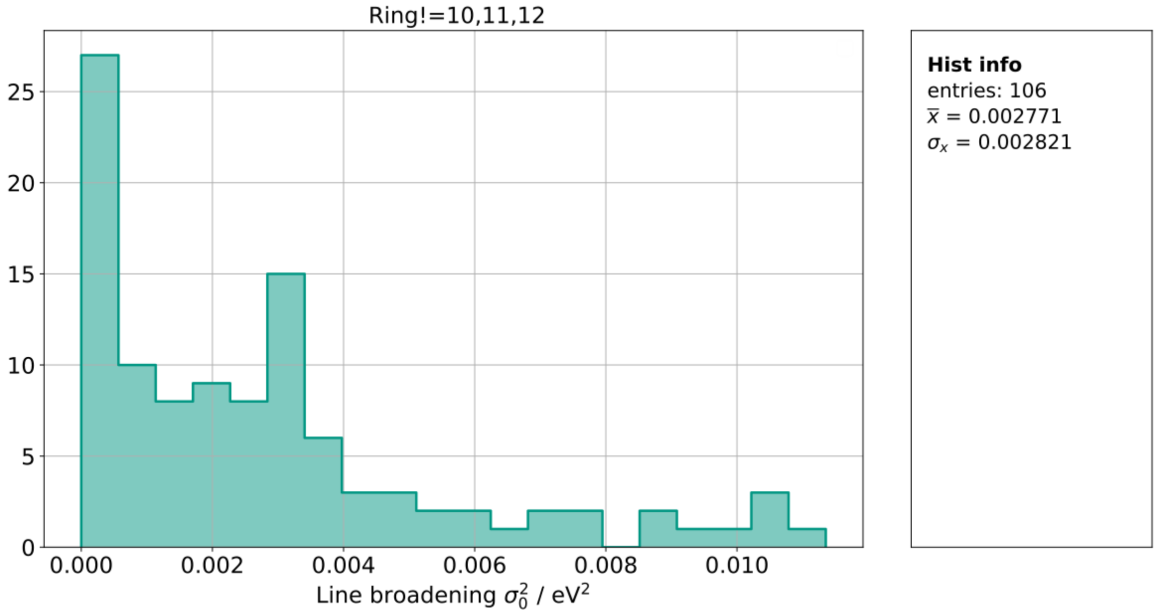

Figure 5.33: Distribution of the σ^2 values of the high sensitivity N line measurements in KNM5 for rings 0 to 9. $\bar{x}$ and σ_x denote the unweighted average and the variance of the distribution, respectively. The weighted average amounts to $\left(1.61^{+0.24}_{-\epsilon}\right)\ 10^{-3}\,\mathrm{eV}^2$. Since σ^2 is fitted with a lower limit only the upper uncertainties are used to symmetrically weigh the average. The lower uncertainty is calculated separately, with ϵ denoting a lower uncertainty close to zero. The pixelwise values are shown in figure 5.32.

The high precision N line measurements in KNM5 were conducted to precisely determine the plasma parameters σ^2, E_{N2} and Δ_{10}. Their results are presented in the following.
For the broadening σ^2 a weighted average of $\left(1.61^{+0.24}_{-\epsilon}\right)\ 10^{-3}\,\mathrm{eV}^2$ was obtained. The pixelwise values with their corresponding uncertainties are shown in figure 5.32. It can be seen, that a significant part of the obtained values lie in the lower limit and that some of them have comparably small upper uncertainties. The distribution of the pixelwise values visible in figure 5.33 shows that around a quarter of all obtained results exhibit a value close to the limit. Therefore, it must be assumed that the weighted average might be shifted to smaller values due to those results in the limit which also show a small upper uncertainty. Therefore, a Monte Carlo study is needed to cross-check the obtained value for σ^2. Additionally, the broadening must be corrected by the not included but relevant systematic shifts. The sensitivity studies in subsection 5.2.2 demonstrated, that the effects of the synchrotron radiation, the Doppler effect and the detailed transmission for single scattered electrons need to be included in the analysis. The synchrotron radiation and the detailed transmission for unscattered electrons are already included in the fit model. Since the studies have shown that the detailed transmissions for un- and single scattered electrons give the same shift of the broadening, only the Doppler effect needs to be subtracted. The Doppler effect shifts σ^2 by $2.92 \times 10^{-3}\,\mathrm{eV}^2$, leading to a corrected value of $-1.31 \times 10^{-3}\,\mathrm{eV}^2$. That the

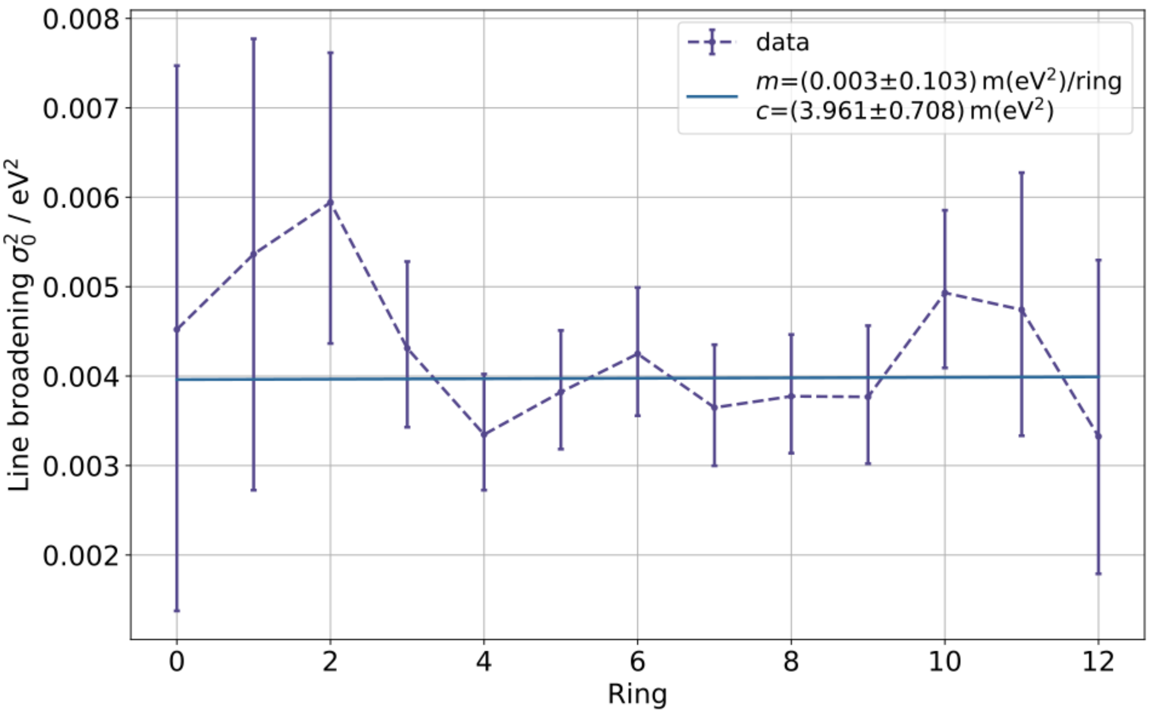

Figure 5.34: Ringwise common broadening σ^2 of the high sensitivity N line measurements in KNM5. The results are fitted linearly with slope m and offset c using the upper uncertainties. The weighted average amounts to $\left(4.01^{+0.26}_{-0.24}\right)\ 10^{-3}\,\mathrm{eV}^2$. The values were obtained by a pixelwise analysis using a common broadening per ring. Unlike all other analyses in this thesis a natural line width of 0 eV was used.

final estimate is negative is probably caused by the method of obtaining the weighted average from the fit results. Another reason could lie in the chosen value of the natural line width and its strong correlation with the broadening. Only a theoretical upper limit of 30 meV exists for the natural line width of the N_{23} lines. Here, a natural line width of 10 meV was assumed. If the natural line width were close to zero this would significantly increase the obtained broadening due to their correlation. An indication that a too large natural line width was used was found in subsection 5.3.1.
In a pixelwise analysis using a ringwise common broadening an uncorrected value for σ^2 of $\left(4.01^{+0.26}_{-0.24}\right)\ 10^{-3}\,\mathrm{eV}^2$ was found. Here, a natural line width of 0 eV was used, since the analyses in subsection 5.3.1 suggested a natural line width of 10 meV being to large. Furthermore, in an analysis with a free natural line width by M. Machatschek a value of $\Gamma = 0\,\mathrm{eV}$ was obtained. This shows, that using a common broadening in the analysis can solve the problems obtained for the pure pixelwise fits and the averaging of their results. Corrected for the Doppler broadening the value amounts to $\left(1.10^{+0.26}_{-0.24}\right)\ 10^{-3}\,\mathrm{eV}^2$. Thus, the unsquared broadening σ equals 33 meV, which is on the scale of the broadening determined by simulation of 7 meV [Kuc16, Mac21a]. The discrepancy between the values is plausible, since the simulation uses a simplified model of the experiment.

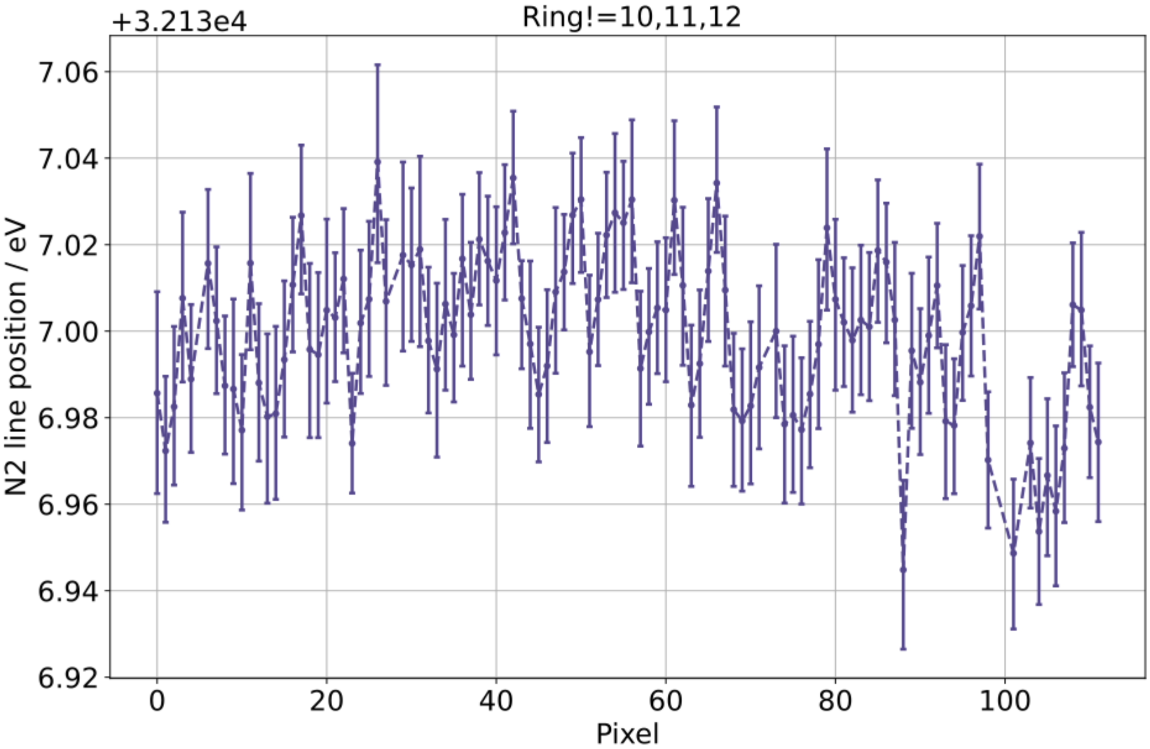

Figure 5.35: Pixelwise N_2 line position E_{N2} of the high sensitivity N line measurements in KNM5 for ring 0 to 9. The asymmetric weighted mean amounts to $\left(32\,137.000^{+0.002}_{-0.002}\right)$ eV.

The obtained estimate for σ^2 allows to predict an upper limit for the Eloss shift, using the inequality [Mac21a]

$$|\Delta_{10}| < 0.74\,\sigma\,. \tag{5.5}$$

Thus, the Eloss shift Δ_{10} must be less than 24.54 mV.
Regarding the sensitivity for σ^2, a value of $0.39 \times 10^{-3}\,\mathrm{eV}^2$ had been predicted by the sensitivity studies in subsection 5.2.1 for a measurement time of 14 d, scaled for the given number of pixels. The fit result using the common broadening gives even a slightly higher sensitivity of $0.25 \times 10^{-3}\,\mathrm{eV}^2$. This might be due to the fixed N_3 line width in the analysis compared to the study. The goal of the measurement for the best case scenario was a sensitivity of $0.1 \times 10^{-3}\,\mathrm{eV}^2$, which could not be reached. However, the obtained sensitivity is significantly larger than the lowest presumed sensitivity of $0.6 \times 10^{-3}\,\mathrm{eV}^2$ [FML+21]. Nevertheless, for the final analysis the sensitivity studies need to be repeated using the real measurement data.
The N_2 line position E_{N2} is obtained as $\left(32\,137.000^{+0.002}_{-0.002}\right)$ eV. The pixelwise results, visible in figure 5.35, show slightly lower line positions for the inner and outer rings compared to the middle ones. The difference is of the order of 40 meV. This pattern has been observed for previous measurements and is assumed to result from the shape of the work functions of the beam tube and the rear wall. It must be noted, that the

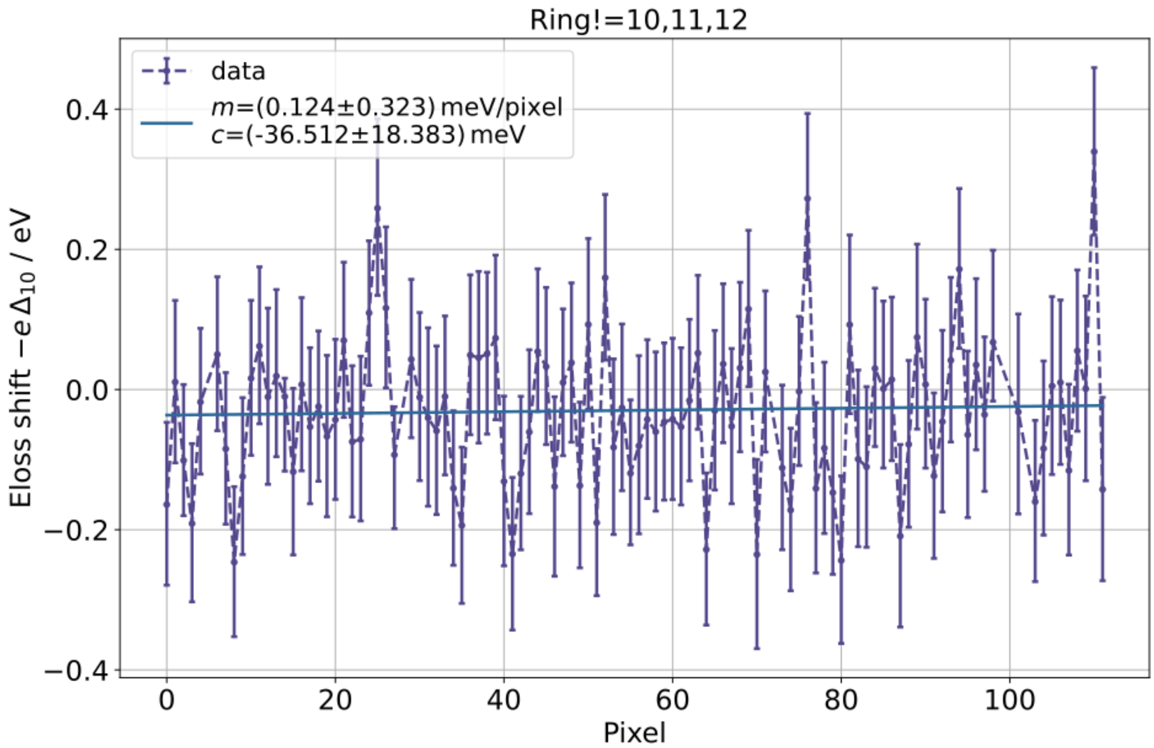

Figure 5.36: Pixelwise Eloss shift Δ_{10} of the high sensitivity N line measurements in KNM5 for rings 0 to 9. The results are fitted linearly with slope m and offset c using the upper uncertainties. The asymmetric weighted mean amounts to $\left(-29.15^{+10.40}_{-11.04}\right)$ meV.

line position includes the average potentials of the KATRIN experiment. The average of the line position does not need to be corrected since all relevant systematic effects are already included in the model. The obtained sensitivity on the line position of 1.653 meV is again higher than predicted, compared to the 2.612 meV sensitivity for 14 d measurement time, scaled for the given number of pixels. However, the influence of the source magnetic field strength is not included in the analysis compared to the study. Thus, the obtained uncertainty in the analysis might be slightly underestimated. Since no problems were found for the N_2 line position, this result shows that the high sensitivity N line measurement were conducted successfully.
As a result for the Eloss shift Δ_{10} the weighted average of $\left(29.15^{+10.40}_{-11.04}\right)$ mV was found. The pixelwise fit results, presented in figure 5.36, do not show a radial dependency. Based on the sensitivity studies, this value must be corrected with the difference of the shifts given by the detailed transmissions for single and un-scattered electrons. This results to a corrected value of the Eloss shift Δ_{10} of 2.46 mV. Since the Eloss function for the energy range of the N lines is still unknown, it is not possible to correct for this systematic. Nevertheless, it is assumed based on the sensitivity studies, that an inaccurate Eloss function could cause a shift at the order of −10 mV. The corrected estimate for Δ_{10} is in agreement with the upper limit of 24.54 mV obtained from the broadening using equation 5.5. In KNM2 a value of the Eloss shift of 98 mV had

been obtained, not including the detailed transmission [Mac21a]. When correcting the value based on the sensitivity studies one finds an Eloss shift of 28.78 mV. It is unclear, why the value obtained in KNM2 is larger than the one from KNM5. Possibly, the sensitivity studies for the KNM5 measurement settings do not apply to the data obtained in KNM2. The KNM2 measurements were conducted with only a 30 % column density which is more than 2 times smaller than in KNM5 and thus might influence the contribution of the detailed transmission. Furthermore, the L_3 line which is influenced by a background slope was used in KNM2. This influence might not have been fully understood and therefore cause an effect on the estimate. Additionally, the effect of the energy dependent cross section was not covered by the systematic studies but might cause a shift of the estimate.

The high-sensitivity N line measurements were designed to reach a sensitivity of 15 mV on the Eloss shift in order to obtain a sensitivity of $0.017\,\mathrm{eV}^2$ on the shift of the squared neutrino mass. From the sensitivity studies the sensitivity on Δ_{10} was predicted to be at 7.98 mV for a measurement time of 14 d, scaled for the given number of pixels. The fit result gives a sensitivity of 10.72 mV, which is slightly smaller than predicted by the sensitivity studies. This is probably due to the analysed data only covering around 8 d of measurement time instead of 14 d. Nevertheless, the sensitivity can even be increased by additionally analysing data taken at the beginning of KNM5 under slightly different measurement conditions.

Based on the obtained values for σ^2 and Δ_{10} the uncertainty on the shift of the squared neutrino mass can be obtained, using

$$\delta\Delta m_\nu^2(\Delta_{10}, \sigma_0) = \sqrt{(\epsilon_1 \delta\Delta_{10})^2 + (4\sigma_0\delta\sigma_0)^2}\,. \tag{5.6}$$

With factor $\epsilon_1 \approx 1170\,\mathrm{meV}$ this results to a sensitivity of $\delta\Delta m_\nu^2(\Delta_{10}, \sigma_0) = 0.0127\,\mathrm{eV}^2$, which is better than the aimed at sensitivity of $0.017\,\mathrm{eV}^2$.

Concluding, the derived measurement and analysis strategy was successfully applied for the high-sensitivity N line measurements in KNM5. Thereby, the aspired sensitivity on the Eloss shift Δ_{10} was reached. Furthermore, all plasma parameters could be determined with a high sensitivity. The analysis of the additional helium measurements will provide a better determination of the line parameters which further improve the sensitivity on σ^2, E_{N2} and Δ_{10}. A Monte Carlo study based on the actual measurement data will be able to determine systematic shifts and uncertainties with more precision. A final analysis using a common broadening as well as all relevant parameters will then result in a reliable best estimate for the neutrino mass analysis.

Chapter 6

Summary and Outlook

Neutrino oscillation experiments have proven that neutrinos have a mass. Determining this mass will pave the way to understanding physics beyond the Standard Model. To achieve this goal, different measurement approaches are currently being used, giving different effective neutrino masses.

The current leading upper constraint on the electron antineutrino mass from direct kinetic measurements comes from the KATRIN experiment with $m_{\overline{\nu_e}} < 1.1\,\mathrm{eV/c^2}$ (90 % C.L.) [AAA+19]. The KATRIN experiment directly measures the kinematic endpoint of the tritium β-decay using high-precision spectroscopy of the generated electrons. In order to reach the design sensitivity of down to $0.2\,\mathrm{eV/c^2}$ (90 % C.L.) [AAB+04], understanding and reducing systematic effects on the neutrino mass measurement is essential. Amongst others, the systematic influence of the inhomogeneous source potential on the neutrino mass needs to be quantified. This is done by ^{83m}Kr calibration measurements.

In the thesis at hand, various systematic effects concerning the ^{83m}Kr measurements have been studied, leading to a recommended measurement and analysis strategy for the krypton calibration measurements using the N_{23} conversion electron line doublet. The obtained strategy has been successfully applied to the high-sensitivity N line measurements conducted in the KNM5 KATRIN krypton measurement from the summer of 2021.

In order to quantify model and parameter dependent systematic contributions for the observables of the source potential, namely the broadening σ^2, the N_2 line position E_{N2} and the Eloss shift Δ_{10}, sensitivity studies have been performed using the pull term method. It has been shown that the relative line intensity of the N_{23} lines I_{N3}/I_{N2}, the relative line position of the N_{23} lines ΔE_{N23}, the natural line width of the N_3 line Γ_{N3} as well as the magnetic field strength in the analysing plane B_{ana} and in the source B_{src} significantly contribute to the systematic uncertainty of σ^2. Their individual effect on σ^2 is of the order of several $10^{-4}\,\mathrm{eV}^2$ for ringwise statistics of 14 d. The uncertainty of the line position E_{N2} is mainly affected by the contributions of I_{N3}/I_{N2}, ΔE_{N23}, B_{ana} and B_{src}, each adding several meV to the uncertainty. Most relevant for the uncertainty of the Eloss shift Δ_{10} in case of low statistics of the measurement is the column density ρd. In this case, knowing ρd can decrease the uncertainty by more than 10 meV. This effect is reduced with increased statistics. Furthermore, the uncertainties on the parameters of the N_1, N_{23} and satellite lines lead to relevant systematic uncertainties on the Eloss shift.

Additionally, it has been studied how a dedicated measurement of the N line properties at the KATRIN experiment can improve the systematic uncertainties of the observables of the source potential. This measurement uses helium instead of tritium as the carrier gas for krypton to ensure a high krypton rate while eliminating the contribution of scattered electrons in the N line region. The corresponding sensitivity studies show a large reduction of the systematic uncertainties on σ^2, E_{N2} and Δ_{10}. Only the systematic contribution of Γ_{N3} for σ^2 is still relevant, since its uncertainty cannot be reduced by the helium measurement due to its correlation with the broadening. Therefore, a more precise theoretical estimation of Γ_{N3} is needed, taking the effect of the neutralisation time in the KATRIN source on the lifetime of the krypton state into account.

The systematic shifts of the source potential's observables caused by an oversimplified modelling of the ^{83m}Kr spectrum were quantified in dedicated studies. They show that the synchrotron radiation, detailed transmission for unscattered electrons, and Doppler effect cause significant shifts of σ^2. For E_{N2}, only the synchrotron radiation and the detailed transmission for unscattered electrons need to be considered. The mean value of Δ_{10} is shifted by the synchrotron radiation, the detailed transmission for single scattered electrons, and by a possibly imprecise Eloss model. The effect of the Eloss model can only be assumed since the correct Eloss function for electrons in the 32 keV energy region is unknown.

Overall, the parameters I_{N3}/I_{N2}, ΔE_{N23}, Γ_{N3}, B_{ana}, B_{src} and ρd should be included in the analysis to minimise the systematic uncertainty on the observables of the source potential. In this thesis, Γ_{N3} and B_{src} were not used to improve the fitting performance and because their contributions are significant but small compared to the others. Regarding the modelling, the synchrotron radiation and the detailed transmission for unscattered electrons are used. The obtained estimates of the source potential are corrected by the shifts caused by the Doppler effect and the detailed transmission for single scattered electrons if needed. This procedure significantly reduces the complexity of the model and therefore the calculation time.

Furthermore, different measurement modes and analysing strategies were compared to study systematic effects and find an optimal measurement and analysing strategy.

Since the N_{23} lines show an intrinsic line width close to zero, an analysing strategy needed to be developed, which prevents unphysical results in the negative region. Different analyses using an extension of the physical model towards the unphysical region and setting limits to prevent fluctuations into the unphysical region were tested.

It was found that the used model extension does not result in a Gaussian distribution of the estimates and therefore is not useful for the analysis.
Therefore, limits were set on both parameters. However, this method causes problems when calculating the weighted mean of the resulting values. A significant part of the results may end up in the limit, impairing the resulting average. A solution would be to increase the statistics on the broadening by using one common broadening for multiple pixels or determining the best estimate by using Monte Carlo simulations.

Next, the magnetic field settings of 1 G and 2.7 G in the analysing plane of the spectrometer have been compared, as well as the three different measurement modes MTD, MTD IE and ramping mode and different ramping velocities of the ramping mode. It is concluded that the 2.7 G magnetic field setting provides a higher statistic compared to the 1 G setting since almost all rings of the detector can be used. Additionally, it is less sensitive to the correct alignment and to intra pixel field inhomogeneities. Regarding the measurement modes, the MTD mode is the most reliable since it does not introduce additional systematic effects compared to the other modes and is already well understood. The MTD IE mode comes with the systematic effect of an inner electrode voltage dependent potential depression, which rescales the energy axis of the spectrum. If the scale factor can be precisely determined, this mode would be able to significantly speed up the measurement process by a few seconds per measurement point due to a quicker setting of the retarding voltages. Apart from the inner electrode voltage dependent potential depression, the ramping mode suffers from substantial timing problems. Therefore, it is not a viable option as a new measurement mode, independent of the used ramping velocity.

In order to prepare for the high-sensitivity N line measurements in KNM5, rear wall voltage dependent N line measurements were performed to determine the optimal rear wall voltage setpoint. Cross-checks with other measurement methods led to the decision of setting the rear wall voltage at $-300\,\mathrm{mV}$, which is supported by the analysis at hand.

The high-sensitivity N line measurements in KNM5 were designed to reach a sensitivity of 15 meV on the Eloss shift Δ_{10} in order to limit the associated shift of the squared neutrino mass to $0.017\,\mathrm{eV}^2$. The measurement and analysis follow the acquired strategies. With this a broadening of $(-1.31 \pm 0.24) \times 10^{-3}\,\mathrm{eV}^2$ is obtained after the correction for the Doppler effect. This negative value is due to the calculation of the weighted average, which does not work for values close to a limit and due to a too large assumption of the natural line width. The small natural line width of the N_{23} lines is strongly correlated with the broadening and can therefore not be measured by the KATRIN experiment. Only a theoretical upper limit of 30 meV exists. In this thesis a natural line width of 10 meV was assumed. The analysis in this thesis in combination with analyses by M. Machatschek hint to an even smaller natural line width close to zero. Due to their correlation this would increase the obtained broadening on the order of $0.001\,\mathrm{eV}^2$. To resolve these problems, an analysis using pixelwise values for parameters with an assumed pixel dependency while directly obtaining one common broadening for each ring was performed. Furthermore, the natural line width was reduced to 0 eV. This results in a corrected broadening of $\left(1.10^{+0.26}_{-0.24}\right)\ 10^{-3}\,\mathrm{eV}^2$. The corrected Eloss shift Δ_{10} amounts to 2.5 meV with a corresponding sensitivity of 10.7 meV. This agrees with the upper limit on Δ_{10} of 24.54 mV, which can be estimated based on the broadening using inequality 5.5. However, the estimate of Δ_{10} is not corrected for the shift of the inaccurate Eloss function. This shift is assumed to be at the order of 10 mV but cannot be quantified without a measurement of the Eloss function at the energy region of the N lines. Under the condition that this important systematic must still be accounted for, the aspired sensitivity of the high-sensitivity N line measurements was successfully reached. Based on the obtained values the sensitivity on the shift of the squared neutrino mass could be determined to $\delta\Delta m_\nu^2(\Delta_{10}, \sigma_0) = 0.0127\,\mathrm{eV}^2$, which fulfils the goal of the measurement.

In summary, sensitivity studies and comparisons of different measurement and analysis settings were used to determine and quantify systematic effects and helped to develop an optimised measurement and analysing strategy of the ^{83m}Kr N lines. This strategy was successfully applied for the high-sensitivity N line measurements in KNM5. Nevertheless, further investigation into the following topics are advised:

- The systematic studies do not yet cover the systematic influence of the energy dependent cross section. It should be added and compared to the other model dependent systematic effects.
- The systematic studies determine the influence of the column density ρd on the sensitivity of the plasma parameters based on a model without detailed transmission. As a next step, the uncertainty contribution of ρd can be reassessed using a model including the detailed transmission function.
- In the systematic studies the influence of the magnetic field strengths have been obtained without including the synchrotron radiation. This can lead to higher order effects and may be cross-checked with a model including the synchrotron radiation.
- An investigation on the natural line width of the N_{23} lines will be beneficial in order to reduce its systematic effect on σ^2.
- The simulated magnetic field strength B_{ana} needs to be adapted to the existing measurements, thereby reducing the number of fit parameters and saving computational time. Concerning B_{src}, it might be sufficient to use a more detailed magnetic field model to decrease the systematic effect. Furthermore, the discrepancies regarding the column density must be resolved, which may result from inaccurate modelling.
- To avoid the averaging process, combined fit analyses using a common broadening can be performed.
- To obtain the correct mean value of pixelwise fitted values of σ^2, it is advised to implement a Monte Carlo method to cross-check the result from the combined fit.

By means of these investigations a final analysis using a common broadening as well as all relevant parameters will then result in a reliable best estimate to be used in the neutrino mass analysis.

Appendix A

Additional Values

A.1 MTD Configurations for N Line Measurements and Sensitivity Studies

The following values, given in V, are used as the optimised MTD for the conducted N line measurements and sensitivity studies for the 2.7 G setting. The gray underlayed values correspond to the optimised MTD for the N_{23} line measurements covering a 6 V measurement interval. When adding the green underlayed values to the MTD, the Eloss region of the N lines with N_1 and satellite lines are included in the 21 V measurement interval. For specific investigations in the sensitivity studies the Eloss region can further be expanded by the blue underlayed values. This allowed to study the systematic influence of the Eloss function dependent on the analysing interval.

32114.000000, 32114.333333, 32114.666666, 32115.000000, 32115.333333, 32115.666666, 32116.000000, 32116.333333, 32116.666666, 32117.000000, 32117.333333, 32117.666666, 32118.000000, 32118.333333, 32118.666666, 32119.000000, 32119.333333, 32119.666666, 32120.000000, 32120.679777, 32121.359554, 32122.039331, 32122.719109, 32123.094644, 32123.470180, 32123.845715, 32124.221251, 32124.596786, 32124.972322, 32125.347858, 32125.723393, 32126.098929, 32126.474464, 32126.850000, 32128.480000, 32130.110000, 32131.740000, 32133.370000, 32135.000000, 32135.325277, 32135.650554, 32135.975831, 32136.301109, 32136.435109, 32136.569109, 32136.703109, 32136.837109, 32136.971109, 32137.105109, 32137.239109, 32137.373109, 32137.507109, 32137.738331, 32137.969554, 32138.200777, 32138.432000, 32138.566000, 32138.700000, 32138.834000, 32138.968000, 32139.102000, 32139.236000, 32139.370000, 32139.504000, 32139.638000, 32139.978500, 32140.319000, 32140.659500

A.2 Run Numbers for the different Measurement Settings

The analysed measurements and their corresponding run numbers are listed in table A.1. They are divided by the different measurement settings which have been investigated in this thesis.

Table A.1: Analysed measurements with corresponding run numbers.

Measurement campaign	Covered lines	Magnetic field setting	Measurement mode	Run numbers
KNM4	N_2, N_3	1.0 G	MTD	66899 - 66904
KNM4	N_2, N_3	1.0 G	MTD IE	66881 - 66898
KNM4	N_2, N_3	1.0 G	Ramp, 30 mV/s	66631 - 66690
KNM4	N_2, N_3	1.0 G	Ramp, 60 mV/s	66501 - 66630
KNM4	N_2, N_3	1.0 G	Ramp, 90 mV/s	66711 - 66880
KNM4	N_2, N_3	2.7 G	MTD IE	66975 - 66992
KNM4	N_2, N_3	2.7 G	Ramp, 30 mV/s	66921 - 66974
KNM5	N_2, N_3	2.7 G	MTD, RW Scan	69243 - 69261, 69265 - 69267
KNM5	N_1, N_2, N_3	2.7 G	MTD	69465 - 69468, 69470 - 69473, 69475 - 69476, 69481 - 69482, 69484 - 69487, 69489 - 69492, 69494 - 69497, 69499 - 69502, 69504 - 69507, 69509 - 69512, 69514 - 69517, 69519 - 69520, 69522 - 69525, 69527 - 69530, 69532 - 69535, 69537 - 69540, 69542 - 69545, 69547 - 69550, 69564 - 69567, 69569, 69571 - 69572, 69574 - 69577, 69579 - 69580

A.3 Period Summaries for the Analysis

The used period summaries are listed in table A.2. The period summaries from KNM3 were used to study the electric potential variance per pixel and for the sensitivity studies. New period summaries were simulated for KNM4+5, which account for issues with the alignment. They were used for all analysis of the measurements conducted in KNM4 and KNM5.

Table A.2: Period Summary Files used in the analysis.

KNMx	Magnetic field setting	File name
KNM3	1.0 G	GlobalKNM3Simulation-PeriodSummary_Jul2020b_32000V_1.0G-000001.ktf
KNM3	2.7 G	GlobalKNM3Simulation-PeriodSummary_Jul2020b_32000V_2.7G-000002.ktf
KNM4+5	1.0 G	GlobalKNM3Simulation-PeriodSummary_Jul2021b-KryptonSimpleLFCS-UpdatedAndCorrected-CorrectedAP-ShiftedFPD_32000V_1.0G.ktf
KNM4+5	2.7 G	GlobalKNM3Simulation-PeriodSummary_Jul2021b-KryptonSimpleLFCS-UpdatedAndCorrected-CorrectedAP-ShiftedFPD_32000V_2.7G.ktf

Appendix B

Additional Figures

B.1 Additional Figures of the Sensitivity Studies

In this section, additional figures from the sensitivity studies in section 5.2 can be found.

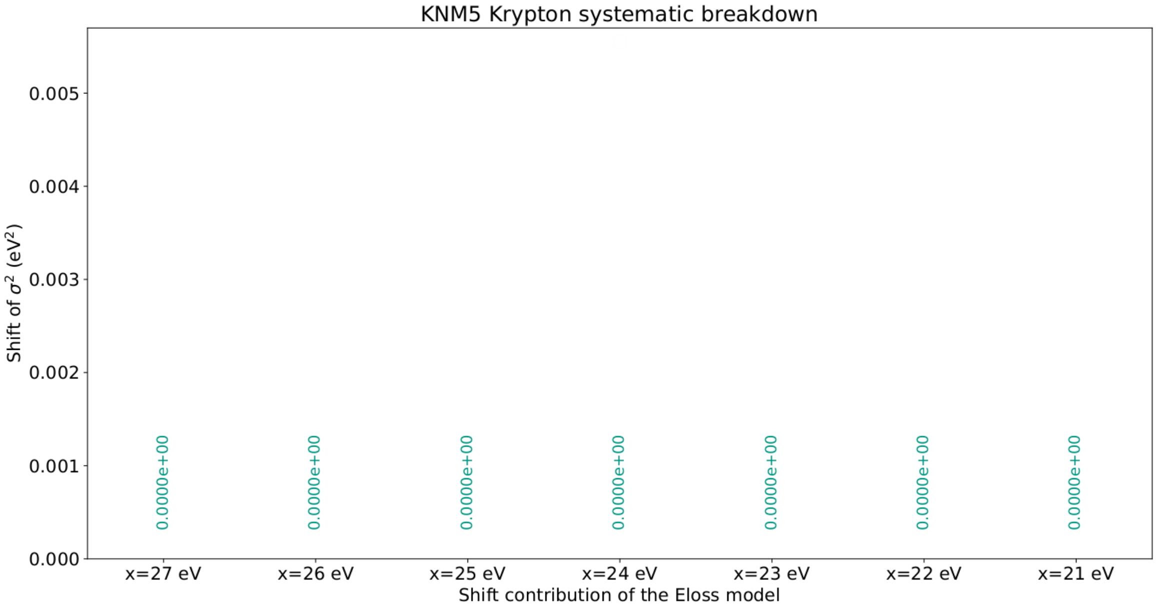

Figure B.1: Shift of $\boldsymbol{\sigma^2}$ with the KNM1 Eloss model dependent on the analysing interval for 1 d and 14 d measurement time. The shift is in comparison to the mean value of $4 \times 10^{-3}\,\mathrm{eV}^2$. The lower energy limit of the total analysing interval x is varied. The depiction is based on the routine introduced in subsection 5.2.2. The shifts on σ^2 are negligibly small and are independent on the analysing interval.

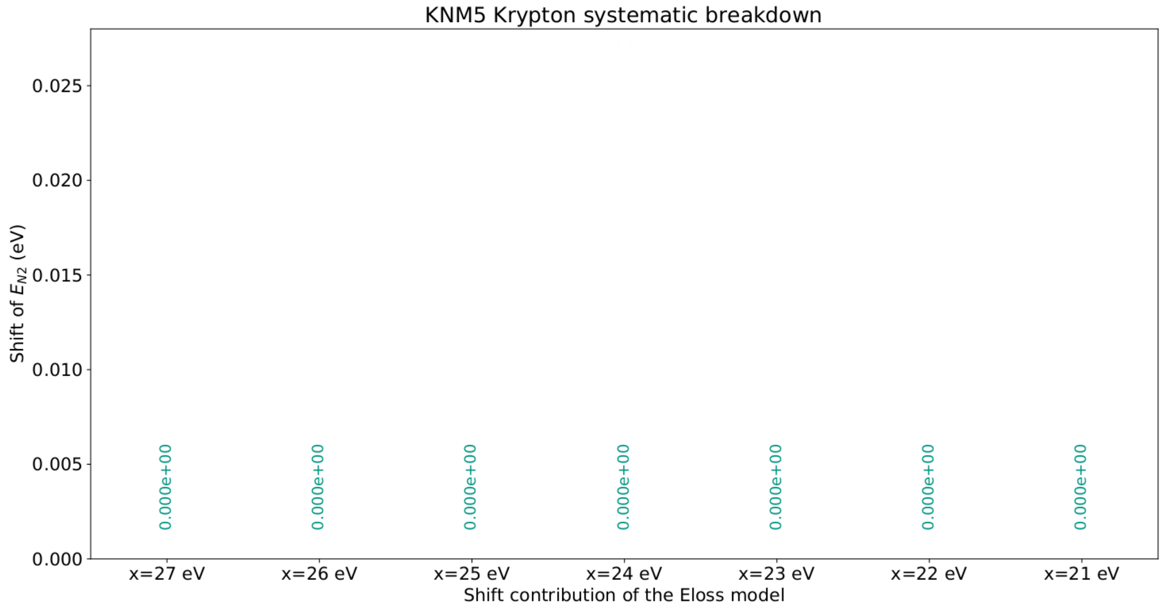

Figure B.2: Shift of E_{N2} with the KNM1 Eloss model dependent on the analysing interval for 1 d and 14 d measurement time. The shift is in comparison to the mean value of 32 136.72 eV. The lower energy limit of the total analysing interval x is varied. The depiction is based on the routine introduced in subsection 5.2.2. The shifts on E_{N2} are negligibly small and are independent on the analysing interval.

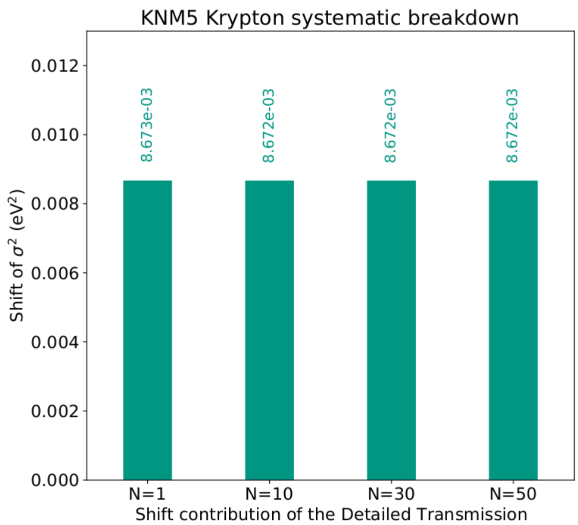

Figure B.3: Shift of σ^2 with the Detailed Transmission model dependent on the number of slices of the source N for 1 d and 14 d measurement time. The shift is in comparison to the mean value of 4×10^{-3} eV^2. Here, the detailed transmission for unscattered electrons (i=0) has been used. The depiction is based on the routine introduced in subsection 5.2.2. The shifts on σ^2 are independent on the number of slices N.

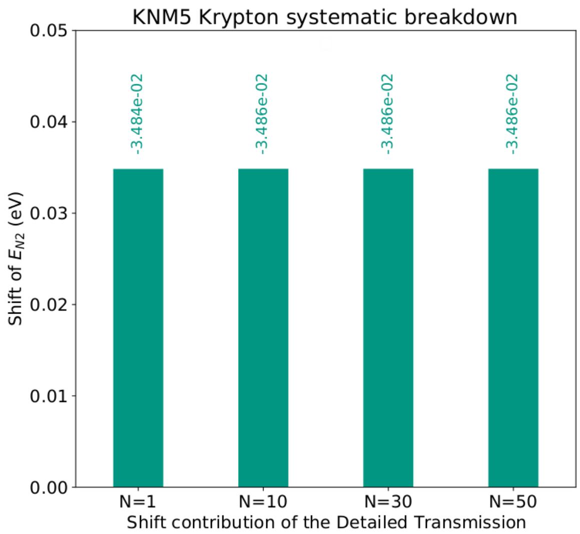

Figure B.4: Shift of E_{N2} with the Detailed Transmission model dependent on the number of slices of the source N for 1 d and 14 d measurement time. The shift is in comparison to the mean value of 32 136.72 eV. Here, the detailed transmission for unscattered electrons (i=0) has been used. The depiction is based on the routine introduced in subsection 5.2.2. The shifts on E_{N2} are independent on the number of slices N.

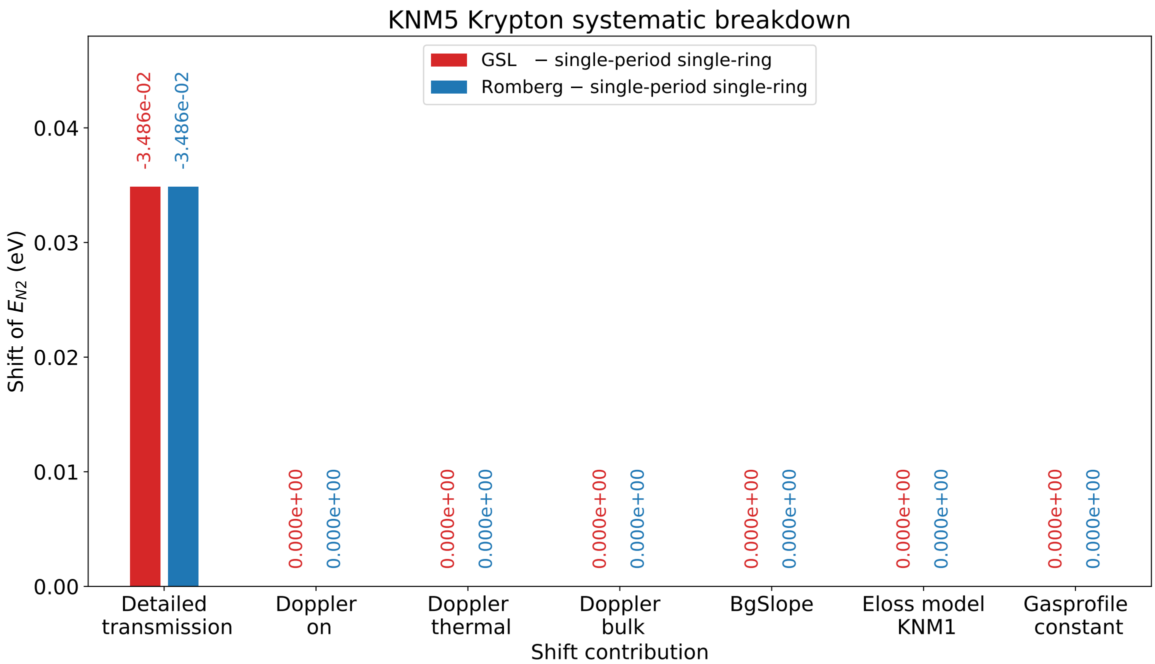

Figure B.5: Shift of E_{N2} dependent on various model settings for two different integration methods, the GSL and the Romberg integrator. The shift is in comparison to the mean value of 32 136.72 eV. The depiction is based on the routine introduced in subsection 5.2.2. The shifts on E_{N2} are independent on the used integration method.

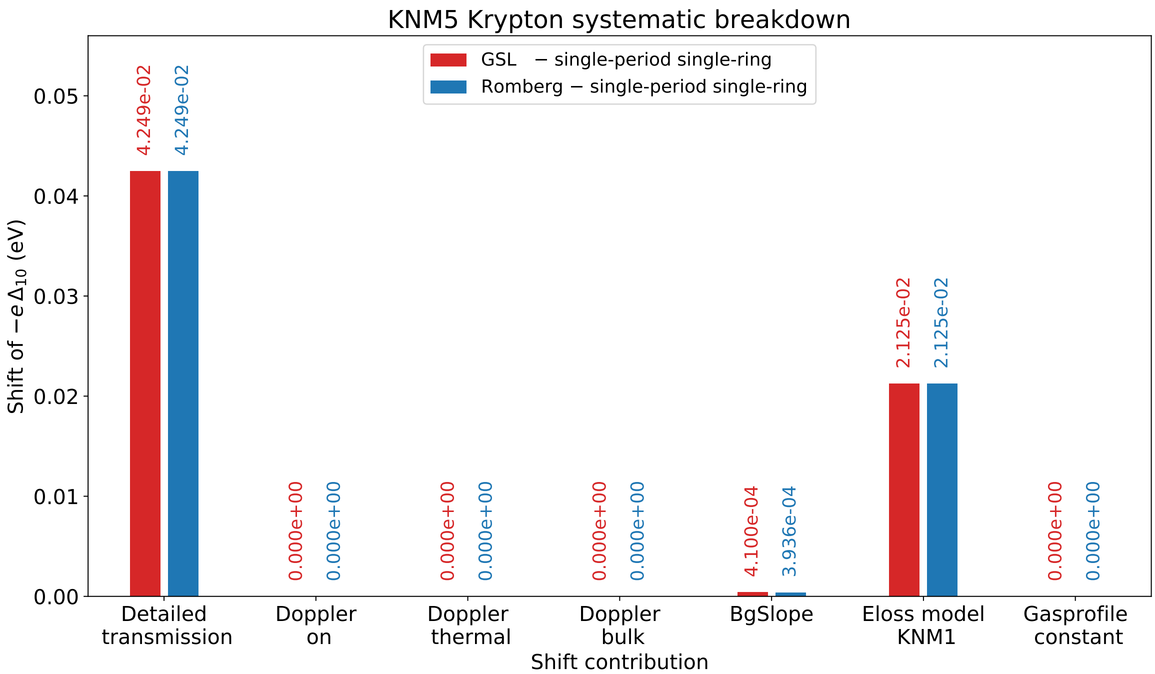

Figure B.6: Shift of Δ_{10} dependent on various model settings for two different integration methods, the GSL and the Romberg integrator. The shift is in comparison to the mean value of 0 eV. The depiction is based on the routine introduced in subsection 5.2.2. The shifts on Δ_{10} are independent on the used integration method.

List of Figures

List of Tables

Bibliography

[AAA+02] Q. R. Ahmad, R. C. Allen, T. C. Andersen, J. D. Anglin, and J. C. Barton *et al.* Direct Evidence for Neutrino Flavor Transformation from Neutral-Current Interactions in the Sudbury Neutrino Observatory. *Physical Review Letters*, 89, 2002.

[AAA+18] DS Akerib, S Alsum, HM Araújo, X Bai, and Aj Bailey *et al.* Position Reconstruction in LUX. *Journal of Instrumentation*, 2018.

[AAA+19] M. Aker, K. Altenmüller, M. Arenz, M. Babutzka, and J. Barrett *et al.* Improved Upper Limit on the Neutrino Mass from a Direct Kinematic Method by KATRIN. *Physical Review Letters*, 123, 2019.

[AAA+20] D. Q. Adams, C. Alduino, K. Alfonso, F. T. Avignone, and O. Azzolini *et al.* Improved Limit on Neutrinoless Double-Beta Decay in 130-Te with CUORE. *Physical Review Letters*, 124, 2020.

[AAA+21] M. Aker, K. Altenmüller, J. F. Amsbaugh, M. Arenz, and M. Babutzka *et al.* The Design, Construction, and Commissioning of the KATRIN Experiment. *prepared for submission to JINST*, 2021.

[AAB+04] J Angrik, T Armbrust, A Beglarian, U Besserer, and J Blümer *et al.* KATRIN design report 2004. *Wissenschaftliche Berichte FZKA*, 2004.

[AAK+85] G Bradley Armen, Teijo Aberg, Kh Rezaul Karim, Jon C Levin, and Bernd Crasemann *et al.* Threshold Double Photoexcitation of Argon with Synchrotron Radiation. *Physical Review Letters*, 54, 1985.

[ABB+18] M. Agostini, A. M. Bakalyarov, M. Balata, I. Barabanov, and L. Baudis *et al.* Improved Limit on Neutrinoless Double-Beta Decay of 76-Ge from GERDA Phase II. *Physical Review Letters*, 120, 2018.

[ABB+19] G. Anton, I. Badhrees, P. S. Barbeau, D. Beck, and V. Belov *et al.* Search for Neutrinoless Double-Beta Decay with the Complete EXO-200 Dataset. *Physical Review Letters*, 123, 2019.

[ABB+21] M. Aker, A. Beglarian, J. Behrens, A. Berlev, and U. Besserer *et al.* Precision measurement of the electron energy-loss function in tritium and deuterium gas for the KATRIN experiment. *The European Physical Journal C*, 81, 2021.

[AFG+94] J. N. Abdurashitov, E. L. Faizov, V. N. Gavrin, A. O. Gusev, and A. V. Kalikhov *et al.* Results from SAGE (The Russian-American gallium solar neutrino experiment). *Physics Letters B*, 328, 1994.

[Bab14] Martin Babutzka. *Design and development for the Rearsection of the KATRIN experiment.* PhD thesis, Karlsruher Institute of Technology, 2014.

[Bar04] Roger Barlow. Asymmetric Statistical Errors. *arXiv preprint*, 2004.

[Beh16] Jan David Behrens. *Design and commissioning of a mono-energetic photoelectron source and active background reduction by magnetic pulse at the KATRIN experiment.* PhD thesis, University of Münster, 2016.

[BF28] M Born and V Fock. Beweis des Adiabatensatzes. *Zeitschrift für Physik*, 51, 1928.

[BGZ+11] A. I. Belesev, E. V. Geraskin, B. L. Zhuikov, S. V. Zadorozhny, and O. V. Kazachenko *et al.* Investigation of space-charge effects in gaseous tritium as a source of distortions of the beta spectrum observed in the Troitsk neutrino-mass experiment. *Physics of Atomic Nuclei*, 71, 2011.

[Bil10] Samoil Bilenky. *Introduction to the Physics of Massive and Mixed Neutrinos*, volume 817 of *Lecture Notes in Physics*. Springer, Berlin, Heidelberg, 2010.

[Blo22] Fabian Block. *Magnetic Field Systematics and Statistical Data Analysis Tools for Neutrino Mass Analysis with KATRIN.* PhD thesis, Karlsruhe Institute of Technology, 2022.

[Böt20] Matthias Böttcher. *Analysis of Krypton Conversion Electron Lines of the Gaseous Krypton-Tritium Source of KATRIN.* PhD thesis, University of Münster, 2020.

[CDR+98] Bruce T. Cleveland, Timothy Daily, Jr. Raymond Davis, James R. Distel, and Kenneth Lande *et al.* Measurement of the Solar Electron Neutrino Flux with the Homestake Chlorine Detector. *The Astrophysical Journal*, 496, 1998.

[Cha14] J Chadwick. Intensitätsverteilung im magnetischen Spectrum der \beta-Strahlen von radium B + C. *Verhandl. Dtsc. Phys. Ges.*, 16, 1914.

[Cho19] Wonqook Choi. Nu scan analysis report. Internal KATRIN document, 2019.

[col04] KATRIN collaboration. WGTS charging. Internal KATRIN document, 2004.

[CP01] J. L. Campbell and Tibor Papp. Widths of the atomic K–N7 levels. *Atomic Data and Nuclear Data Tables*, 77, 2001.

[CRH+56] C. L. Cowan, F. Reines, F. B. Harrison, H. W. Kruse, and A. D. McGuire. “detection of the free neutrino: a confirmation. *Science*, 178, 1956.

[DDL+90] D. Decamp, B. Deschizeaux, J. P. Lees, M. N. Minard, and J. M. Crespo *et al.* A precise determination of the number of families with light neutrinos and of the Z boson partial widths. *Physics Letters B*, 235, 1990.

[Def17] Marco Deffert. *Simulation of the global beam line alignment of the KATRIN experiment.* Master thesis, Karlsruhe Institute of Technology, 2017.

[DGG+62] G. Danby, J-M. Gaillard, K. Goulianos, L. M. Lederman, and N. Mistry *et al.* Observation of High-Energy Neutrino Reactions and the Existence of Two Kinds of Neutrinos. *Physical Review Letters*, 9, 1962.

[DKMS05] A. Dinklage, T. Klinger, G. Marx, and L. Schweikhard. *Plasma Physics: Confinement, Transport and Collective Effects*, volume 790. Springer, Berlin Heidelberg, 2005.

[DKS64] I. Dostrovsky, S. Katcoff, and A. W. Stoenner. Decay Scheme of 83-Rb. *Physical Review*, 136, 1964.

[EEF+01] V Eckardt, T Eggert, H Fessler, H Hümmler, and G Lo Curto *et al.* Calibration of the STAR Forward Time Projection Chamber with Krypton-83m. Technical report, Max-Planck-Institut für Physik, München, 2001.

[Erh16] Moritz Gérard Erhard. *Influence of the magnetic field on the transmission characteristics and the neutrino mass systematic of the KATRIN experiment*. PhD thesis, Karlsruhe Institute of Technology, 2016.

[FFI+01] S. Fukuda, Y. Fukuda, M. Ishitsuka, Y. Itow, and T. Kajita *et al.* Constraints on Neutrino Oscillations Using 1258 Days of Super-Kamiokande Solar Neutrino Data. *Physical Review Letters*, 86, 2001.

[FML+21] Caroline Fengler, Moritz Machatschek, Alexey Lokhov, Vikas Gupta, and Matthias Böttcher *et al.* The Krypton V campaign - measurement proposal. Internal KATRIN document, 2021.

[Frä17] F.M. Fränkle. Background processes in the KATRIN main spectrometer. *Journal of Physics: Conference Series*, 2017.

[Fri20] Fabian Ruben Friedel. *Ion and plasma systematics during the first KATRIN neutrino mass measurements*. PhD thesis, Karlsruhe Institute of Technology, 2020.

[Gal12] Peter T. Gallagher. Introduction to Plasma Physics, 2012.

[GBD+14] L. Gastaldo, K. Blaum, A. Doerr, Ch. E. Düllmann, and K. Eberhardt *et al.* The Electron Capture Ho-163 Experiment ECHo. *Journal of Low Temperature Physics*, 176(5):876–884, may 2014.

[GGH+16] A. Gando, Y. Gando, T. Hachiya, A. Hayashi, and S. Hayashida *et al.* Search for Majorana Neutrinos Near the Inverted Mass Hierarchy Region with KamLAND-Zen. *Physical Review Letters*, 117, 2016.

[GP69] V. Gribov and B. Pontecorvo. Neutrino astronomy and lepton charge. *Physics Letters B*, 28, 1969.

[Gro15] Stefan Groh. *Modeling of the response function and measurement of transmission properties of the KATRIN experiment*. PhD thesis, Karlsruhe Institute of Technology, 2015.

[GSL] GSL Team. Numerical Integration — GSL 2.7 documentation.

[Gup21] Vikas Gupta. L-32 measurements in KryptonV. Internal KATRIN document, 2021.

[Hac17] Moritz Thomas Hackenjos. *KATRIN "First Light" - Commissioning and Modelling of the Beamline*. PhD thesis, Karlsruhe Institute of Technology, 2017.

[HHH+99] W. Hampel, J. Handt, G. Heusser, J. Kiko, and T. Kirsten *et al.* GALLEX solar neutrino observations: Results for GALLEX IV. *Phys.Lett.B*, 447, 1999.

[Hin18] Dominic Fabian Hinz. *Ionisation Mechanisms of Pb-206 Induced Rydberg Atoms*. Master thesis, Karlsruhe Institute of Technology, 2018.

[HLL+20] V Hannen, B Lehnert, A Lokhov, C Rodenbeck, and R Sack *et al.* T2 energy loss parameterization update including KNM2 data. Internal KAT-

RIN document, 2020.

[Höt12] Markus Hötzel. *Simulation and analysis of source-related effects for KATRIN.* PhD thesis, Karlsruhe Institute of Technology, 2012.

[Hua10] Jiayu Hua. *Simulation des Kryptonmodus der Tritiumquelle WGTS im KATRIN Experiment.* PhD thesis, Karlsruhe Institute of Technology, 2010.

[Käf12] Wolfgang Käfer. *Sensitivity Studies for the KATRIN experiment.* PhD thesis, Karlsruhe Institute of Technology, 2012.

[KBD+19] M Kleesiek, J Behrens, G Drexlin, K Eitel, and M Erhard *et al.* β-Decay Spectrum, Response Function and Statistical Model for Neutrino Mass Measurements with the KATRIN Experiment. *The European Physical Journal C*, 79, 2019.

[KBT+08] T. Kibédi, T. W. Burrows, M. B. Trzhaskovskaya, P. M. Davidson, and C. W. Nestor. Evaluation of theoretical conversion coefficients using BrIcc. *Nuclear Instruments and Methods in Physics Research, Section A: Accelerators, Spectrometers, Detectors and Associated Equipment*, 589, 2008.

[Kle14] Marco Kleesiek. *A Data-Analysis and Sensitivity-Optimization Framework for the KATRIN Experiment.* PhD thesis, Karlsruhe Institute of Technology, 2014.

[Kle18] Manuel Klein. *Tritium ions in KATRIN: blocking, removal and detection.* PhD thesis, Karlsruhe Institute of Technology, 2018.

[Kle21a] Manuel Klein. Discrepancy in optimal RW voltages. Internal KATRIN document, 2021.

[Kle21b] Manuel Klein. Optimal rear wall bias. Internal KATRIN document, 2021.

[Kle21c] Manuel Klein. Plasma drifts : two observables. Internal KATRIN document, 2021.

[KS10] Denize Kalempa and Felix Sharipov. Separation phenomenon in the Windowless Gaseous Tritium Source of KATRIN experiment. Ternary mixtures. Technical report, Karlsruhe Institute of Technology, 2010.

[KUA+01] K. Kodama, N. Ushida, C. Andreopoulos, N. Saoulidou, and G. Tzanakos *et al.* Observation of tau neutrino interactions. *Physics Letters B*, 504, 2001.

[Kuc16] Laura Kuckert. *The windowless gaseous tritium source of the KATRIN experiment – Characterisation of gas dynamical and plasma properties.* PhD thesis, Karlsruhe Institute of Technology, 2016.

[Lei14] Benjamin Leiber. *Investigations of background due to secondary electron emission in the KATRIN-experiment.* PhD thesis, Karlsruher Institute of Technology, 2014.

[Lis17] Luca Lista. *Statistical Methods for Data Analysis in Particle Physics*, volume 941 of *Lecture Notes in Physics*. Springer International Publishing, Cham, 2017.

[Liu73] J. W. Liu. Total Inelastic Cross Section for Collisions of H2 with Fast Charged Particles. *Physical Review A*, 7, 1973.

[Mac16] Moritz Machatschek. *Simulation of the m Kr Mode of the Tritium Source of the KATRIN Experiment.* Master thesis, Karlsruhe Institute of Technology, 2016.

[Mac21a] Moritz Machatschek. *A Phenomenological Theory of KATRIN Source Potential Systematics and its Application in Krypton-83m Calibration Measurements.* PhD thesis, Karlsruhe Institute of Technology, 2021.

[Mac21b] Moritz Machatschek. Krypton Negative Width Fluctuations. Internal KATRIN document, 2021.

[MB78] J. H. Misguich and R. Balescu. 'Clumps' as enhanced correlations and turbulent Debye screening. *Plasma Physics*, 20, 1978.

[MF09] Benjamin Monreal and Joseph A. Formaggio. Relativistic Cyclotron Radiation Detection of Tritium Decay Electrons as a New Technique for Measuring the Neutrino Mass. *Phys.Rev.D*, 80, 2009.

[OL77] J. J. Olivero and R. L. Longbothum. Empirical fits to the Voigt line width: A brief review. *Journal of Quantitative Spectroscopy and Radiative Transfer*, 17, 1977.

[Ost08] Beatrix Ostrick. *Eine kondensierte Kr-83m-Kalibrationsquelle für das KATRIN-Experiment.* PhD thesis, University of Münster, 2008.

[Ost20] Raphael Ostertag. *Investigation of Plasma Effects in the KATRIN Source with Kr-83m.* Masters thesis, Karlsruhe Institute of Technology, 2020.

[Per09] Donald H. Perkins. *Particle astrophysics.* Oxford University Press, 2009.

[Pla83] R. L. Plackett. Karl Pearson and the Chi-Squared Test. *International Statistical Review / Revue Internationale de Statistique*, 51, 1983.

[Pra11] M. Prall. The Katrin experiment and the pre-spectrometer at reduced retarding potential. *Progress in Particle and Nuclear Physics*, 66, 2011.

[Pri13] Florian Priester. *Tritiumtechnologie für die fensterlose Quelle WGTS von KATRIN.* PhD thesis, Karlsruhe Institute of Technology, 2013.

[RFAP78] F. Rösel, H. M. Fries, K. Alder, and H. C. Pauli. Internal conversion coefficients for all atomic shells. *Atomic Data and Nuclear Data Tables*, 21, 1978.

[Röt19] Carsten Röttele. *Tritium suppression factor of the KATRIN transport section.* PhD thesis, Karlsruhe Institute of Technology, 2019.

[Sac20] Rudolf Sack. *Measurement of the energy loss of 18.6 keV electrons on deuterium gas and determination of the tritium Q-value at the KATRIN experiment.* PhD thesis, University of Münster, 2020.

[SBB+20] A.G. Singh, E.P. Bernard, A. Biekert, E.M. Boulton, and S.B. Cahn *et al.* Analysis of 83m Kr prompt scintillation signals in the PIXeY detector. *Journal of Instrumentation*, 2020.

[Sch14] Matthew D. Schwartz. *Quantum Field Theory and the Standard Model.* Cambridge University Press, 2014.

[Sch21] Lutz Schimpf. *Characterisation of energy loss processes of 18 . 6 keV electrons inside the windowless tritium source of KATRIN.* PhD thesis, Karlsruhe Institute of Technology, 2021.

[SJZ08] Zhang Shiwei, Han Jin, and Zhang Zhijun. Computer Simulation of Positional Beaming Effect of Molecular Flow in Straight Cylindrical Pipeline by Monte Carlo Method. *International Conference on Computer Science* *and Information Technology*, 2008.

[SK20] F Spanier and J Kellerer. Limits on the electrostatic potential in the WGTS. Technical report, Karlsruhe Institute of Technology, 2020.

[SM19] H Seitz-Moskaliuk. *Characterisation of the KATRIN tritiumsource and evaluation of systematic effects*. PhD thesis, Karlsruhe Institute of Technology, 2019.

[Suz95] Yoichiro Suzuki. Kamiokande solar neutrino results. *Nuclear Physics B - Proceedings Supplements*, 38, 1995.

[Tro18] Nikolaus Rainer-Maria Trost. *Modeling and measurement of Rydberg-State mediated Background at the KATRIN Main Spectrometer*. PhD thesis, Karlsruhe Institute of Technology, 2018.

[Val09] Kathrin Valerius. *Spectrometer-related background processes and their suppression in the KATRIN experiment*. PhD thesis, Muenster University, 2009.

[vM85] K. v. Meyenn, editor. *Wolfgang Pauli - Wissenschaftlicher Briefwechsel mit Bohr, Einstein, Heisenberg u.a.*, volume 2 of *Sources in the History of Mathematics and Physical Sciences*. Springer Berlin Heidelberg, Berlin, Heidelberg, 1985.

[VSD+18] D. Vénos, J. Sentkerestiová, O. Dragoun, M. Slezák, M. Ryšavý, and A. Špalek. Properties of 83mKr conversion electrons and their use in the KATRIN experiment. *Journal of Instrumentation*, 13(2), 2018.

[WBB+91] D L Wark, R Bartlett, T J Bowles, R G H Robertson, and D S Sivia *et al.* Correspondence of Electron Spectra from Photoionization and Nuclear Internal Conversion. *Physical Review Letter*, 67:17, 1991.

[WW97] V. Weisskopf and E. Wigner. Berechnung der natürlichen Linienbreite auf Grund der Dirac schen Lichttheorie. In *The Collected Works of Eugene Paul Wigner*. Springer, 1997.

[Zac15] M Zacher. *High-field electrodes design and and an angular-selective photoelectron source for the KATRIN spectrometers.* PhD thesis, University of Münster, 2015.

[ZBB+20] P A Zyla, R M Barnett, J Beringer, O Dahl, and D A Dwyer *et al.* Review of Particle Physics. *Progress of Theoretical and Experimental Physics*, 2020, 2020.

[Zub20] Kai Zuber. *Neutrino Physics.* CRC Press, Third edition. | Boca Raton : CRC Press, 2020. | Series: Series in high energy physics, cosmology & gravitation, 2020.